2016

Multiphysics Modelling of Sodium Sulfur Battery

Jerry Hunter Mason

Multiphysics Modelling of Sodium Sulfur Battery

Jerry Hunter Mason

Dissertation submitted to the

Benjamin M Statler College of Engineering and Mineral Resources

at **West Virginia University**

in partial fulfillment of the requirements for the degree of

Doctor of Philosophy

in

Mechanical Engineering

Ismail Celik, Ph.D., Chair

Xingbo Liu, Ph.D.

Harry Finklea, Ph.D.

Nianqiang Wu, Ph.D.

Vyacheslav Akkerman, Ph.D.

Department of Mechanical and Aerospace Engineering

West Virginia University

Morgantown, West Virginia

2015

Keywords: Sodium Polysulfide Battery, Electrochemistry, Porous Media Flow, Capillary Flow

Abstract

Multiphysics Modelling of Sodium Sulfur Battery

Jerry Mason

Due to global climate change and the desire to decrease greenhouse gas emissions, large scale energy storage has become a critical issue. Renewable energy sources such as wind and solar will not be a viable energy source unless the storage problem is solved. One of the practical and cost effective solutions for this problem is sodium sulfur batteries. These batteries are comprised of liquid electrode materials suspended in porous media and operate at relatively high temperatures (>300˚C). The sodium anode and the sulfur/sodium-polysulfide cathode are separated by a solid electrolyte made of beta-alumina or NASICON material. Due to the use of porous materials in the electrodes, capillary pressure and the combination of capillary action and gravity become important.

Capillary pressure has a strong dependence on the wetting phase (liquid electrode material) saturation; therefore sharp concentration gradients can occur between the inert gas and the electrode liquid, especially within the cathode. These concentration gradients can have direct impacts on the electrodynamics of the battery as they may produce areas of high electrical potential variation, which can decrease efficiency and even cause failures. Then, thermal management also becomes vital since the electrochemistry and material properties are sensitive to temperature gradients.

To investigate these phenomena in detail and to attempt to improve upon battery design a multi-dimensional, multi-phase code has been developed and validated in this study. Then a porous media flow model is implemented. Transport equations for charge, mass and heat are solved in a time marching fashion using finite volume method. Material properties are calculated and updated as a function of time. The porous media model is coupled with the continuity equation and a separate diffusion equation for the liquid sodium in the melt. The total mass transport model is coupled with charge transport via Faraday's law.

Results show that overpotential is significantly higher in the porous region of the cathode as was predicted by models in the literature. Overpotential is also high on the electrolyte surface and wall. Alternative electrode configurations with high resistive layers recommended by previous researchers also produce areas of high potential gradient. New electrode designs including conductivity gradients and porous media property variations are simulated and compared to previous designs and then recommendations are made for optimum cell operating conditions.

Acknowledgements

First and foremost, I want to express my utmost gratitude to my family for always supporting me and pushing me to succeed. I required a great deal of encouragement and help in my personal life to make my work possible. I want to especially thank my wife, Carla, who has been with me since I was an undergraduate and never once doubted me, even when I doubted myself. I must also thank my daughter Madolyn who brightens my life and provided me with the inspiration to complete my research.

I must also acknowledge my advisor and committee chair, Dr. Ismail Celik, whom has been behind me since I was an undergraduate student at WVU as well. He has had a lot of patience with me as I have grown as a person and as a researcher, always pushing me to be better in both respects. Additionally, his in depth knowledge, wisdom and leadership have provided me with a solid foundation on which to perform my work.

I would also like to thank all other members of my graduate committee: Dr. Harry Finklea for teaching me about electrochemistry and helping me with my electrochemical modelling, Dr. Xingbo Liu for working with me and providing funding through his research group – the Center for Electrochemical Energy Storage (CEES), Dr. Nianqiang Wu for providing me with an opportunity to experimentally validate my porous media model with his group and Dr. Vyacheslav Akkerman for the courses which he taught and the advice he has given me. Each of my committee members have provided me with valuable knowledge

and feedback on my work which have been instrumental to the completion of my dissertation as well as my overall education. I would also like to thank Xuefei Gao for her experimental work in Dr. Wu's lab which helped with my porous media model.

Finally, I would like to recognize my fellow students and post docs within the Computational Fluid Dynamics and Applied Multi-Physics (CFD&AMP) Center. They have been great friends as well as great coworkers. I would to give special thanks to Hayri, Vijay, Fan, Engin, Berk, Mehmet, Albio, Raju, Steve, Tao, Satish, Jose and Sergio. They all made my time in the office enjoyable while also helping with any problem that I may have had in any way they could. Thank you for everything.

Table of Contents

List of Figures

List of Tables

Nomenclature

Symbol	Description	Units
a	Chemical activity	
a_S	Surface area density	(m^2/m^3)
b'	Empirical parameter $b' = bnF/RT$ where $b = 384.9642\ mV$	
C_α	Normalized molar concentration of species α	
C_T	Dimensionless parameter	
c_α	Molar concentration of species α	(mol/m^3)
c_p	Constant pressure thermal capacitance	$(J/kg-K)$
c'	Empirical parameter $c' = cnF/RT$ where $c = 74.8151\ mV$	
D	Diffusion coefficient	(m^2/s)
DoD	Depth of discharge	
d'	Empirical parameter $d' = dnF/RT$ where $d = 5.0553\ mV$	
E	Either Formal potential or Nernst potential	(V)
e	Charge of a single electron	$(1.60217662 \times 10^{-19}\ coul)$
F	Faraday's Constant	$(Coul/mol)$
$\vec{F}$	Force vector	(N)
G	Gibb's free energy	(J/mol)
H	Enthalpy	(J)
h	Convection heat transfer coefficient	(W/m^2-K)
g	Gravity or applied pressure gradient	(m/s^2)
I	Applied current density	(A/m^2)

Symbol	Description	Units
i_F	Faradaic current density	(A/m^2)
i_0	Exchange current density	(A/m^2)
J	Current density	(A/m^2)
j	Non-dimensional current density	
K_P	Polarization resistance	$(\Omega \mathrm{m}^2)$
$K_{P,T}$	Temperature dependent polarization resistance	$(\Omega \mathrm{m}^2/K)$
$\vec{k}_0$	Permeability tensor	(m^2)
$k_{r\alpha}$	Reduced permeability of phase α	
L	Length	(m)
$\dot{m}$	Mass flow rate	(kg/s)
n	Number of electrons involved in reaction	
P	Total pressure	(Pa)
p_c	Capillary pressure	(Pa)
p_α	Pressure in phase α relative to capillary pressure	(Pa)
$\dot{q}$	Heat generation density	(W/m^3)
R	Ideal gas constant	$(J/mol-K)$
r_c	Mean pore diameter	(m)
S_α	Saturation of species α	
T	Temperature	(K)
t	Time	(s)
t_+	Transference number of Na^+	

Symbol	Description	Units
u_α	Pore velocity of species α	(m/s)
$\forall$	Volume	(m^3)
v	Velocity	(m/s)
W	Weight fraction	
X	From Na_2S_X	
z_α	Charge of species α	
	Greek	
α	Charge transfer coefficient	
β	Expansion coefficient (volume change fraction)	
γ	Surface tension	(N/m)
ε_α	Volume fraction of phase α	
θ	Dimensionless electrical resistance	
λ	Thermal conductivity	
η	Overpotential	(V)
μ	Viscosity	$(N-s/m^2)$
ξ	Resistance	(Ω)
ρ	Material density	(kg/m^3)
σ	Electrical or ionic conductivity	$(1/\Omega - m)$
τ	Tortuosity	
ϕ	Potential	(V)
ψ	Wetting angle	(Radians)

Subscripts/Superscripts

Symbol	Description
$+$	Of or related to the positive ion (cation, Na^+) or charge of +1
$-$	Of or related to the negative ion (anion, $S_X^=$) or charge of -1
$=$	Charge of -2
0	Normalized or reference value
α	General phase designation
a	Anode
B	Refers to the finite volume below current finite volume ($z_B = z_P - \Delta z$)
b	Bottom face of finite volume ($z_b = z_P - \Delta z/2$). Also may refer to buoyancy
c	Cathode or Capillary
E	Refers to the finite volume to the east of the current finite volume ($x_E = x_P + \Delta x$)
e	Related to electronic current. Also refers to east face of finite volume ($x_e = x_P + \Delta x/2$)
eff	Effective value of a property based on concentrations, porosity, etc.
F	Faradaic (as in Faradaic current i_F)
g	Related to gravity
gas	Gas phase
i	Related to ionic current
liq	Liquid phase
N	Refers to the finite volume to the east of the current finite volume ($y_N = y_P + \Delta y$)

Symbol	Description
n	Non-wetting phase. Also refers to north face of finite volume ($y_n = y_P + \Delta y/2$)
OCV	Of or related to the open circuit voltage
$ohmic$	Related to IR drop and resulting heat generation
OX	Oxidized species
P	Refers to coordinates of the volumetric center of a finite volume (x_P, y_P, z_P)
por	Related to open pore space
$react$	Related to chemical reaction
RED	Reduced species
r	Reduced value or residual
ref	Reference value
S	Total sulfur. Also refers to the finite volume to the east of the current finite volume ($y_N = y_P - \Delta y$)
s	Refers to south boundary of finite volume ($y_s = y_P + \Delta y/2$)
sol	Solid phase
T	Refers to the volume above current finite volume $z_T = z_P + \Delta z$
t	Top face of finite volume ($z_t = z_P + \Delta z/2$)
$total$	Total combination of parameter
W	Refers to the finite volume to the west of the current finite volume ($x_W = x_P - \Delta x$)
w	Wetting phase. Also refers to west face of finite volume ($x_w = x_P - \Delta x/2$)

Chapter 1: Introduction

Sodium sulfur (NaS) batteries are electrochemical energy storage devices which have been recognized as good candidates for large-scale grid energy storage. The system consists of liquid electrode materials including a sodium anode and sulfur/sodium polysulfide cathode separated by a dense ceramic electrolyte which is a good sodium ion conductor [1]. Na-S batteries have a high energy density and thermodynamic efficiency for charge and discharge cycles. It usually operates between 300 to 350 ^{o}C and is constructed from cost effective materials [1]. These batteries are unique in that the viscous electrode materials are suspended within porous media and are sensitive to temperature. Therefore, the phenomena of capillary flow and heating due to the electrochemistry become important in cell design and application.

1.1 Motivation

With the concerns of global climate change due to greenhouse gas emissions, it has become more important than ever to efficiently store and distribute renewable forms of energy. However, the mainstream forms of renewable energy, including wind and solar, are not able to adjust to the cyclic daily power demands associated with the energy grid. For example, during cold weather more electricity is used at night when solar energy is not being harnessed. Wind energy is somewhat unpredictable depending on the location and is also inconsistent even over short time frames. Because of this, the power grid must always be supplemented by other energy sources, most generally fossil fuels or nuclear power plants, during peak demand times. On the other hand, large scale energy

storage can be used to harness excess energy during periods of low demand from the renewable energy sources as an alternative and cleaner solution.

Currently there are a few practical ways to store excess power: pumped hydroelectric, compressed air and electrochemical energy storage. The first and most cost effective storage technique involves constructing pumped hydroelectric systems which store energy by pumping water uphill from a lower reservoir to an upper reservoir. Water from this upper reservoir is then released into a hydroelectric plant during peak loading times to compliment the other available energy sources. Round trip efficiency of the water is relatively good, on the order of 70-75% [2]. Worldwide, nearly 140 gigawatts of pumped hydroelectric energy is available with typical installed capacities in the range of 200-3000 MW [2]. The average cost of storing this energy globally ranges from $100-200/kWh, with some plants costing much more than others [3]. There are a few drawbacks to building such a system, however. While operation and maintenance costs are low, a large amount of capital is required for initial construction. Also, the reservoirs require large amounts of water and land, with specific topographies not being adequate for effective system operation [2].

Compressed air energy storage (CAES) uses a similar concept to hydroelectric, with air being pumped and compressed into underground caverns or aboveground storage tanks. This air is heated and expanded in a turbine to provide energy during peak loading times. Certain geology must be available for underground storage with price and capacity depending on what is available. Above ground storage, although not fully commercialized, has an estimated average cost of around $434/kWh, which is much higher than hydroelectric, and

round trip efficiency on the order of 42-55% [4]. Typical capacities of above ground tanks average 50 MW [5].

Where pumped hydroelectric power and CAES are impractical or undesirable, electrochemical energy storage in the form of large scale batteries provide an alternative and arguable better solution. Currently NaS batteries are the best possible candidate for this position, with round trip efficiency of 75% and total costs ranging from $445-555/kWh, meaning the system is more efficient with a similar cost to CAES [4]. Although promising research and demonstrations have been done for large scale lead acid batteries, flow batteries and even lithium batteries, NaS batteries are currently the only commercialized form of large scale electrochemical energy storage. Additionally, predicted costs and efficiencies of these new batteries are not significantly better than those of sodium sulfur batteries. For example, while lithium batteries have efficiencies as high as 94%, their estimated cost of power is $900-1700/kWh [4]. Flow batteries, depending on the chemistry used, have predicted efficiencies between 60-75% and costs ranging from $300-1350/kWh [4]. Also, as previously stated, most of these batteries are not yet ready for full commercialization. Typical battery storage facilities have capacities on the order of 1 MW, with some of the new batteries predicting higher capacities of around 10 MW [4].

Due to the unique construction and operation of NaS batteries, specialized numerical models are desired for design and control applications. The effects of porous media within the electrodes and the complex mass transport and electrochemistry taking place within the cathode are especially important. Recently work has been done to create reduced order models for the

electrochemistry and thermodynamics taking place within the cell [6] [7], which are being developed for use in thermal management and control of battery modules. However, a more detailed model is required in order to fully resolve the physics within the cell and explore design modifications which may improve battery performance and reduce the risk of failure. In particular, a phenomena which has not been studied in detail is that of vertically oriented current density gradients which occur within the cathode. Multiple studies have reported this phenomena experimentally and numerically and the problems which may result [1] [8] [9] [10] [11] [12]. The most likely cause is the complex relationship between the solid porous material, capillary flow, gravity and the resulting gradients in overpotential and electrochemistry reaction rates. High reaction rates in the porous region have been related to precipitation of solid Na_2S_2 and Na_2S during discharge and the formation of highly resistive layers of melt with high sulfur content during charge. Both of these are detrimental to cell performance and can increase degradation rates while decreasing efficiency and cell capacity. Measuring and monitoring such phenomena is impractical or impossible experimentally. Therefore, it is very important to develop a model which can resolve a combination of physics which includes porous media flow model in order to design a cell which avoids the aforementioned problems while also maintaining a high level of performance. There has been no previous study which accounted for capillary pressure within the electrodes and there is currently no reliable way to predict cell failure or capacity loses which result from solid precipitation. The goal of this study is to develop a physics based model which considers the combined effects of gravity, buoyancy, capillary pressure, diffusion,

heat transfer and electromigration within the electrodes and to use this model to predict failure of the battery.

1.2 Objectives

The objective of this study is to develop a detailed multiphysics model for NaS batteries which considers as much of the physics as possible. This is done by numerically solving charge, specie and heat transport equations and studying the relationships between them. The material properties will change with time, temperature, phase and specie concentrations. Each transport equation is coupled to all others either directly through relevant source terms or indirectly though relative property changes. Once the model is validated with experiments, proposed design changes are modeled and conclusions about the overall cell design and optimization are made. The computer code being used is written in house and is built upon a transient fuel cell model originally developed by Dr. Raju Pakalapati and Dr. Ismail Celik [13] [14] [15]. The detailed list of objectives is as follows:

1. Adapt Fuel Cell specie transport model, electrochemistry model and equation solvers to NaS battery chemistry and geometries

2. Develop and implement heat transport model and couple with specie and charge transport

3. Develop porous media flow model which considers gravity and buoyancy, including verification with analytical solutions and validation with simple experiments

4. Implement porous media flow model into multiphysics model, coupling with previously developed specie, charge and heat transport

5. Compare the total battery model against numerical and experimental results found in the literature

6. Perform parametric studies on properties which can be similarly altered in real world circumstances

7. Make design modifications to sulfur electrode in an attempt to improve performance

8. Demonstrate ability to predict battery failure and capacity loss

9. Based on these studies, make suggestions about the design and optimization of the batteries and recommend future experimental work

1.3 Organization of Thesis

Including the introduction, this thesis is divided into 8 chapters. In Chapter 2 a literature review is conducted on the basic background of NaS batteries and a detailed account of relevant model developments. Chapter 3 describes in detail the electrochemistry of NaS batteries and goes through the derivation of the charge transport model. Chapter 4 includes discussion and derivation of the specie transport model, which is divided into two parts: 1. Specie transport within the ionic liquids due to ion migration and diffusion 2. Capillary flow due to

saturation gradients between ionic liquid and inert gas. The thermal model is derived in Chapter 5 and the various sources of heat are explored. Details about property models and numerical implementation are given in Chapter 6. Chapter 7 is designated for results and discussion, including analyses of alternative electrode designs. Conclusions and recommendations for future work related to battery performance and optimization are discussed in Chapter 8. Suggestions are made for possible improvements to the battery design and for electrochemical experiments that may provide useful data necessary to improve modelling and design further.

Chapter 2: Literature Review

2.1 Introduction

Initial invention of NaS batteries has been credited to Ford Motor Company during the 1960s [16]. A joint development program undertaken in the mid-1980s by NGK Insulators, LTD. (NGK) and Tokyo Electric Power Co. (TEPCO) heralded the first commercial production beginning in 2003 [17]. NaS Batteries are characterized by high energy density, high DC conversion rate, temperature stability, long operation lives and inexpensive materials [18] [19]. Their energy density is roughly triple that of lead-acid batteries [20] and their DC conversion efficiency is as high as 85% [19]. Because of these characteristics, NaS batteries are excellent tools when used for peak shaving and grid storage applications [21], finding their niche in the renewable energy field. Sunlight and wind energy cannot possibly meet instant demand changes of power customers, but through the use of large scale storage technology, such as NaS batteries, the downfalls of these energy sources can be overcome. The NaS cell consists of negative and positive electrodes comprised of liquid sodium and sulfur respectively [1]. Figure 1 shows a diagram which illustrates the operation of a standard NaS battery.

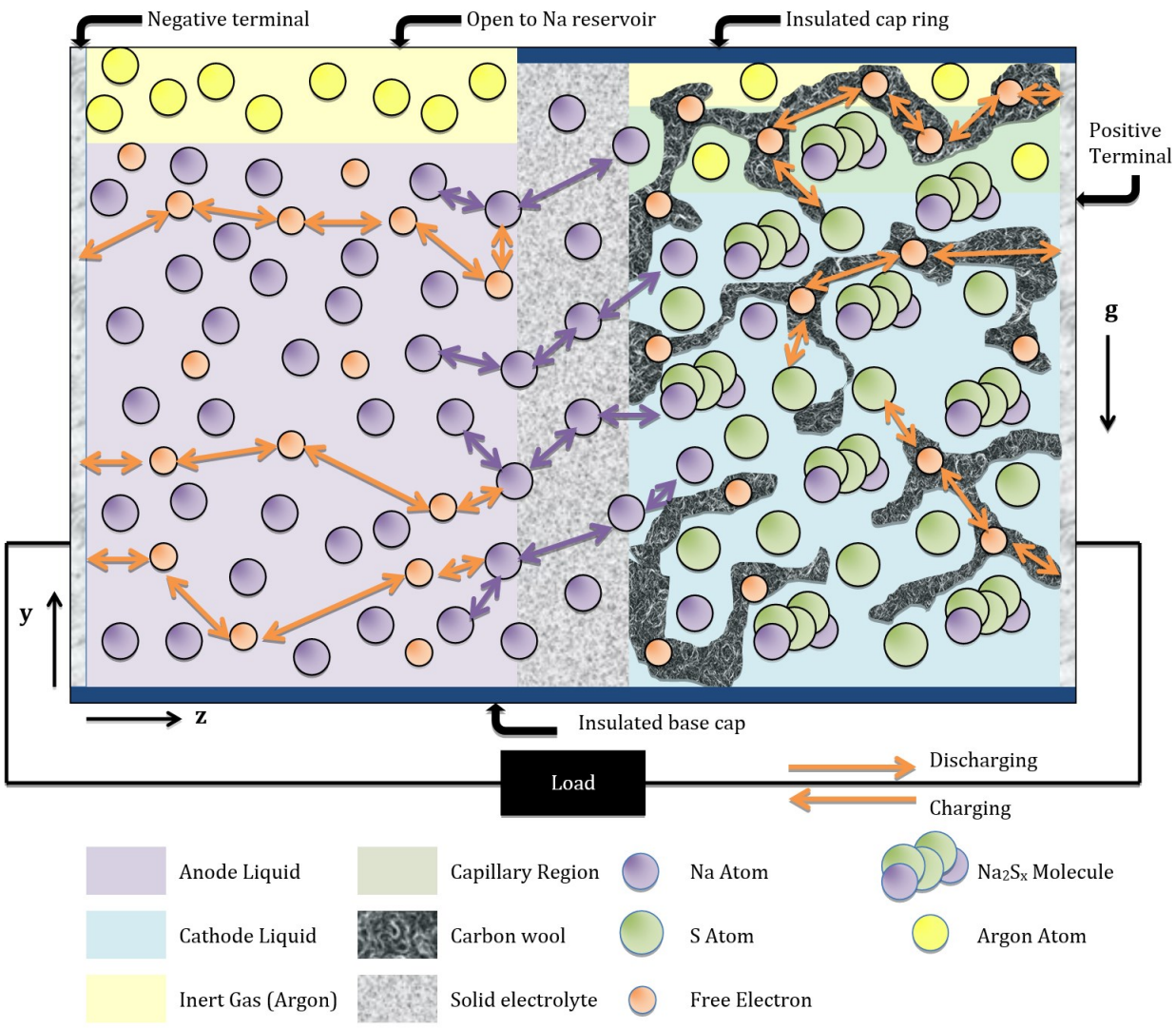

Figure 1 - NaS Cell Illustration, vertical arrangement (note gravity)

The solid electrolyte dividing these electrodes is typically comprised of beta-alumina ceramic [1] [17] [22] with more recently developed batteries having Sodium Super Ion Conductors (NASICON) as electrolytes [23]. The half-cell and overall cell reactions are presented in Equation (1) [24]. Reactions occur from left to right during discharge and right to left during charge.

Anode: $$2Na \rightleftharpoons 2Na^{+} + 2e^{-} \quad (1.a)$$

Cathode: $$XS + 2e^{-} \rightleftharpoons S_X^{=} \quad (1.b)$$

Overall: $$2Na^+ + xS + 2e^- \rightleftharpoons Na_2S_X \quad (1.c)$$

Conventional NaS batteries typically operate between 300 and 350°C in order to avoid solid precipitation in the Sodium Polysulfide (Na_2S_X) melt. This is due to the nature of the phase diagram shown in Figure 2. Operating within this temperature range also decreases the ionic resistance of the electrolyte allowing for adequate flow of Na ions [17].

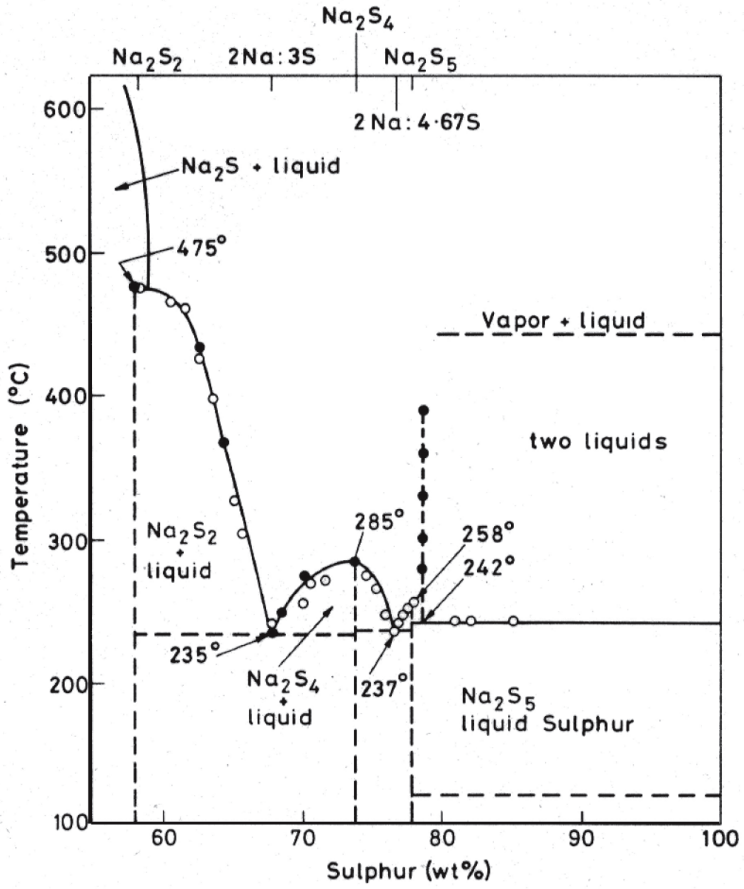

Figure 2 – Na_2S_x Phase Diagram [25]

NaS batteries are a promising technology. However, research and development of new and more efficient NaS cells has been relatively slow

compared to other battery technologies, i.e. lithium ion batteries, which were originally invented about a decade later [26]. The recent developments of NASICON electrolyte materials [27], specifically by researchers at West Virginia University [28] have increased the necessity for an expedited design process. This is where a multiphysics model becomes important. Such a model would be used to study the mass, charge and heat transport phenomena as well as the electrochemistry of a given battery in great detail. Electrode materials and cell dimensions could be optimized within a numerical model before undertaking the expenditure of laboratory testing. Data from small scale experiments of new electrolyte and electrode materials for the purpose of property measurement could be applied to practical batteries within the model in order to study scaling effects and determine the best way to move forward in the design process.

2.2 Previously Developed Models

In order to design sustainable large scale energy storage systems, it is very important to analyze the thermal and electrochemical behavior of a single Na-S battery system. Experimental studies are available for the thermal management and electrochemical performance of the cell [29]. However, there are few computational models that combine both electrochemical performance and the temperature variation in Na-S battery system [29] [30]. All of these models assume ideal conditions within the sodium anode, such that a current flux can be applied on the anode side of the electrolyte as a boundary condition.

2.2.1 Charge Transport Modelling

The charge transport and potential distribution have been modelled both statically and as a function of time by multiple researchers [8] [9] [29] [31] [32].

Early models developed by Gibson and by Breiter and Dunn [31] used analytical methods to study the electrochemical kinetics of the sulfur electrode. These researchers were interested in estimating the potential distribution within the sulfur electrode for the purpose of optimizing the performance of the cell. The electrochemical kinetics show high potential gradients occurring at the cathode-electrolyte interface. Gradients of kinetic factors, particularly that of the overpotential, may cause localized areas of high reaction rates which in turn result in precipitation of insoluble compounds (Na_2S_2 and Na_2S). These solid precipitants can result in electrode inhibition and rapid cell degradation. Gibson's model assumes the cell is radially symmetric (uniform concentration) and approximated as steady state such that the problem becomes one dimensional and independent of time. Additionally, kinetic studies of polysulfide melts allow for the approximation of a linear relationship between the reaction rate and the overpotential. Gibson starts with ohm's law written for the electronic and ionic currents respectively:

$$-\frac{1}{\xi_e}\frac{d^2\phi_e}{dx^2} = \frac{\delta J_e}{\delta x} \tag{2}$$

$$-\frac{1}{\xi_i}\frac{d^2\phi_i}{dx^2} = \frac{\delta J_i}{\delta x} \tag{3}$$

The total applied current is equal to the combination of the ionic and electronic current at any point ($J_e + J_i = I_0, \nabla \cdot J_e = -\nabla \cdot J_i$). Therefore equations (2 and (3 can be combined and integrated with appropriate boundary conditions. The pole is positioned at $x = 0$ with an applied current of $I = 0.1\ A$ while the

electrolyte is placed at $x = L$. The result is an ordinary differential equation which can be solved analytically. The final equation for the overpotential distribution is as follows:

$$\phi_e - \phi_i = \frac{\xi_e I + \xi_i I \cosh\left(\theta^{\frac{1}{2}} L\right)}{\theta^{\frac{1}{2}} \sinh\left(\theta^{\frac{1}{2}} L\right)} \cosh\left(\theta^{\frac{1}{2}}(L - x)\right) - \frac{\xi_i I}{\theta^{\frac{1}{2}}} \sinh\left(\theta^{\frac{1}{2}}(L - x)\right) \tag{4}$$

Where θ is the ratio between the total resistance and the slope resistance: $\theta = \frac{\xi_e + \xi_i}{\delta}$

Parametric studies on electrode thickness L (Figure 3) and the ratio between felt and cathode melt resistance per unit length ξ_i/ξ_e (Figure 4) are performed. A summary of Gibson's results are displayed in Table 1 in the form of surface polarization currents for each case.

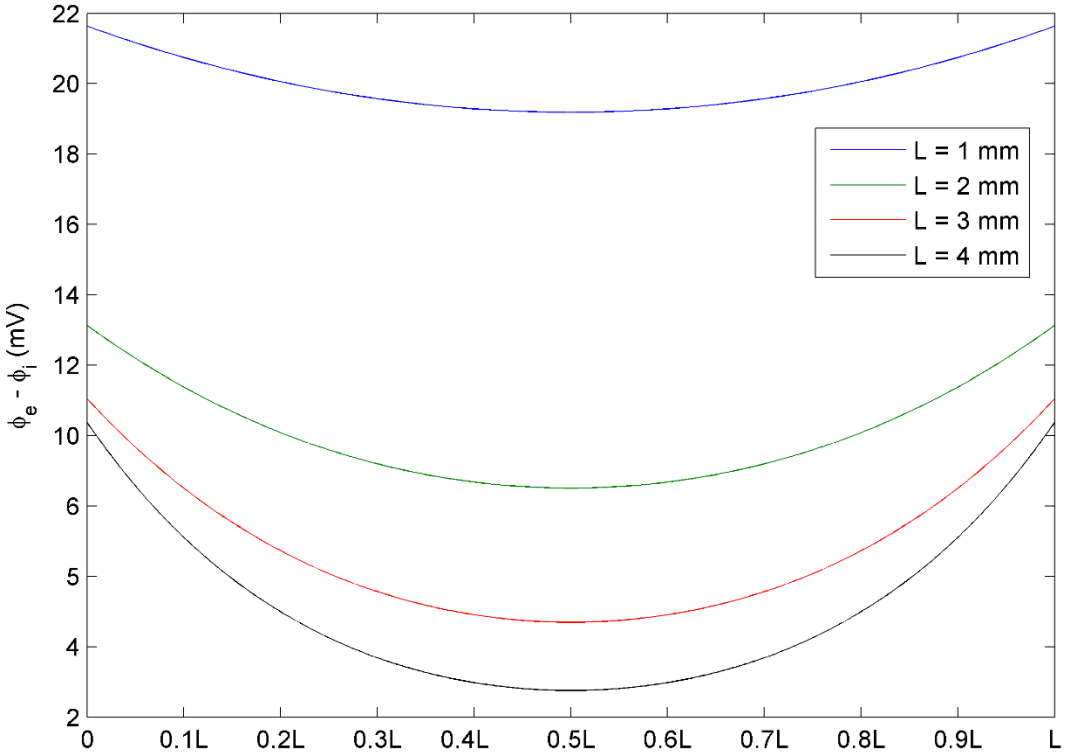

Figure 3 – Parametric study of sulfur electrode thickness originally performed by Gibson [32]

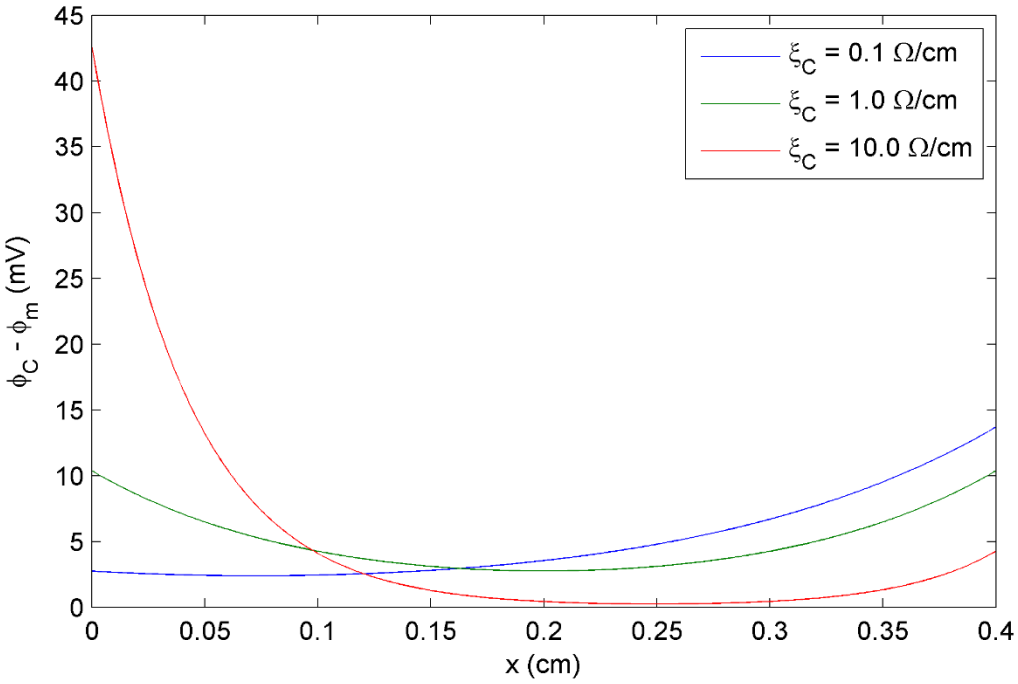

Figure 4 – Parametric study of ratio between melt and porous media resistance originally performed by Gibson [32]

Table 1 – Current consumed at the pole ($\mathbf{I_p}$) as calculated by Gibson [32]

	L			
ξ_i	1 mm	2 mm	3 mm	4 mm
0.1 Ω/cm	35.0	17.0	9.6	6.1
1.0 Ω/cm	38.0	26.0	22.0	21.0
10.0 Ω/cm	57.0	56.0	55.0	55.0

Z = 0.3 Ω, I_0 = 100 mA

Through this study, Gibson finds that the polarization loses are minimized by increasing the electrode thickness while minimizing the resistance of the

porous mat with respect to the melt resistance (increased porosity). However, while a low resistance mat leads to decreased polarization at the electronic pole, high polarization still occurs at the electrolyte surface (Figure 4). This can lead to the development of passive layers during both charge and discharge, limiting cell capacity. In order to alleviate this problem, Breiter and Dunn expand on Gibson's model to consider a highly resistive layer of porous mat at the electrolyte surface dubbing their configuration the 'dual mat' electrode. Using similar assumptions with property values close to real conditions, Breiter and Dunn's model demonstrates that using a dual mat is an effective way to limit the overpotential at the electrolyte surface thus allowing for greater depth of charge/discharge. It is assumed that the potential distribution is continuous at the interface between the dual mat layers in order to close the system. The validity of this assumption is later challenged by Kawamoto and Wada [8]. Using this assumption and applying a similar solution process to the one taken by Gibson, Breiter and Dunn arrive at the following piecewise, analytical solution for the system:

For $x = 0$ to L_1:

$$(\phi_e - \phi_i)_1 = \frac{\xi_i I}{\theta_1^{\frac{1}{2}}} \exp\left(-\theta_1^{\frac{1}{2}} L_1 + \theta_1^{\frac{1}{2}} x\right) + \frac{2 I \xi_{e2}}{\theta_1^{\frac{1}{2}} + \theta_2^{\frac{1}{2}}} \exp\left(-\theta_2^{\frac{1}{2}} L_2 - \theta_1^{\frac{1}{2}} x\right) \tag{5}$$

For $x = L_1$ to L_2: (6)

$$(\phi_e - \phi_i)_2 = \xi_{e2} I \left[\frac{2}{\theta_1^{\frac{1}{2}} + \theta_2^{\frac{1}{2}}} - \frac{1}{\theta_2^{\frac{1}{2}}} \right] \exp\left(-\theta_2^{\frac{1}{2}} L_2 + \theta_2^{\frac{1}{2}} x \right) + \frac{\xi_{e2} I}{\theta_2^{\frac{1}{2}}} \exp\left(-\theta_2^{\frac{1}{2}} x \right)$$

A parametric study is performed on a sulfur electrode of total length $L_0 = 6.6\ mm$ and with a highly resistive layer of thickness $L_2 = 0.8\ mm$ and resistance per unit length of $\xi_{e2} = 2500\ \Omega/cm$. The melt resistance is maintained to be $\xi_i = 4.0\ \Omega/cm$ while the single mat resistance ξ_{e1} is varied from $0.4, 4.0$ and $20.0\ \Omega/cm$. A reproduction of the results of the first case ($\xi_{e1} = 0.4\ \Omega/cm$) is shown in Figure 5. As shown in the figure, the dual mat case exhibits a significant reduction in polarization at the electrolyte surface ($x = 6.6\ mm$) compared to the single mat case, decreasing from 27 mV to 1.1 mV. It is theorized by Breiter and Dunn that this electrode structure allows for enough potential drop from the small electronic current to reduce the potential drop from the higher ionic current in this region.

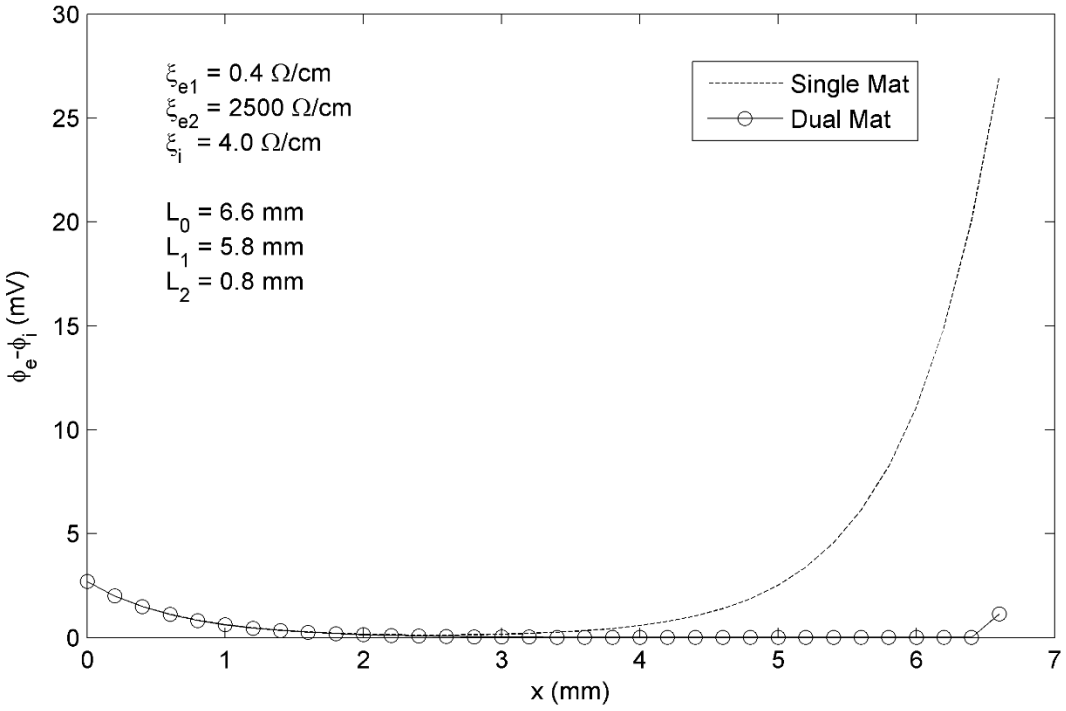

Figure 5 - Comparison of Breiter and Dunn's Dual Mat Electrode to Single Mat Electrode

Kawamoto and Wada are responsible for developing multiple sodium-sulfur battery models both jointly and individually [8] [9] [29] [33] [10]. One of their earlier models [8] focuses primarily on the possible influence of axial concentration gradients due to gravity and porous media effects in the sulfur electrode mat. It has been demonstrated that in a cylindrical, vertically oriented cell that the electrochemical reaction rate not only changes in the radial direction (as studied by Gibson, Breiter and Dunn) but also exhibits a distribution in the axial direction (vertically) [11] [12]. Kawamoto and Wada suggest that the axial distribution of the reaction rate is correlated to a similar distribution in melt concentration, produced by porous media flow phenomena. Both experimental and numerical data are produced for the cell illustrated in Figure 6.

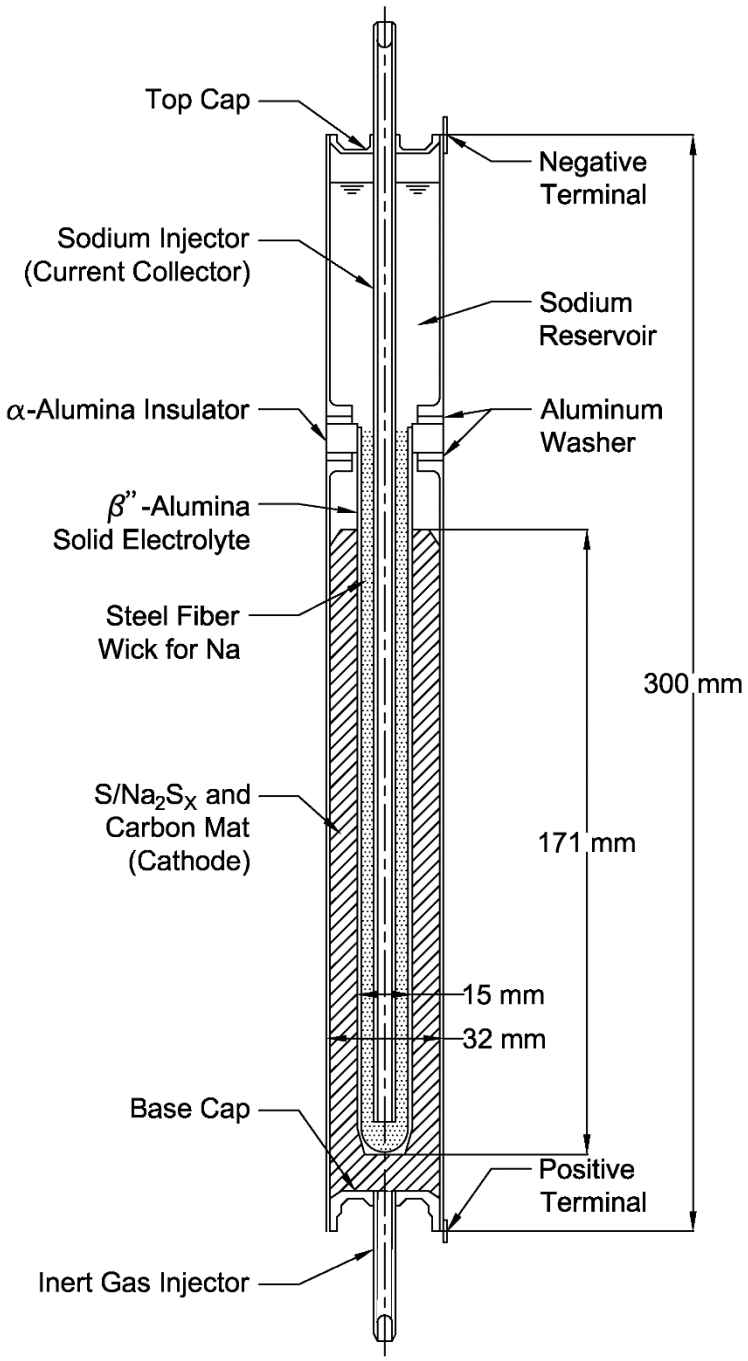

Figure 6 – Schematic of cell studied by Kawamoto, Wada and Kusakabe [29] [8] [9] [33] [10]

Assumptions:

(i) Convection is neglected such that only the ionic potential gradient produces the ionic current

(ii) Exchange current density is linearly proportional to the over potential

(iii) The system is axisymmetric

(iv) Concentrations are assumed uniform in the radial direction but vary linearly in the axial direction (vertically) such that the concentration of the melt is zero at the top of the electrode. As such, certain properties are related to the volume fraction of the melt (see Figure 7).

Assumptions (i) and (ii) are combined with current conservation to produce the following system of equations:

$$\nabla \cdot (-\sigma_i \nabla \phi_i) + \frac{a_s}{K_p} \phi_i = \frac{a_s}{K_p} \phi_e \quad (7)$$

$$\nabla \cdot (-\sigma_e \nabla \phi_e) + \frac{a_s}{K_p} \phi_e = \frac{a_s}{K_p} \phi_i \quad (8)$$

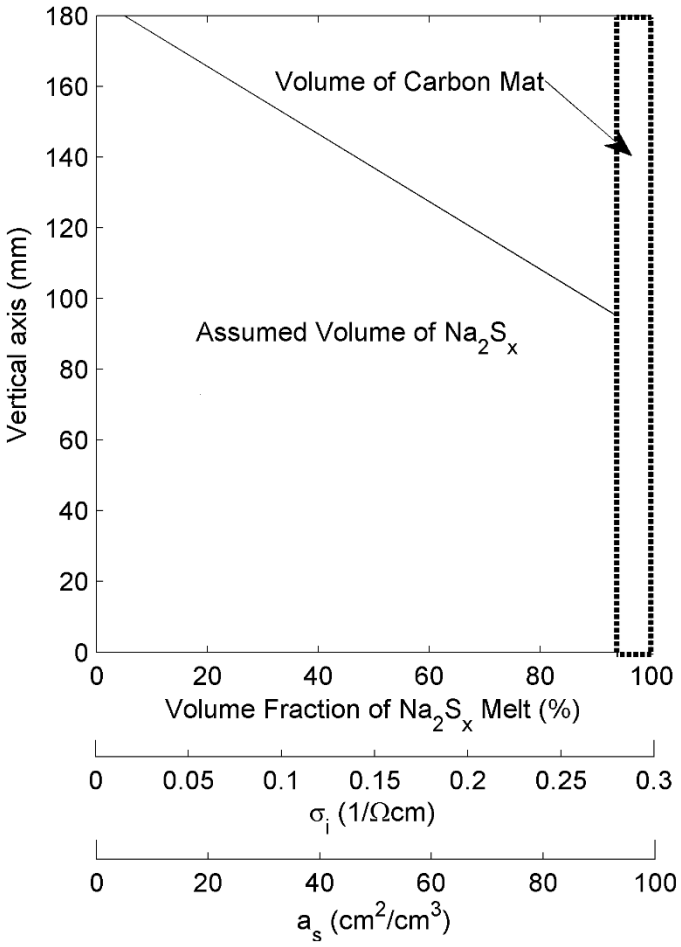

Figure 7 – Applied distribution of melt volume fraction (porosity) and affected properties

This gradient is imposed within the electrochemical model and the distributions of the overpotential and current density are produced for realistic cells at a given static state. The cells studied contain three different cathode mat configurations: (a) Uniform mat conductivity ($0.5\ 1/\Omega\mathrm{cm}$), (b) dual mat with highly resistive layer ($\sigma = 0.0025\ 1/\Omega\mathrm{cm}$) at electrolyte surface and the newly proposed (c) dual-dual mat with an additional medium resistive layer ($\sigma = 0.1\ 1/\Omega\mathrm{cm}$). This third mat is positioned within the region of assumed capillary rise from 145 mm to 18 mm vertically. The electrode has an inside diameter (electrolyte surface) of 7.5 mm

and outside diameter of 15 mm. The effective length of the electrode is 180 mm and a total current of 5 amps is applied. Contours of the overpotential in the cathode for each case as per Kawamoto and Wada's model are illustrated in Figure 8.

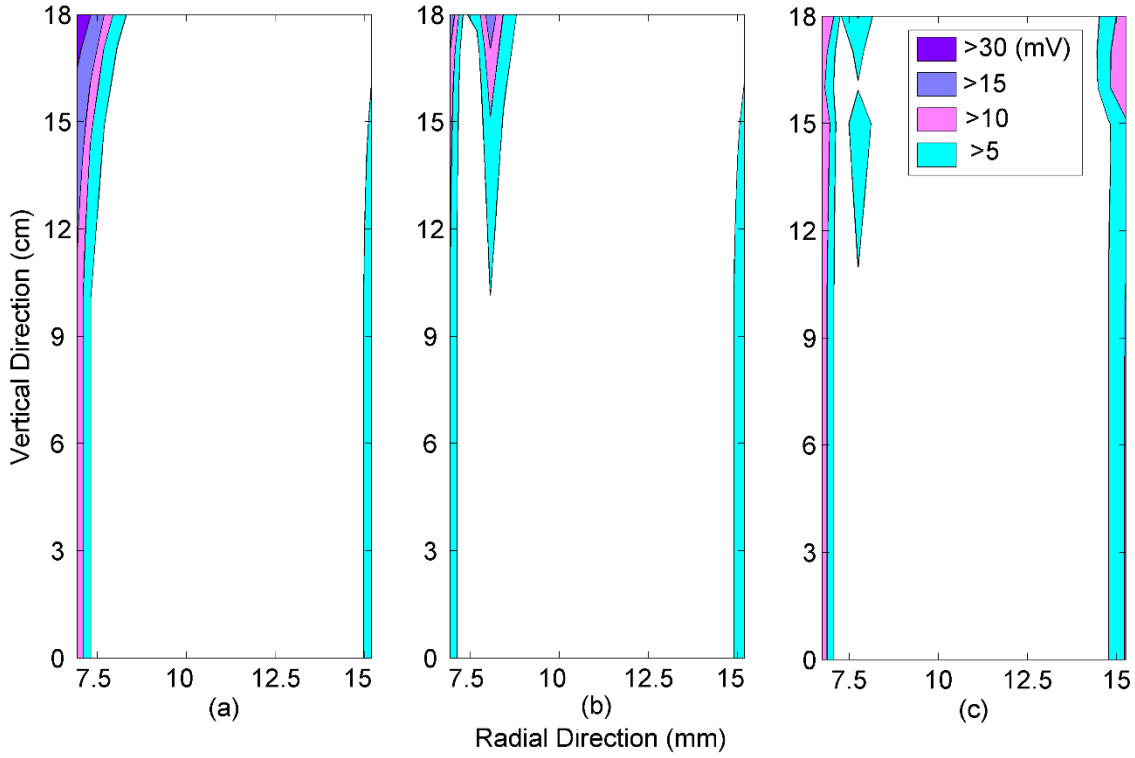

Figure 8 – Distributions of the overpotential for (a) single (b) dual and (c) dual dual mat electrode configurations

Cases (a) and (b) produce results similar to those presented by Breiter and Dunn with high over potential (5-10 mV) occurring in the region closest to the electrolyte. However, because of the concentration gradient assumed to be produced by the capillary rise in the porous media, a small area of even higher over potential (15-30 mV) occurs near the top of the electrode at the electrolyte surface and between the high and low resistive mat layers. These results suggest

that a concentration gradient caused by gravity and porous media effects would produce overpotential high enough to cause rapid production of sodium polysulfide; leading to solid precipitation of Na_2S_2 and Na_2S. This leads the authors to suggest the medium resistance layer described in case (c). Results for this case show that the maximum overpotential has decreased to about 5 mV for the given conditions and distributes the reaction rate much more evenly throughout the electrode. This would theoretically allow for greater sodium penetration, leading to a more uniform concentration gradient. However, because none of the models mentioned thus far consider species transport, no solid conclusions can be made pertaining to reactant concentration gradients and their effects on the system. Additionally, while the importance of porous media effects are clearly demonstrated, no real effort is made to accurately model the transport within porous media which will be induced by density gradients (gravity) and capillary flow (due to capillary pressure). Regardless, some agreement occurs between experimental and numerical data for the single mat electrode as shown in Figure 9.

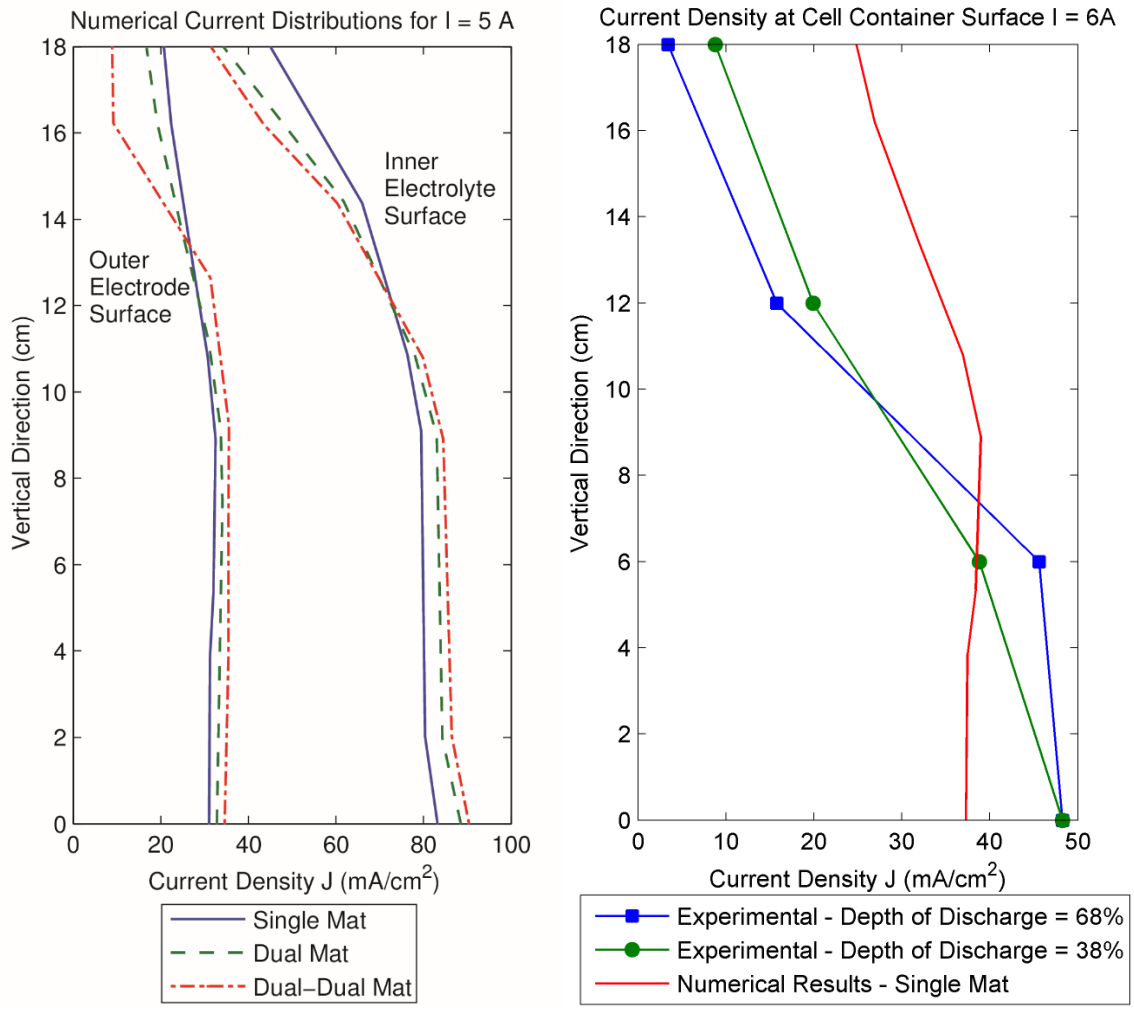

(a) **(b)**

Figure 9 – (a) Calculated current density distributions with applied current $I = 5A$ and (b) Experimentally measured current density distributions in vertical direction with applied current of $I = 6\ A$ [8]

Kawamoto applies this same model to further explore NaS battery performance [9]. Alternative linear distributions of melt in the porous media which depend on the depth of discharge are modeled. The calculated vertical distributions in current density are then compared to empirical data taken at similar depths of discharge. Experiments show that significant charge distributions occur, especially at low depths of discharge (in two phase region). At the end of charge/beginning

of discharge, the majority of the current passes near the bottom of the cell rapidly decreasing with height. Moving towards the two phase region, this gradient decreases substantially until the distribution becomes relatively constant. Calculations are limited to the single phase region, however the model does predict the trend of decreasing current density in the vertical direction. A more sophisticated model which can handle multiple phases and mass transport due to capillary motion as well as diffusion would be needed to study the performance in the two phase region. Currently, such a model has not been produced.

The effects that voids within the carbon mat might have on operation and degradation are also explored. Kawamoto changes the domain from a vertical cross section to a horizontal one, ignoring distributions in the vertical direction in order to explore variations within the radial and tangential directions. Two different cases are studied, one in which a void exists in the carbon mat over a small portion of the electrolyte surface and the second in which a similar void exists between the carbon mat and the metal container. It is found that when the void is in contact with the electrolyte that the current density decreases in this area while increasing elsewhere which can lead to non-uniform electrolyte degradation. Voids at the container surface seem to cause increased current density in the area adjacent to the voids, which can result in rapid corrosion of the metal. Additionally, regardless of where the void is located, the cell resistance is increased. It is also predicted that when a void is located at the electrolyte surface that sulfur within the void will not be utilized due to a lack of current (no current collector present). It is concluded that careful manufacturing processes should be used in order to prevent these phenomena from taking place.

2.2.2 Specie Transport Modelling

Kao and Wayner were among the earliest developers of species transport models for NaS batteries [34]. While Gibson and other model developers focused on electrochemistry and the effect of the relationship between melt and mesh conductivity, it was pointed out that they neglected the more significant influences that concentration gradients have on battery performance. Kao and Wayner's solution was a one dimensional transient model which solved for the polysulfide concentration profiles within the sulfur electrode during discharge.

Assumptions:

(i) The sulfur electrode can be represented as a superposition of two continua (sulfur polysulfide melt and the carbon felt).

(ii) Experiments by Cleaver and Davis [35] show that sulfur atoms are transported with sulfide ions, simplifying the system to consider only one velocity.

(iii) Double layer capacitance was neglected and the electrode kinetics can be modeled using a diffusion model.

(iv) It is assumed that the electrode expands radially during discharge

Empirical formulas were used to calculate the chemical potential of atomic sulfur and melt conductivity. The three equation system solves for the dimensionless current density (J), the reference velocity (v_{ref}) and X from Na_2S_X in a time marching fashion via the orthogonal collocation method.

$$\frac{\partial^2 j}{\partial x^2} = C_t \frac{\partial j}{\partial x} + C_t^2 j + \left[1 - \left(\frac{I}{a' J_i \Delta R}\right)^2 \left(\frac{\partial j}{\partial x} + C_t j\right)^2\right] + \left[\zeta \left\{j - \frac{\sigma_i}{\sigma_i + \sigma_e}\left(\frac{R_o}{R_o - y\Delta R}\right)\right\} - \frac{X a' J_i \Delta R}{I}(b' + 2c'X + 3d'X^2)\frac{\partial X}{\partial x}\right] \quad (9)$$

$$\frac{\partial}{\partial x}\left(\frac{v_{ref}}{C_t}\right) = \frac{\forall_1 I}{2F}\frac{\partial}{\partial x}\left(\frac{jX}{C_t}\right) \quad (10)$$

$$\frac{\partial X}{\partial t} = \frac{(19 + 18.4X)^2 C_t}{18.4\Delta R}\frac{\partial}{\partial x}\left[\frac{v_{ref}}{C_t(19 + 18.4X)}\right] \quad (11)$$

Where $x = \frac{r - R_0}{R_1 - R_0}$, $C_t = \frac{\Delta R}{\gamma \Delta R + R_0}$, $\gamma = a' J_i \Delta R^2 \left(\frac{1}{\theta_1} + \frac{1}{\theta_2}\right)$ and $j = \frac{J_i}{I}$

Transient values of concentration and reaction overpotential are calculated from the results for a cell with outer radius $R_0 = 0.3\ cm$, active electrode thickness $\Delta R = 0.2587\ cm$ and $\alpha = 100\ cm^{-1}$. Given initially uniform concentrations, three cases are studied with applied current densities of $I_{R_0} = 0.12345, 0.3705$ and $0.823\ A/cm^2$ respectively. Each simulation is executed until "*X*" falls below 3.0 at any point in the electrode, which is the point were solid precipitation will likely occur. Results consistently show that the reaction rate (over potential) is initially non uniform, particularly at the electrolyte surface, just as predicted by both Gibson's model and Breiter and Dunn's model. However, the reaction rate tends towards uniformity as the depth of discharge increases. This

means that the high reaction rate obtained with the static electrochemical models is only of concern at the very beginning of the discharge cycle. Ergo, Kao and Wayner's results suggest that this initially amplified rate does not persist long enough to cause issues within the system, assuming that there is charge acceptance to begin with. On the other hand, the opposite phenomenon occurs for the polysulfide concentration. It is initially uniform and becomes less so during discharge. The non-uniformity (gradient) increases as the current increases, resulting in significant capacity loss. In other words, the higher the current, the less energy is produced before the value of "*X*" reaches a point where solid precipitation is imminent. This holds true for each variation of the melt and mesh conductivities. While this model demonstrates the importance of monitoring and understanding species concentrations, it cannot simulate more complex dual mat sulfur electrode because of the over simplification of the charge transport. A model which combines the transient species transport as well as a discretized charge transport equation must be used.

2.2.3 Coupled Charge/Specie Transport Modelling

As a response to this need, Wada presents a transient, one dimensional, radially symmetric model [33]. This model is a combination of Gibson's work on potential distribution calculations with Kao and Wayner's work on specie distribution profiles within NaS batteries. The purpose of the model is to study the species transport within a dual mat sulfur electrode, so that a more concrete conclusion can be made about the effect that the resistive layer has on the gradient of specie concentration.

Assumptions:

(i) Electrode reaction can be simplified to:

$$2Na^{+} + S_x + 2e^{-} \Leftrightarrow Na_sS_x$$

(ii) Sodium ions are transported within the sulfur species and diffusion driven by density gradients are neglected:

$$\vec{J}_i = e(n_+\vec{u}_+ - 2n_-\vec{u}_-) = -\sigma_i\vec{\nabla}\phi_i \qquad (12)$$

(iii) It is assumed that the electrode expands axially (vertically) during discharge rather than radially as assumed by Kao and Wayner

(iv) Exchange current density is assumed to be linearly proportional to the overpotential

The species transport equation for species "α" within the cathode melt is expressed as follows:

$$\frac{\partial n_\alpha}{\partial t} + \vec{\nabla}\cdot(n_\alpha\vec{u}_\alpha) = \dot{\omega}_\alpha \qquad (13)$$

The chemical activity (also called electromotive force) and the melt resistivity are calculated using empirical formulas. Equations (12 and (13 for the charge and species transport, respectively, are simplified using the listed assumptions such that only two equations are need to describe the system. Scaling factors β and L for electrode volume and length respectively are calculated as a functions of the species concentrations (depth of discharge) and cell geometry in order to satisfy the third assumption. Equation (14) is used to solve for the sodium species concentration while Equation (15) solves for the current density in the melt.

$$\frac{\partial}{\partial r}\frac{1}{r}\frac{\partial}{\partial r}rJ_i + \frac{a_s}{K_p}\left\{-\left(\frac{1}{\sigma_i}+\frac{1}{\sigma_e}\right)J_i + \frac{1}{\sigma_e}\frac{r_1}{r}I + \frac{\partial E_{OCV}}{\partial r}\right\} = 0 \qquad (14)$$

$$\frac{\partial c_+}{\partial t} = \frac{\beta}{RF}\frac{1}{r}\frac{\partial}{\partial r}\left\{C_+(rJ_i - r_1 I)\frac{r_o^2 - r^2}{r_o^2 - r_1^2}\right\} - \frac{L}{F}\frac{1}{r}\frac{\partial}{\partial r}(rJ_i) \qquad (15)$$

All other variables which are of interest (such as C_S and overpotentials) can be calculated as analytical functions of these two unknowns (i.e. "*X*" in Na_2S_X and over potential). Values used for the conductivity, porosity, area density and other properties are close to that of a real cell similar to the one shown in Figure 6. A current density of $\pm 100\ mA/cm^2$ is applied in the simulation of both a single and dual mat electrode for the sake of comparison, primarily to investigate the influence that the dual mat has on the sodium polysulfide concentration gradient. In addition, unlike Kao and Wayner, Wada's model is used to simulate the charge cycle of the electrode (corresponding to the negative applied current density) as well as the discharge cycle. Similar to Kao and Wayner, Wada's model predicts that a concentration gradient will occur within the melt and that the initial high gradient in overpotential rapidly decreases during both charge and discharge. The results also show that the dual mat electrode not only reduces the initial spike in overpotential near the electrolyte during discharge, but also mitigates the high concentration gradient which occurs in the same area as the battery moves further into the charge or discharge cycle.

Kawamoto [10] improves upon Wada's [33] model by exploring the overpotential and concentration gradients in the two phase region (when atomic sulfur is present within the cathode) as well as the one phase region explored

previously. Diffusion due to electro-migration is added to the model such that an additional source term is included in the ionic current conservation equation

$$J_i = -\sigma_i \nabla \phi_i - F(z_+ D_+ \nabla c_+ + z_- D_- \nabla c_-) \tag{16}$$

Where:

$$D = \frac{D_+ D_- (z_+ - z_-)}{z_+ D_+ - z_- D_-} \tag{17}$$

$$t_+ = \frac{z_+ D_+}{z_+ D_+ - z_- D_-} \tag{18}$$

Equations (17 and (18 are substituted into (16 and then the ionic and electronic currents are related via charge transport, similar to previous models. The resulting equations describing the charge transport within the NaS battery are Equations (19 and (20.

$$-\nabla \cdot (\sigma_i \nabla \phi_i) + \frac{a_s}{K_p} \phi_i = \frac{1}{3} F \nabla \cdot \left\{ D \frac{3t_+ - 1}{t_+(1 - t_+)} \nabla c_+ \right\} + \frac{a_s}{K_p} (\phi_e - \mu) \tag{19}$$

$$-\nabla \cdot (\sigma_e \nabla \phi_e) + \frac{a_s}{K_p} \phi_e = \frac{a_s}{K_p} (\phi_i - \mu) \tag{20}$$

Because sodium ions have a transference number near unity, Kawamoto concludes that the derivative of the sodium ion concentration with respect to time is proportional to the divergence of the ionic current density (Equation (21)).

$$\frac{\partial c_+}{\partial t} = -\frac{1}{F}\nabla \cdot J_i = \frac{a_s}{K_p}(\phi_e - \phi_i - \mu) \qquad (21)$$

Realistic values are used for coefficients and properties with ionic conductivity σ_i and area density a_s being time dependent functions of x (from Na_2S_x). The equations are rewritten in radial coordinates, assuming axial symmetry, and solved numerically for a range of applied currents (3, 6 and 9 amps). Full charge and discharge cycles are simulated for the cell previously studied by both Kawamoto and Wada [9] [33] (Figure 6) Cell voltage results are plotted against depth of discharge and compared to experimental data. According to their figures, the numerical voltage data closely represents empirical data. A study is performed on the effect that diffusion has on battery performance. When the diffusion coefficient is set to zero during charge, the model predicts blocking to occur close to the transition from single phase melt to a two phase melt (when atomic sulfur is present). Blocking is due to a layer of atomic sulfur developing at the electrolyte surface which causes a region of high resistance. This finding is significant as it shows that diffusion of the sulfur in the melt influences the capacity of the cell greatly. This would explain why capacity decreases as the charging current increases, as illustrated by the experimental data obtained by Kawamoto [10]. Previous models were unable to predict this as they did not explore the phenomena which occur in the two phase region. Kawamoto's model also predicts that the cell resistance and concentration gradient of polysulfide species ("*X*" from Na_2S_X) are strongly influenced by diffusion of sulfur, especially in the two phase region. In the single phase region, each of these parameters follow similar trends to those predicted by previous models [8] [9] [33] [34]. However, once in the two phase region new observations can be made. During charge in

this region, an accumulation of sulfur occurs at the electrolyte surface which in turn increases the cells electrical resistance and would limit the ionic current due to lack of available sodium species. The opposite occurs during discharge as a depletion of sulfur and increase in sodium polysulfide at the electrolyte surface decreases electrical resistance. However, due to the lack in atomic sulfur, sodium entering from the electrolyte will react with sodium polysulfide increasing the probability of formation of insoluble Na_2S_2.

2.2.4 Heat Transport Modelling

Kawamoto along with Kusakabe [29] put forth both experimental and numerical data which outline the thermal behavior of NaS batteries for relatively high current density loads. Application of NaS batteries for load leveling purposes often require the cells to handle high current loads, especially during peak times of the day. Also, it is of interest to understand the performance of batteries in extreme conditions for the accelerated evaluation of cell degradation. Otherwise, cell lifetime tests would take years to complete. When subjected to high current densities (greater than $100\,mA/cm\text{^}2$ of electrolyte surface) a few specific problems occur. Cell performance deteriorates quickly as sulfur utilization and/or sodium penetration is limited, thus decreasing energy efficiency. Unusual temperature rise occurs due to the increased rate of heat generation. At high temperatures the solid electrolyte and metal container may degrade at an accelerated pace. Additionally, the cell can fail or even burst open due to thermal stress and or fatigue. In order to thoroughly study cell performance under extreme conditions, experimental and numerical analysis is performed on cells experiencing current loads ranging from 130 – 390 mA/cm^2. The same battery used by Kawamoto and Wada previously is once again the focus of this study

(Figure 6). During testing, the battery is contained within a heated chamber which maintains a constant ambient temperature of 335^{o}C. Thermocouples are spaced axially on the surface of the battery in order to monitor the temperature of the battery.

Kawamoto employs a numerical model with the following assumptions:

(i) Convection of the reactants is neglected, i.e. species concentrations are homogeneous.

(ii) The system is axisymmetric allowing for one-dimensional cylindrical coordinates

The transient heat transfer equation based on these assumptions is presented as Equation (22) :

$$r\rho c_p \frac{\partial T}{\partial t} - \frac{\partial}{\partial r}\left(r\lambda \frac{\partial T}{\partial r}\right) = r\dot{q} \tag{22}$$

Neumann boundary conditions are applied, assuming free convection on the outside wall of the cell container and considering the radiation within the heater (Equation (23)).

$$\begin{gathered} \frac{\partial T}{\partial r} = 0 \quad \text{at} \quad r = 0 \\ \frac{\partial T}{\partial r} = \frac{h}{\lambda}(T_{amb} - T) + \frac{\epsilon\delta}{\lambda}(T_{amb}^4 - T^4) \ \text{ at } \ r = r_o \end{gathered} \tag{23}$$

While the source term $\dot{q}$ considers Ohmic heating, entropy change and Peltier heat (Equation (24)):

$$\dot{q} = \frac{1}{\sigma}\left(\frac{I}{2\pi r l}\right)^2 \pm \frac{J}{dr} T \frac{dV}{dT} \pm \frac{J}{dr} pT \qquad (24)$$

The conductivity is calculated by integrating a one dimensional resistance network model. Entropy change, which is exothermic during discharge and endothermic during charge, is assigned as a function of the depth of discharge based on the experimental work by Knodler [36]. Peltier heating is assumed to occur at the interface between the sodium electrode and electrolyte surface in addition to being distributed in the sodium polysulfide electrode as being linearly proportional to the electrochemical reaction rate.

The simplified electrochemical model agrees reasonable with experimental measurements of cell voltage outside of the regions where concentration polarization takes place (end of charge, beginning of discharge) for multiple current densities (130-390 mA/cm^2). Meanwhile, the thermal model shows good agreement with wall temperatures taken experimentally for the same applied current densities. With an ambient temperature of 335°C, maximum wall temperatures reach 340-370°C for this current range. The temperature reaches its maximum near the end of charge and its minimum during discharge (near ambient temperature for all cases). Maximum predicted temperatures in the inner wall of the cathode were predicted by the model to reach 350-400°C, meaning that a significant temperature gradient on the order to 10-30°C develops within the battery at high current densities. After 1500 cycles experimentally, thermal fatigue at these operating temperatures are shown to be negligible for the ceramic electrolyte, but substantial for the sealant materials used to construct

the battery. It is concluded that this model can be used to determine if given operating conditions are suitable for safe battery function.

A 2012 paper by Li et al [37] presents results from a multiphysics NaS model which combined the aspects of Kawamoto's 1D thermal model [29] 2D specie model [9] and 1D ionic diffusion model [10] and expanded them all into 2D. The results and discussion suggests that the model considers the transport of sodium polysulfide due to gravity, but according to initial conditions, the same linear distributions as used in [9] are applied again. The authors obtain similar results and reach similar conclusions to those Kawamoto previously. The contribution of this work was the study of radially oriented carbon fibers versus axially oriented ones in the cathode. The idea is that the electric conductivity in the direction of the fibers is less than in the perpendicular direction. Results show that radially oriented fibers promote radial transport of ions in addition to decreasing cell resistance. This means that the sodium ions are spread more evenly throughout the melt and problems such as blocking due to accumulation of sulfur and solid precipitation due to accumulation of sodium are less likely.

2.3 Summary

As inclusive as these models are as a whole, the full effects of porous media and capillary flow, which were shown to be significant by certain models, are usually ignored in the literature. Additionally, the models and experiments are performed in a controlled thermal environment, with the assumption being that the cell temperature is constant or distributed only radially. In real applications, however, NaS cells must operate in a less controlled environment and will be subject to variable rates of discharging and charging. Gradients of temperature,

species concentrations and overpotential in the axial direction are substantial and need to be understood. Additionally, defects and inhomogeneity, especially in the cathode mesh, should be considered. Due to the nature of the materials used and general electrochemistry, understanding the thermodynamics and transient operational performance of NaS cells are of the utmost importance for cell optimization, failure analysis and for prescribing safe operating conditions.

In conclusion, numerous electrochemical models for NaS batteries have been developed beginning as early as 1974 [9] [29] [31] [32] [33] [37]. These previously developed models, though accurate for a given design and parameters, make assumptions which ignore many of the physics which take place within the batteries. The models are either one or two dimensional, idealize the entire anode and ignore thermal effects on the electrochemistry. None model gravity or capillary motion within the electrodes in a realistic way, even though it is demonstrated that this phenomena is important.

Chapter 3: Electrochemistry and Charge Transport Modelling

3.1 Introduction

The foundation of any electrochemical model are the equations for charge transport, exchange current density and the open circuit voltage (Nernst potential). Fundamentally, the equations are derived from the conservation of charge, Ohm's law, the Butler-Volmer equation, Faraday's law and Gibb's free energy. Gibbs free energy in the form of the Nernst Equation is replaced by an empirical relationship due to the complexity of reactions taking place in the cathode. Next, a simplified expression for the exchange current density is derived by parametric analysis of the over potential in the Butler-Volmer equation. Then conservation of charge is used to arrive at the charge transport equations, in terms of ionic/electronic potentials.

3.2 Theory and Model Derivation

The primary objective of an electrochemical model is to relate the ionic and electronic current to each other and properly represent the interfaces between them. Ionic current is transported in the form of ions ($Na^+, S_x^=$) within the electrode melts and through the electrolyte. Electronic current is transported in the form of electrons through the liquid sodium metal, the solid electrode materials (graphite in cathode, stainless steel in the anode) and the cell container. The direction of current flow depends on the potential across the cell with respect to the open circuit voltage (OCV) which is called the over potential (η). For the NaS battery (or any electrochemical cell in general), when the cell potential is less than the OCV, the anode species is oxidized, releasing electrons into the circuit. The newly formed cations (Na^+) are transported across the electrolyte and into

the cathode. Here the cations and anions ($S^{=}$) react and are reduced, absorbs electrons from the circuit in the process. For cell potentials greater than the OCV the opposite occurs.

3.2.1 Open Circuit Voltage (Nernst Equation)

The general expression for the Nernst potential or OCV is derived from Gibb's Free energy and Faraday's law (Equation (25)).

$$E_{OCV} = -\frac{\Delta G^0}{nF} - \frac{RT}{nF}\ln\left(\frac{a_{RED}}{a_{OX}}\right) \tag{25}$$

However, the chemical activities (a_{OX} and a_{RED}) for reactions in a sodium polysulfide melt are not well defined. This is due to the formation of multiple polysulfide species and the intermediate reactions which may occur. For example, when sodium is introduced in small concentrations to a sulfur melt, Na_2S_5 forms with free atomic sulfur. This is called the 2 phase region, and is present for melts where total weight percentage of sulfur is greater than 78.5% (Figure 2). As sodium is continually added, eventually the polysulfide reacts with sodium to form Na_2S_4, Na_2S_3 and so on. Because only polysulfide exists in the melt, this is called the single phase region. Experimental measurements by Gupta [25] and Cleaver [35] show that the Nernst potential is nearly constant in the two phase region and linearly dependent on concentration of total sulfur in the single phase region. This data is used to develop a piecewise function which describes the Nernst potential of the melt:

$$\begin{aligned} E_{OCV} &= E^0 - \left[\frac{0.305(DoD-0.5685)}{0.4315}\right] \quad V \text{ for } DoD > 0.5685 \\ E_{OCV} &= E^0 \quad V \qquad\qquad\qquad\qquad \text{for} DoD < 0.5685 \end{aligned} \tag{26}$$

Where the depth of discharge (DoD) is derived with respect to a composition of pure Na_2S_3 yielding Equation (27).

$$DoD = 2.092\frac{1 - W_S}{W_S} \tag{27}$$

Sudworth and Tilley use the data from Gupta and Cleaver to estimate $\Delta E^0 = 2.071\ V$. However, the data also shows that this value is dependent on temperature. Thermodynamic data from Knödler [36] is used to produce a linear relationship between the Nernst potential of pure sulfur and the temperature (Equation (28)).

$$E_{OCV} = T\frac{dE}{dT} + E^0 \quad V \tag{28}$$

Where $E^0 = 1.936\ V$ and $\frac{dE}{dT}$ is proportional to the entropy generation and will be discussed in Chapter 5. This is the equation which will be used to calculate open circuit voltage in this study.

3.2.2 Current Density

In order to model charge transport, an approach similar to that used by Kawamoto in [10] is taken. First, the equations will be derived within the cathode due to its complexity. The equation for the ionic flux or current density ($\vec{J}_i$) is expressed as Equation (29) as presented by Newman [39].

$$\vec{J}_i = -\sigma_i \nabla \phi_i - F(z_+ D_+ \nabla c_+ + z_- D_- \nabla c_-) \tag{29}$$

Which considers ion transport due to potential gradient as well as molecular diffusion due to concentration gradients. In NaS batteries, the ionic charge of the sodium cations $z_+ = 1$ and for sulfur anions $z_- = 2$ and the concentrations are related by $2c_+ = Xc_-$. These values combined with additional

equations for the diffusion coefficient and the transference number lead to an equation for the ionic flux in terms of the sodium ions. Additionally, because solid and gaseous phases also exist in the electrodes, the concentrations are multiplied by the volume fraction of liquid (ε_{liq}).

$$D = \frac{D_+ D_- (z_+ - z_-)}{z_+ D_+ - z_- D_-} \tag{30}$$

$$t_+ = \frac{z_+ D_+}{z_+ D_+ - z_- D_-} \tag{31}$$

$$\vec{J}_i = -\sigma_i \nabla \phi_i - \frac{1}{3} FD \frac{\left(2 + \frac{1}{X}\right) t_+ - \frac{1}{X}}{t_+ (1 - t_+)} \nabla \left(\varepsilon_{liq} c_+\right) \tag{32}$$

Electronic current is dependent only on the potential gradient in the electronic conductor, so the equation for electronic current density comes directly from Ohm's law (Equation (33)).

$$\vec{J}_e = -\sigma_e \nabla \phi_e \tag{33}$$

Conservation of charge (energy) is used to relate the ionic and electronic current via Equation (34).

$$\begin{gathered} \nabla \cdot \left(\vec{J}_i + \vec{J}_e\right) = 0 \\ \nabla \cdot \vec{J}_i = -\nabla \cdot \vec{J}_e = a_s i_F \end{gathered} \tag{34}$$

A continuum approach is taken for modelling the NaS battery. Because of this the electron conducting porous graphite mat and the ionic conducting sodium polysulfide occupy the same control volumes. Therefore, an exchange current density (i_F) must be calculated everywhere that there is liquid present. This can be calculated from the Butler-Volmer Equation [39]

$$i_F = i_0 \left[e^{\left(\frac{\alpha_a nF\eta}{RT}\right)} - e^{\left(\frac{\alpha_c nF\eta}{RT}\right)} \right] \quad (35)$$

Where the overpotential η is defined by Equation (36)

$$\eta = \phi_e - \phi_i - E_{OCV} \quad (36)$$

Ideal values are assumed for the charge transfer coefficients $\alpha_a = -\alpha_c = 0.5$ due to insufficient empirical data. Previous authors assumed that a linear relationship exists between the exchange current i_F and the overpotential η. In order to test the validity of this assumption, Equation (35) is solved for a range of overpotential at an arbitrary activation current density $i_0 = 1.0\ A/m^2$ and operating temperature of 335°C. The resulting exchange current is then plotted against the overpotential. For an overpotential range of -1 to +1 V, the relationship is clearly nonlinear as shown in Figure 10.

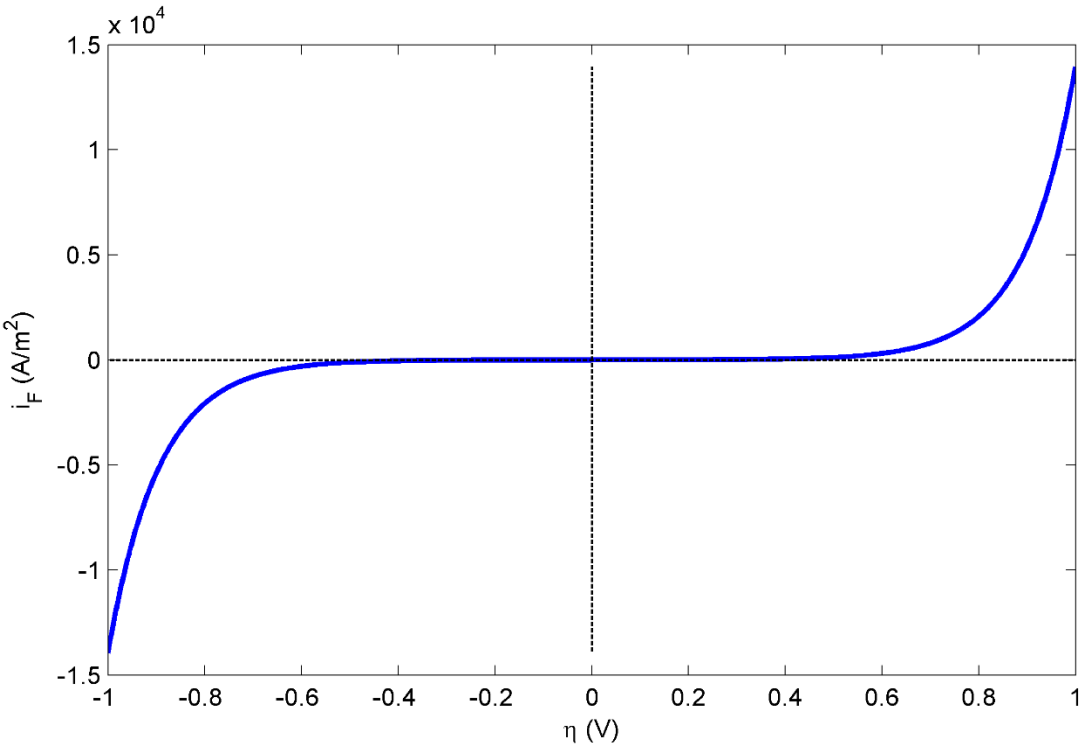

Figure 10 – Analysis of overpotential/exchange current relationship using Butler-Volmer for $-1.0 < \eta < +1.0\ V$

However, previous models have predicted a much smaller range of overpotentials to occur. For high current density operation, Kawamoto's steady state model is used to predict a maximum overpotential of $\eta \approx 0.075\ V$ in the cathode and an average overpotential on the order of $\eta \approx 0.001\ V$. Transient models predict that the overpotential gradient actually decreases during cell operation. Therefore, a better range of overpotential to evaluate is determined to be $-0.1 < \eta < +0.1\ V$ (Figure 11). A linear approximation for this range of overpotentials exhibits minimal error.

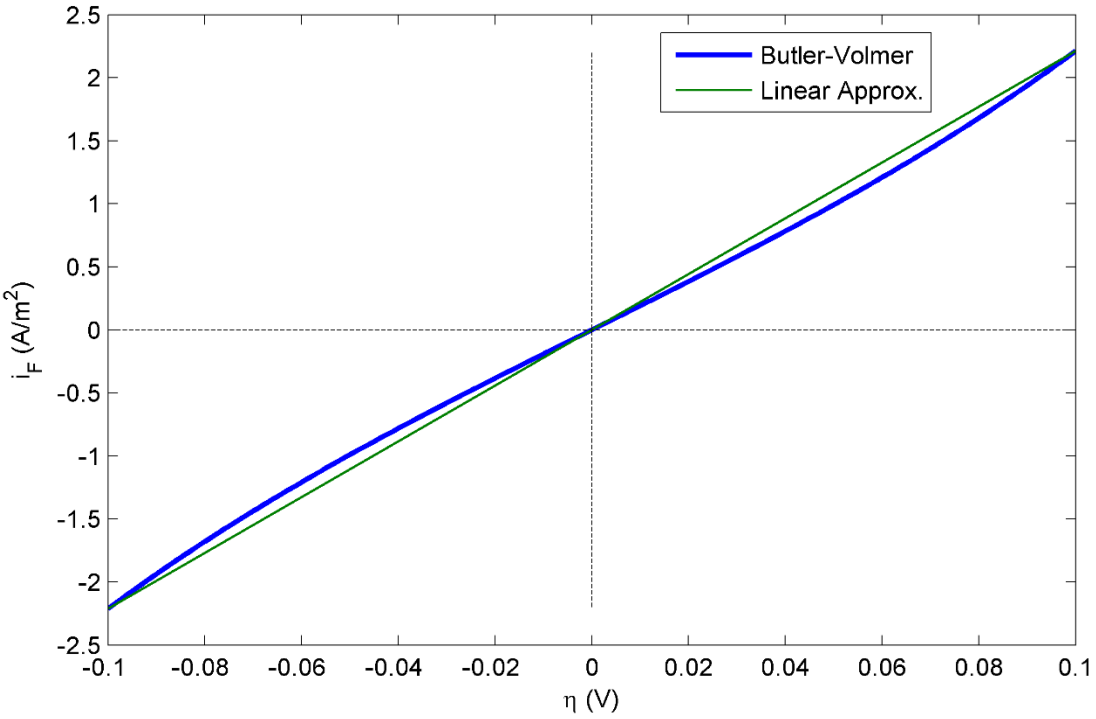

Figure 11 – Analysis of overpotential/exchange current relationship using Butler-Volmer for $-\mathbf{0.1} < \boldsymbol{\eta} < +\mathbf{0.1}\ \boldsymbol{V}$

From this analysis, it is assumed that a linear relationship between the overpotential and exchange current density is appropriate. Therefore, the Butler-Volmer equation becomes:

$$i_F = i_0 \frac{F}{RT}\eta = \frac{1}{K_{p,T}T}\eta$$
$$K_{p,T} = \left(i_0 \frac{F}{R}\right)^{-1} \ (\Omega\, m^2/K) = \text{constant} \tag{37}$$

Where $K_{p,T}$ is similar to the surface polarization term K_p suggested by Kawamoto and Wada [8] [9] [10] [33] with the temperature kept out so that temperature dependence is maintained.

3.2.3 Charge Transport

Equation (34) is updated by Equations (36) and (37) to produce Equation (38).

$$\nabla \cdot \vec{J}_i = -\nabla \cdot \vec{J}_e = \frac{a_s}{K_{p,T}T}(\phi_e - \phi_i - \Delta E_{OCV}) \tag{38}$$

This equation is now combined with the Equations (32) and (33) to yield the set of charge transport equations for the ionic and electronic conducting phases within the cathode (Equations (39) and (40) respectively).

$$\begin{aligned} -\nabla \cdot (\sigma_i \nabla \phi_i) + \frac{a_s}{K_{p,T}T}\phi_i \\ = \frac{a_s}{K_{p,T}T}(\phi_e - \Delta E_{OCV}) + F\nabla \cdot \left[D_{eff}\nabla c_+\right] \end{aligned} \tag{39}$$

$$-\nabla \cdot (\sigma_e \nabla \phi_e) + \frac{a_s}{K_{p,T}T}\phi_e = \frac{a_s}{K_{p,T}T}(\phi_i + \Delta E_{OCV}) \tag{40}$$

Where:

$$D_{eff} = \frac{1}{3}D\frac{\left(2 + \frac{1}{X}\right)t_+ - \frac{1}{X}}{t_+(1 - t_+)}$$

Given values or empirical equations for the transport properties as well as the concentration and temperature fields, these equations can now be discretized and solved numerically. Notice that the derived charge transport equations are not directly dependent on time. However, temperature and sodium concentration do have time dependent equations, as will be discussed later. Therefore, by updating the species concentration, temperature field and properties as a function of time, a transient solution will be produced.

Within the solid electrolyte no electronic current is present ($\vec{J}_e = 0$) so only one equation is required to solve the charge transport. Because the electrolyte is a solid, no molecular diffusion will take place. Combining these conclusions with Equations (32) and (34) yields the charge transport equation for the electrolyte:

$$-\nabla \cdot (\sigma_i \nabla \phi_i) = 0 \tag{41}$$

Charge transport in the anode can also be simplified. Because only one phase is present in the anode melt (sodium) diffusion due to concentration gradients will not occur. Also, because sodium is an electron conductor, there is no ionic current except at the anode/electrolyte interface, which can be applied as a boundary condition. These considerations combined with Equations (33) and (34) gives the charge transport equation for the anode:

$$-\nabla \cdot (\sigma_e \nabla \phi_e) = 0 \tag{42}$$

Chapter 4: Mass Transport Modelling

4.1 Introduction

Mass transport in an electrochemical system is strongly dependent on potential gradient, due to the high concentrations of ions within the electrode melts. The depletion and accumulation of species concentrations due to reaction at the electrolyte and solid electrode surface and the migration due to potential gradient cause gradients in species concentration to occur. Therefore, diffusion becomes important.

In the case of NaS batteries, the liquid electrode materials are suspended in solid porous mediums with an inert gas (such as argon) filling the open space. Because of this, capillary action becomes another primary source of mass transport. Gravity must also be considered, as it is an opposing force to vertical capillary motion and the primary cause of saturation (liquid concentration) gradients in the vertical direction. Otherwise, the liquid concentration within the media would likely be constant in the vertical direction.

4.2 Theory and Derivation Part 1- Species Transport in Electrode Melts

For this part of the model derivation, only the transport that occurs within the liquid phase and solid electrolyte will be considered. Transport of the liquid itself will be modelled separately as described in the following section. The mole fraction of sodium within the anode melt is always unity, as only liquid sodium is present. The cathode melt contains a mixture of sodium, sulfur and sodium polysulfide.

Rosen and Tegmam [40] have shown that for certain temperatures concentrations, sodium polysulfide does not exist in molecular form but rather as an ionic liquid containing a mixture of sodium, free sulfur and sulfur ions. This is true for total sulfur mass concentrations greater than 67.6% compared to sodium (Figure 2) or in other words, for $x \geq 3$ in Na_2S_x, which is also the operational limit of the NaS battery. Below this concentration, solid precipitation of Na_2S_2 and Na_2S occurs.

Cleaver and Davies [35] performed experiments which measured the electromotive force (EMF) of the NaS cathode in order to explore the transport behavior of sulfur/sodium polysulfide melts. The EMF was measured for the formation of free sulfur (E_S) and for the formation of a sulfur ion ($E_=$). These values were then compared to the EMF of the sulfur in a polysufide melt ($E_{S_{Na}}$), which was estimated from experiments performed on a cell containing two sulfur electrodes and a sodium electrode. Please refer to the publication for details on the experimental procedure. The behavior of the melt is bound by two limiting cases:

1. The melt behaves as if sulfur is contained within polysulfide ions ($S_3^=, S_4^=$ and so on) and migrates with the ionic current. For this to be true, $E_{S_{Na}} = E_=$
2. The melt behaves as if some free sulfur is present and does not migrate relative to the ionic transport of sodium (Na^+) and monosulfide ($S^=$). For this to be true, E_{Na} is between E_S and $E_=$.

The measured values of the EMF are listed in

Table 2 – EMF Measurements on the Sodium-Sulfur Cell at 360°C [35]

E_S	72 mV
$E_=$	281 mV
$E_{S_{Na}}$	273.5±2.5 mV

Because $E_{S_{Na}}$ is within 5 to 10 mV of $E_=$ and 200 mV away from E_S, it is concluded that case 1 is true and all sulfur migrates with the ionic current. Therefore, the migration velocity of total sulfur migrates relative to sodium. This means that only two equations are required to solve for species transport. Starting with the transport equations for a binary electrolyte, without convection:

$$\frac{\partial}{\partial t}\left(\varepsilon_{liq} c_+\right) = \frac{t_+}{z_+ F} \nabla \cdot (\sigma_i \nabla \phi_i) + \nabla \cdot \left[D_{eff} \nabla\left(\varepsilon_{liq} c_+\right)\right] \qquad (43)$$

$$\frac{\partial}{\partial t}\left(\varepsilon_{liq} c_-\right) = \frac{1 - t_+}{z_- F} \nabla \cdot (\sigma_i \nabla \phi_i) + \nabla \cdot \left[D_{eff} \nabla\left(\varepsilon_{liq} c_-\right)\right] \qquad (44)$$

Risch and Newman [40] calculated the value of the transference number for sodium polysulfides at different temperatures and concentrations. Extrapolating the data, for the operating conditions of a typical NaS cell the transference number of sodium falls within the range $0.93 < t_+ < 1.0$. Previous authors have used this as justification to assume that $t_+ = 1.0$. Additionally, the concentrations are related in terms of X so the concentration transport within the melt would reduce to Equations (45) and (46).

$$\frac{\partial}{\partial t}\left(\varepsilon_{liq} c_+\right) = \frac{1}{F} \nabla \cdot (\sigma_i \nabla \phi_i) + \nabla \cdot \left[D_{eff} \nabla\left(\varepsilon_{liq} c_+\right)\right] \qquad (45)$$

$$\frac{\partial}{\partial t}\left(\varepsilon_{liq} c_{-}\right) = \nabla \cdot \left[D_{eff} \nabla \left(\varepsilon_{liq} \frac{X}{2} c_{+}\right)\right] \tag{46}$$

Equation (39) contains similar terms to Equation (45) and can be rearranged as so:

$$\nabla \cdot (\sigma_i \nabla \phi_i) + F \nabla \cdot \left[D_{eff} \nabla c_{+}\right] = \frac{a_s}{K_{p,T} T} (\phi_i - \phi_e + \Delta E_{OCV}) \tag{47}$$

What is shown is that if the transference number is assumed to be unity, the change in sodium concentration density is proportional to the exchange current density (Equation (37)) by Faraday's constant. This means that the rate of change of sodium concentration can be calculated directly from the exchange current density:

$$\frac{\partial}{\partial t}\left(\varepsilon_{liq} c_{+}\right) = \frac{1}{F} \frac{a_s}{K_{p,T} T} (\phi_i - \phi_e + \Delta E_{OCV}) \tag{48}$$

The validity of these assumptions will be discussed further in Chapter 6. The model is written to solve the discretized versions of equations (43) and (44) implicitly. There is also a built in option which calculates the concentrations at each time step explicitly from equations (46) and (48) for $t_+ = 1.0$.

In the electrolyte, only sodium is present, but a concentration gradient will occur due to the potential gradient. Molecular diffusion is neglected so Equation (45) reduces to Equation (49) in the electrolyte.

$$\frac{\partial}{\partial t}(c_{+}) = \frac{1}{F} \nabla \cdot (\sigma_i \nabla \phi_i) \tag{49}$$

4.3 Theory and Derivation Part 2- Porous Media Flow

When two different fluids (usually immiscible) are in contact with a solid surface one fluid will be favorably attracted to the solid surface [41] due to differences in their wetting properties. This fluid is designated as the wetting phase while the other is called the non-wetting phase. Surface tension between the wetting phase and the solid results in a pressure differential across the interface of the two fluid phases [41]. Within the pores of a porous media, this pressure different results in the wetting phase advancing into the region occupied by non-wetting fluid and displacing it. This pressure is defined as the capillary pressure (p_c), and accounts for the capillary action. Capillary pressure in an individual pore is dependent on the effective pore radius (r_c), surface tension of wetting phase (γ) and wetting angle between solid and wetting phases (ψ) with respect to the non-wetting phase (Equation (50)) [41].

$$p_c^0 = \frac{2\gamma \cos(\psi)}{r_c} \tag{50}$$

Within a continuum where properties are averaged locally, capillary pressure has been shown to have an additional dependence on phase concentration (or more conveniently saturation) [41]. Saturation of a particular fluid is defined as the percent of pore volume occupied by this fluid. Assuming that the wetting phase is a liquid and the non-wetting phase is a gas, the saturations of the wetting phase (S_w) and the non-wetting phase (S_n) in a two fluid phase system are defined by Equations (51-(53.

$$S_w = \frac{1}{\varepsilon_{por}} * \frac{\varepsilon_{liq}}{\varepsilon_{liq} - \varepsilon_{gas}} \tag{51}$$

$$S_n = \frac{1}{\varepsilon_{por}} * \frac{\varepsilon_{gas}}{\varepsilon_{liq} - \varepsilon_{gas}} \quad (52)$$

$$S_n = (1 - S_w) \quad (53)$$

It has been determined experimentally that the dependence of capillary pressure on saturation is exponential with hysteresis depending on the initial conditions and residual saturations [41]. Residual saturations (S_{rw} and S_{rn}) are attributed to trapped portions of the wetting phase or non-wetting phase within the pores during depletion or addition of the wetting phase respectively [41] and depend on the composition and homogeneity of the medium. Multiple models [42] [43] [44] [45] [46] have been developed to calculate the capillary pressure as a function of a normalized saturation (S_0) which takes into account residual saturations that may occur for each liquid phase (Equation (54)).

$$S_0 = \frac{S_w - S_{rw}}{1 - S_{rw} - S_{rn}} \quad (54)$$

With the capillary pressure field, velocity can be calculated using Darcy's law (Equation (55)). This equation is derived from Stokes equation that is valid for $Re \ll 1$ as is typical in porous media flow [41].

$$\vec{u}_\alpha = \frac{\vec{k}_0 k_{rw}}{\mu_\alpha}\left(\vec{\nabla} P_\alpha\right) \quad (55)$$

Where $\vec{u}_\alpha$, μ_α, P_α and ρ_α are the pore velocity, viscosity, total pressure and density of phase α while $\vec{k}_0$, k_{rw} and $\vec{g}$ are the permeability tensor, relative permeability coefficient and gravity vector (which can also contain an applied pressure gradient). The total pressure gradient of a particular fluid phase is the combination of the capillary pressure gradient, the pressure gradient due to gravity and the pressure due to buoyancy forces.

$$\vec{\nabla}P_\alpha = \vec{\nabla}p_{\alpha,c} - \vec{\nabla}p_{\alpha,g} \quad (56)$$

Previously developed porous media flow models [41] [47] do not consider the buoyancy forces in this manner. It was found during this study that neglecting the buoyancy which counteracts gravity causes two problems. First, when gravity is involved the resulting pressure gradient sometimes leads to a velocity field which violates the mass conservation law. Second, low density fluids are able to penetrate deeply into high density fluids by means of capillary motion with no force to prohibit such motion, which is not physically accurate. In order to derive a proper relation between gravity, buoyancy and pressure gradient, a force balance is performed inside a volume element containing a fluid displacing another fluid (Figure 12) with the y-coordinate oriented in the direction of gravity.

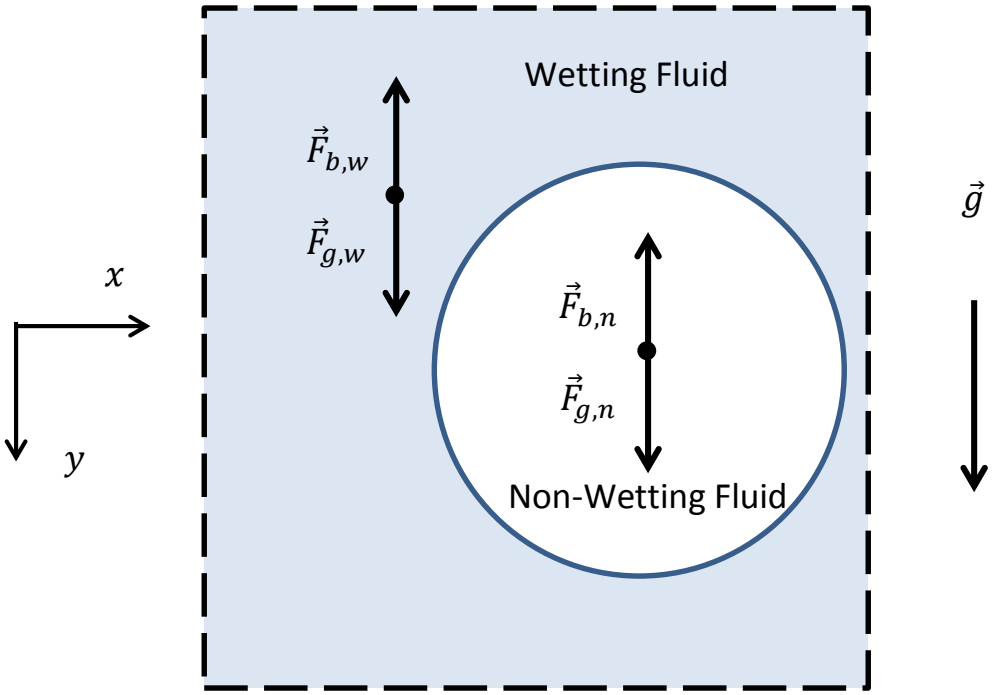

Figure 12 – Gravitational and Buoyancy force diagram

It is assumed that the illustrated system is not static, such that the forces are not balanced and the fluids are accelerating with respect to one another. As

the heavier fluid is displaced in the direction of the gravitational field, the lighter fluid will accelerate in the opposite direction. From Newton's second law of motion we know that the accelerations must be equal and opposite (Equation (57)).

$$\Sigma\vec{F}_w = m\vec{a}_w = -m\vec{a}_n = -\Sigma\vec{F}_n$$
$$\Sigma\vec{F}_w = \vec{F}_{b,n} - \vec{F}_{g,n} \tag{57}$$

$$\Sigma\vec{F}_w = \rho_w\vec{g}\partial V_n - \rho_n\vec{g}\partial V_n \tag{58}$$

Because the volumes are proportional to the saturations ($V_w = S_w V_{total}$) and $S_n = 1 - S_w$:

$$\Sigma\vec{F}_w = (1 - S_w)(\rho_w - \rho_n)\vec{g}\partial V \tag{59}$$

This force is converted into a pressure by dividing by the differential cross sectional area normal to the direction of the force. In the three dimensional case where $\partial V = \partial x\,\partial y\,\partial z$ with the area normal to the gravitational force being $\partial\vec{A} = \partial x\,\partial z$ the pressure gradient due to gravity and buoyancy is derived. Dividing by the normal area vector and taking the gradient of Equation (59) yields:

$$\vec{\nabla}p_{w,g} = (1 - S_w)(\rho_w - \rho_n)\vec{g} \tag{60}$$

The modified version of Darcy's law which properly accounts for gravity and buoyancy for a two fluid phase system for the wetting fluid is shown in Equation (61):

$$\vec{u}_w = \frac{\vec{k}_0 k_{rw}}{\mu_w}\left(\vec{\nabla}p_{w,c} + (1 - S_w)(\rho_w - \rho_n)\vec{g}\right) \tag{61}$$

These velocities are then used to solve the mass transport of the wetting and non-wetting fluids with respect to each other by use of the saturation equation (Equation (62)). This equation comes directly from the mass conservation equation [41].

$$\frac{\partial}{\partial t}\left(\rho_\alpha S_\alpha \varepsilon_{por}\right) = \vec{\nabla} \cdot [\rho_\alpha \vec{u}_\alpha] \tag{62}$$

Equations (55) and (62) are combined to form the transport equation which is to be solved (Equation (63)). This is written specifically for the wetting phase ($\alpha \rightarrow w$) as the saturation of the non-wetting phase is calculated directly from Equation (63), where $p_w = p_n - p_c$

$$\frac{\partial}{\partial t}(\rho_w S_w \phi) = \vec{\nabla}\left[\frac{\rho_w \vec{k}_0 k_{rw}}{\mu_w}\left(\vec{\nabla} p_{w,c} + (1 - S_w)(\rho_w - \rho_n)\vec{g}\right)\right] \tag{63}$$

4.2.1 Porous Media Flow Modelling

Flow of the wetting phase within the solid medium with respect to the non-wetting phase is modeled using a continuum approach. However, in order to close the system, a model must be chosen for the pressure gradient as well as the relative permeability. As mentioned previously, multiple models have been developed for the capillary pressure gradient, however some models were developed specifically for underground aquifers and oil reservoirs so are derived with respect to typical rock and soil properties. The model chosen for this study has also been one implemented by Hoteit [47]. It is determined appropriate because it takes into account heterogeneous permeability in addition to normalized saturation (Equation (64))

$$\vec{\nabla} p_c = \frac{p_c^0}{\sqrt{\nabla \cdot \vec{k}_0}} \ln(S_0) \tag{64}$$

For the relative permeability, power type functions of the normalized saturation (Equation (65)) have been hypothesized [42] [46] [48]. Similar to capillary pressure models, this relationship is based on experimental observations as a theoretical relation has not been clearly defined.

$$\begin{aligned} k_{rw} &= (S_0)^n \\ k_{rn} &= (1 - S_0)^{\frac{n}{2}} (1 - S_0^{\frac{n}{2}}) \end{aligned} \tag{65}$$

In this study, a value of $n = 4$ is used in Equation (65) as which will be referred to as the relative permeability sub-model. This value was determined by theoretical and experimental studies by Leverett [49] Brooks and Corey [50]. This closes the system which can now be solved numerically.

4.2.2 Porous Media Model Verification

The saturation equation is discretized via the finite volume method in three dimensions and solved in a time marching fashion. The code is capable of implementing 1st order Euler's as well as 2nd and 4th order Runga-Kutta solution methods. Normalized saturation, relative permeability and capillary pressure are updated at each time step. A staggered grid is used to avoid checker-boarding of the pressure gradient and to maintain mass conservation.

Model Verification Example 1

The model is verified by comparing the numerical results to analytical solutions in a similar procedure to the one used by Hoteit et al [47]. For simplicity, these verifications are performed in a 1-dimensional domain. In these examples,

flow is simulated within an idealized (homogenous) paper membrane which is 5 cm in length, 4 mm wide and 1 mm thick.

The first example is the solution of the Buckley Leverett problem [51] with a sharp moving interface between the wetting phase (water) and non-wetting phase (air) due to applied pressure gradient. The purpose of this verification is to show that the discretized form of the equations properly handles applied pressure and sharp concentration gradients without numerical diffusion. The capillary pressure that normally causes a gradient between the saturations of the two phases is ignored. At $t = 0$ the domain is fully saturated by the non-wetting phase with an applied injection of wetting phasing at the rate of $Q = 0.05$ Pore Volume/s (PV/s) at $x = 0$ cm. Other parameters are listed in Table 3. A comparison between the exact solution and numerical solution is shown in Figure 13.

Table 3 - Parameters for Example 1

Permeability	k_0	0.1	md
Porosity	ϕ	0.2	
Residual Saturations	S_{rn}	0.2	
	S_{rw}	0	
Mesh size	n_x	80	cells

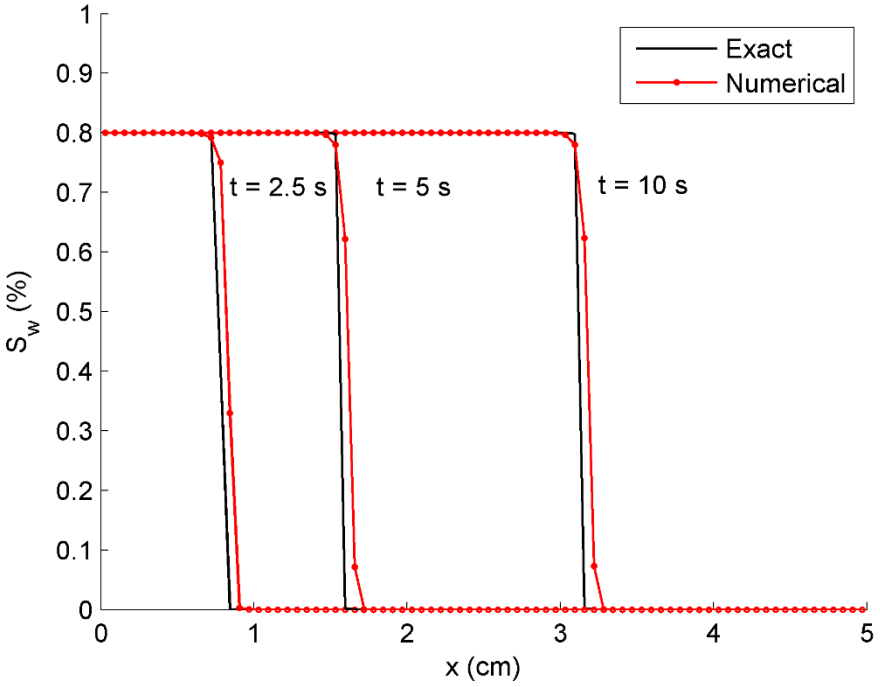

Figure 13 – Model verification part 1, Buckley-Leverrett problem

As shown in Figure 13, the numerical results closely agree with the exact solution of a sharp moving front. This simplified model handles the high saturation gradient without instabilities and with no apparent accumulation in error. In fact, the performance of this model is comparable to the more sophisticated model applied by Hoteit et al [47]. Additionally, No discernable amount of numerical diffusion takes place over time.

Model Verification Example 2

For the second test case, the semi-analytical solution derived by Van Dujin and Neef [52] is used to verify that permeability and capillary pressure flow sub-models have been properly applied. It is called semi-analytical because no exact solution exists for the capillary pressure or relative permeabilities. The solution of the saturation equation is solved as a similarity solution of the one dimensional

partial differential equation. Please refer to Van Dujin and Neef's publication for more details.

The geometry for this example is similar to that used in the first example, but with the two immiscible fluids having identical wetting properties. This way, it can be demonstrated that the model is capable of handling an application with two similar fluids while also verifying the permeability and capillary pressure models. The initial saturation of the left half ($0.0 \leq x < 2.5$ cm) of the media is assumed to be fully saturated with the wetting phase while the right side ($2.5 \leq x \leq 5$ cm) is saturated with what is called the non-wetting phase, even though wetting properties are similar for both phases. Other data relevant to this example are shown in Table 4 with a comparison to the semi-analytical solution shown in Figure 14.

Table 4 - Parameters for Example 2

Permeability	k_0	0.5	md
Porosity	ϕ	0.25	
Residual Saturations	S_{rn}	0	
	S_{rw}	0	
Mesh size	n_x	100	cells

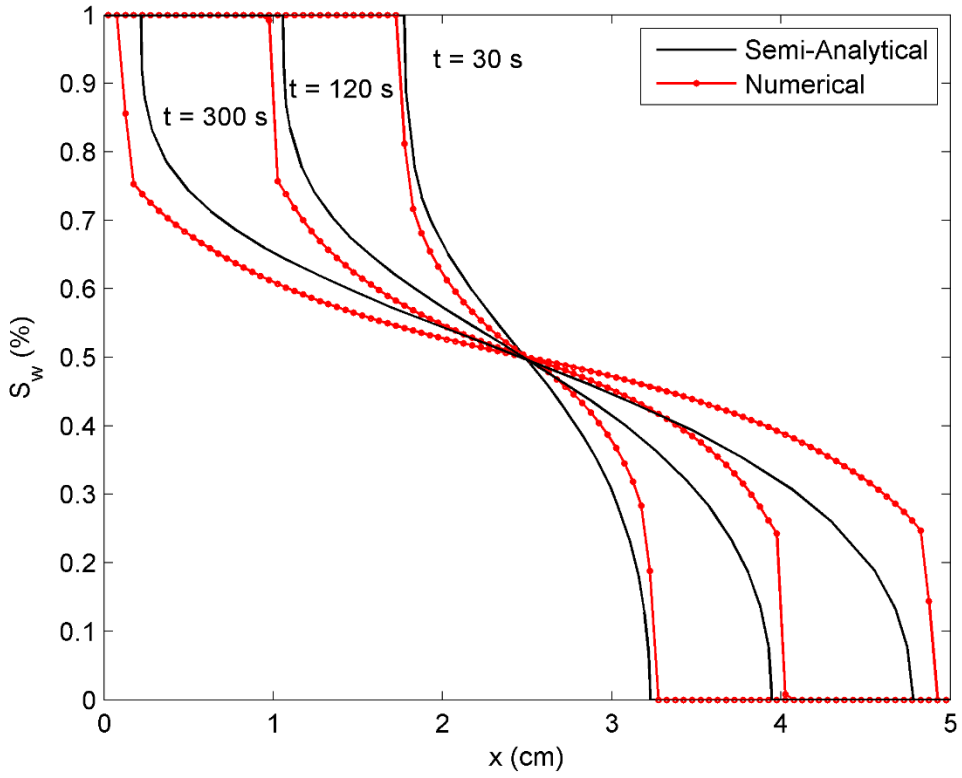

Figure 14 – Model verification part 2, Van Dujin-Neef problem

The numerical data shows good agreement with the semi-analytical data. Each solution shares an inflection point at 50% saturation and at the midpoint of the domain ($x = 2.5\ cm$) for each point in time, which implies that the additional wetting of the media by the non-wetting phase is being modelled properly (as the solution should be symmetric). There appears to be some numerical diffusion occurring over time which is causing the fronts of the interface to move slightly faster than expected. It is possible that the error could be reduced by refining the mesh or decreasing the time step, which will be studied later.

Model Verification Example 3

In order to demonstrate the ability of the model to handle a heterogeneous media, a 2D heterogeneous media flow problem which was previously modeled by Hoteit et al [47] is simulated. A domain with dimensions of 500 x 270 x 1 meters with horizontal (x direction) layers of alternating high (100 md) and low (1 md) permeabilities which are 30 m thick. Nine layers are distributed vertically (y direction) with five having high permeability. The media is initially fully saturated by the non-wetting phase. An injection rate of 0.11 PV/year is applied at $x = 0$. Two cases are performed; case (a) which ignores capillary pressure and case (b) which does not. The simulations of these cases are carried out until the wetting fluid fills 50% of the total pore volume. The resulting contours of wetting phase saturations at this time are shown in Figure 16 and Figure 17 respectively. Other parameters are shown in Table 5. Additional details about this problem and analogous results can be found in the paper by Hoteit [47].

Table 5 - Parameters for Example 3

Porosity	ϕ	0.20	
Residual saturations	S_{rn}	0	
	S_{rw}	0	
Mesh size	n_x	50	cells
	n_y	90	cells
Wetting fluid	Water		
Non-wetting fluid	Oil		

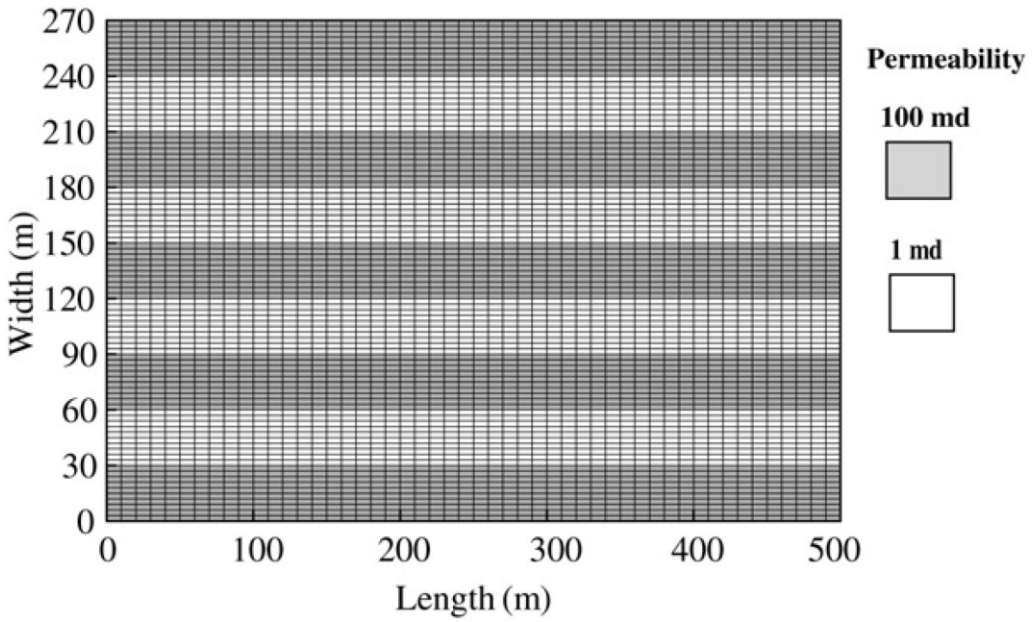

Figure 15 – Domain and permeability distribution for Example 3 (a) and (b) from publication by Hoteit [47]

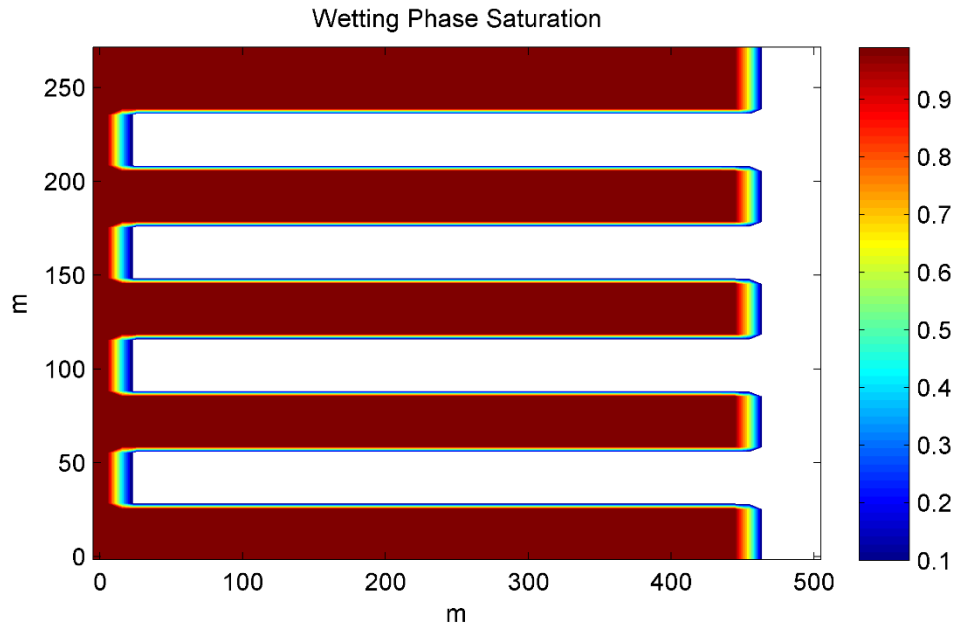

A

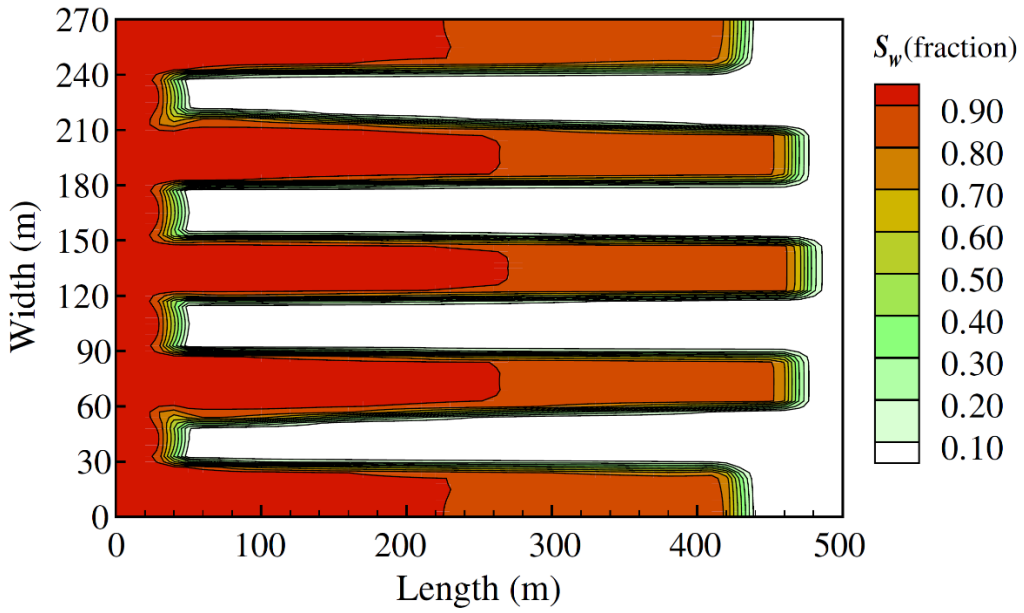

B

Figure 16 – Example 3(a), A: Results from the newly developed model and B: results from model by Hoteit et al [47]

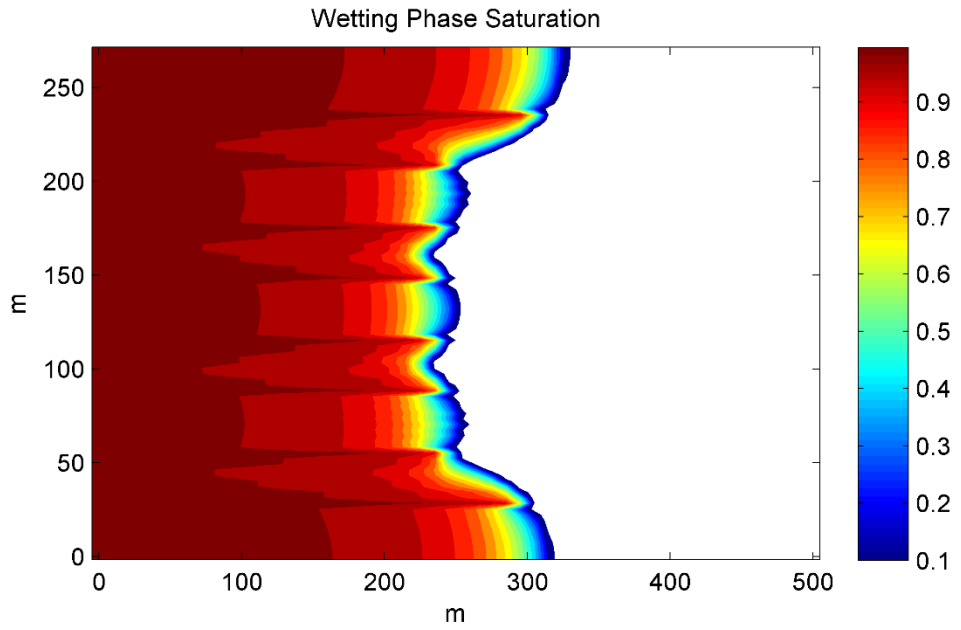

A

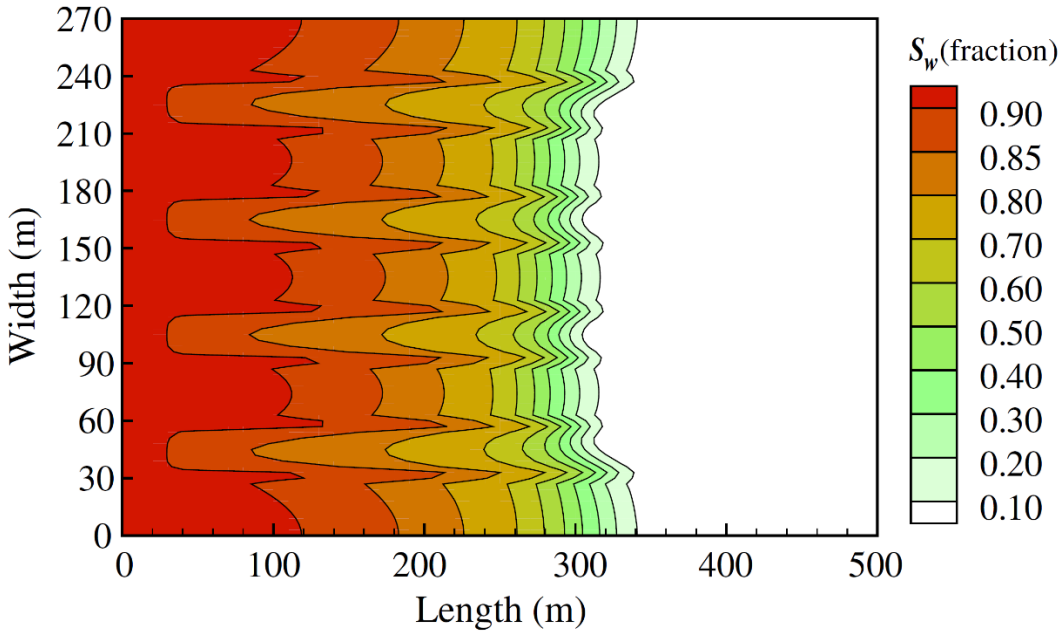

B

Figure 17 – Example 3(b), A: Results from the newly developed model and B: results from model by Hoteit et al [47]

A comparison between the results from the literature (Figure 16B and Figure 17B) and the present model (Figure 16A and Figure 17A) show similarly shaped interfaces between the fluids, which is particularly significant for the complex shape of the flow front produced by case (b). It could be argued that the current model handles case (a) better than the model from the literature. For the model used in this study, no substantial gradient forms between the saturated and wetting phases, as is characteristic of a zero capillary pressure case. Hoteit's results show a steady decrease in wetting phase saturation from left to right before the sharp interface is reached. Therefore, it is concluded that the model developed in this study is capable of handling both simple and complex porous media flow at a level similar to other more sophisticated models.

Analysis of dependence on time step and grid resolution

First, it is necessary to explain the stability criteria of the model. In a typical convection problem, the discretized 1D equation for the explicit solutions is:

$$\varphi(x, t + \Delta t) = \varphi(x, t) + \frac{u\Delta t}{\Delta x}(\varphi(x + \Delta x, t) - \varphi(x - \Delta x, t) \qquad (66)$$

The stability criteria is that $\frac{u\Delta t}{\Delta x} \leq 1$ (Courant number). For the 1D porous media flow case, Equation (63) becomes Equation (67)

$$S_w(x, t + \Delta t) = S_w(x, t) + \frac{\Delta t}{\mu \Delta x^2 \varepsilon}\Delta(k_{rw} k_0 p_w) \qquad (67)$$

Notice here that the transport variable S_w does not appear in the right hand side of the equation directly. Where it come into play is within the pressure

gradient. Assuming no other pressure gradients are present this relationship is as follows:

$$\Delta p_w = \Delta p_c = \Delta\left[\frac{p_c^0}{\sqrt{\nabla \cdot \vec{k}_0}}\ln(S_0)\right] = \Delta\left[\frac{p_c^0}{\sqrt{\nabla \cdot \vec{k}_0}}\ln\left(\frac{S_w - S_{rw}}{1 - S_{rw} - S_{rn}}\right)\right] \tag{68}$$

So the discretized form of the equation written out completely would involve the wetting saturation as part of a logarithmic function. Therefore, there is not straightforward way to define the stability criteria. However, it is apparent that there is a dependence similar to the diffusion equation on $\Delta t/\Delta x^2$. In other words, to maintain stability when increasing the grid resolution by a factor of 10, the time step must be decreased by a factor of 100.

With this in mind, the analysis of the grid resolution is performed. Example two is repeated for multiple time steps and grid resolutions in order to perform dependency studies. Grids of 75, 150 and 300 elements are applied and simulated with a time step of 0.001 s. The wetting phase saturation is plotted at 120 s for each of these cases and compared to the semi-analytical solution (Figure 18).

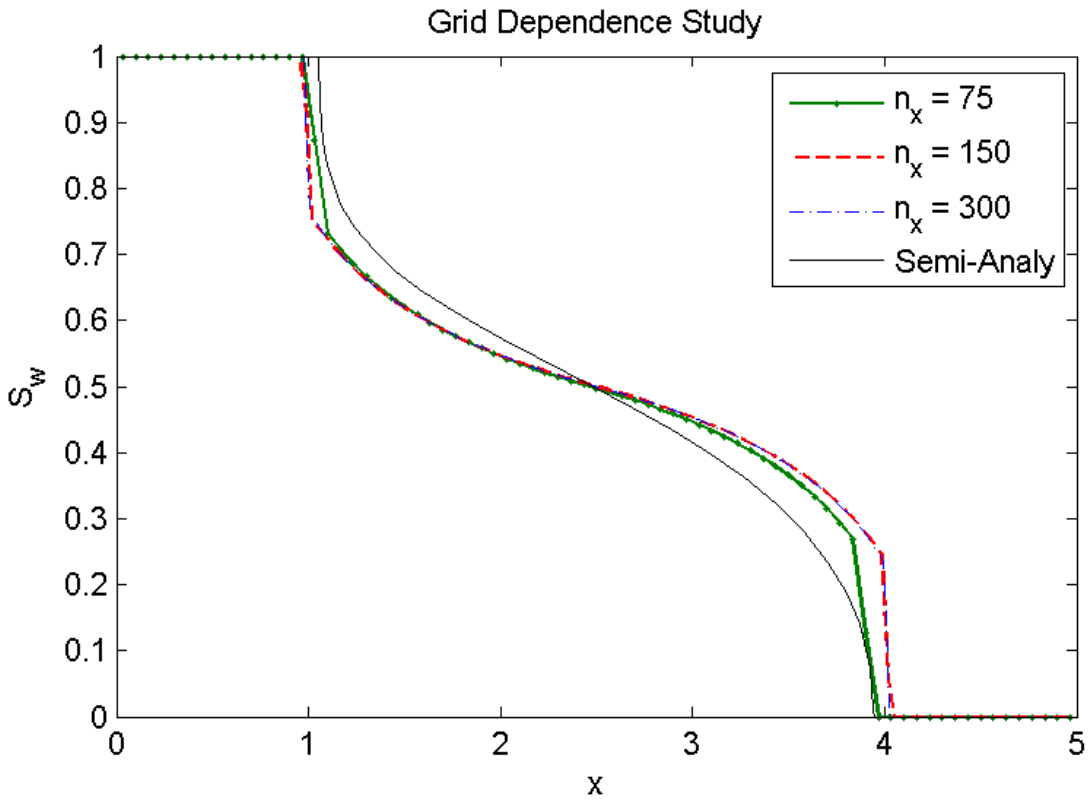

Figure 18 - Porous media model grid dependence study - Example 2 profile plotted at $t = 120\ s$

Interestingly, increasing the grid resolution from 75 to 150 moves the profile slightly away from the semi-analytical solution. Increasing further to 300 elements yields results practically identical to the 150 element case. Another observation is that the 75 element case is not as symmetric as the other solutions. Without changing the time step, grids larger than 300 elements produced unstable solutions while grids smaller than 75 elements experienced no transport due to the right hand side of the equation going smaller than the machine accuracy (Figure 19). It is determined based on these comparisons that the grid resolution has a negligible effect on the numerical model as long as there is stability.

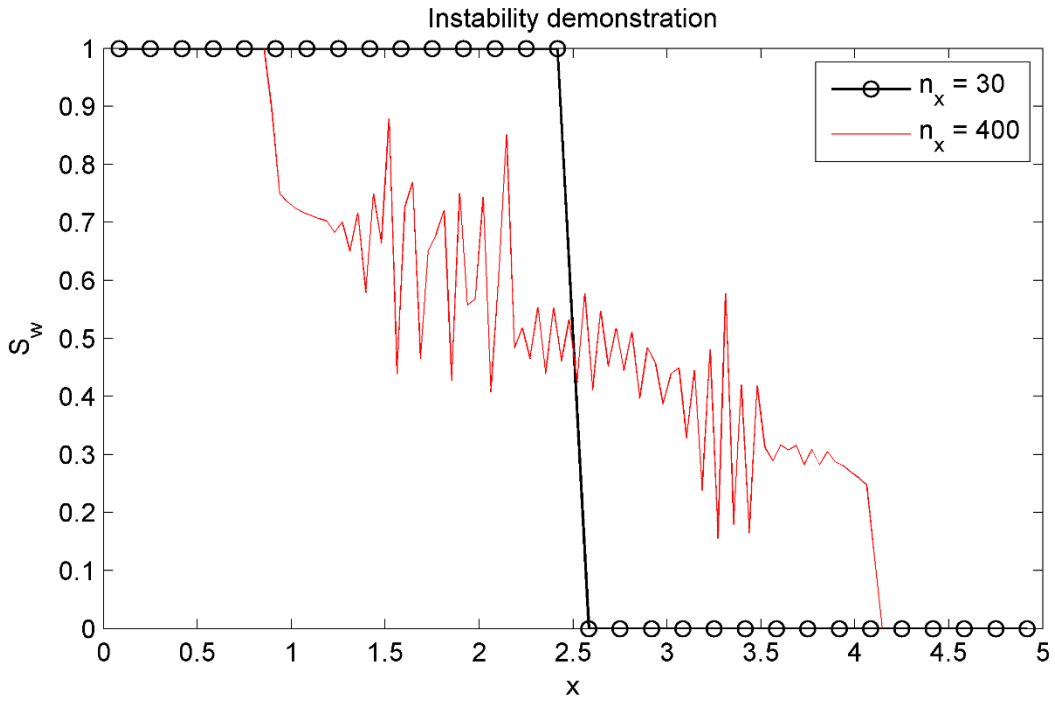

Figure 19 - Porous media model instability demonstration – Example 2 profiles plotted at $t = 120\ s$

A similar study was performed for time steps of 0.05, 0.005 and 0.0005 s all at the same grid resolution (Figure 20).The solutions at each of these time steps are indistinguishable from one another, so the dependence on the time step is assumed negligible. Time steps larger than 0.05 s produced unstable results.

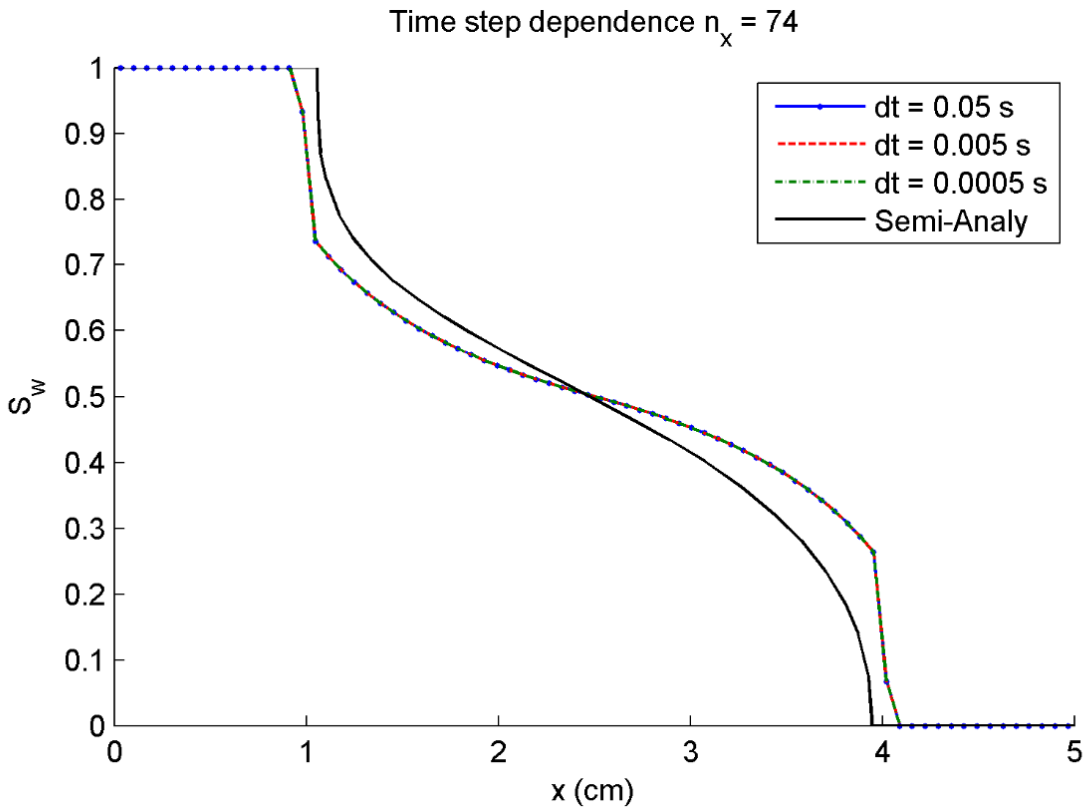

Figure 20 – Porous media model time step dependence study, Example 2 profile plotted at $t = 120\ s$

4.2.3 Porous Media Flow Model Validation

Simple experiments were performed on lateral flow test strips (LFTS) manufactured by EMD Millipore Corp. in order to validate the physical accuracy of the porous media flow model. Credit for performing these experiments goes to Xuefei Gao and Dr. Nick Wu from the MAE department at WVU [53]. The test section of the strip consists of a nitrocellulose membrane 25 mm long, 4 mm wide and 0.185 mm thick with a specified porosity of $\varepsilon_{por} = 0.23$. Sample and absorption pads located on either end of the membrane made of glass fibers act as the source and sink reservoirs of the wetting fluid (distilled water) respectively. These reservoirs have dimensions of 17x4x1 mm and a specified porosity of

$\varepsilon_{por} = 0.60$. These components as well as others that were neglected by the model are outlined in Figure 21.

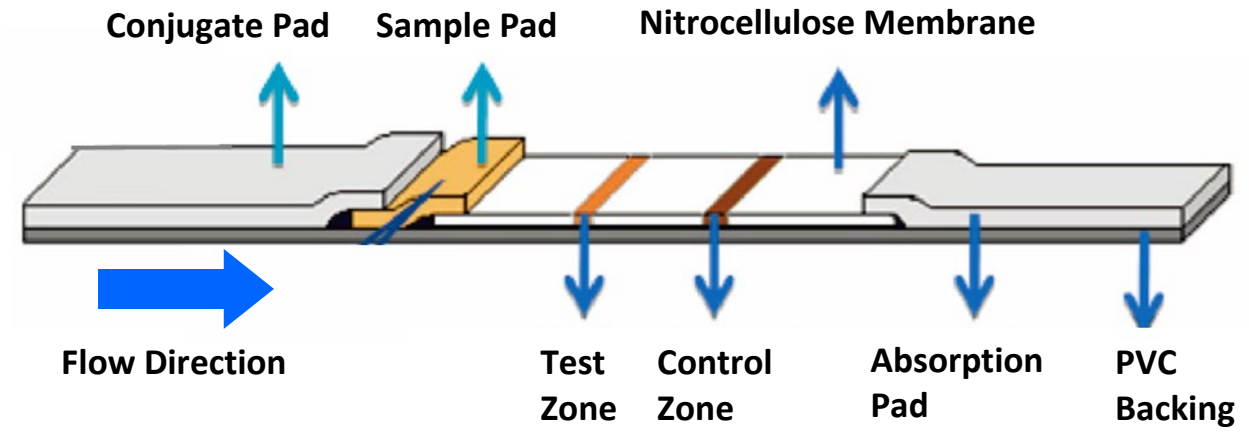

Figure 21 – Illlustration of Millipore LFTS components. Figure credit goes to Gao and Wu [53]

Values for the wetting angle at the water/nitrocellulose interface (ψ), average pore size (r_c) and tortuosity (τ) were obtained from the official specification sheet provided by Millipore [54] and from the literature [55]. For validation of the pore size and porosity, an image analysis was performed on a photograph taken by a scanning electron microscope (SEM) (Figure 22).

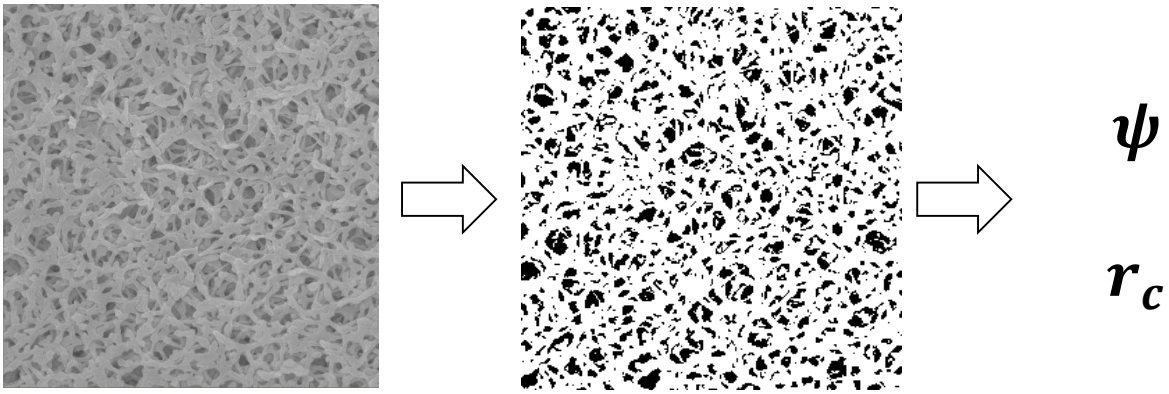

Figure 22 – SEM image analysis of nitrocellulose membrane

This was done by converting the image to black (pore) and white (fiber) which are colors 0 and 255 in an 8 bit color scheme. The file is loaded into Matlab as a matrix of these values and the porosity and average pore radius are estimated by analyzing the matrix row by row and column by column. The porosity is estimated to be $\varepsilon_{por} = 0.23$ while the average pore radius is $r_c = 26\,\mu m$. These are close to the specified values, so it is determined that the provided specifications should be used. The additional relevant parameters of the simulations are listed in Table 6.

Table 6 – LFTS simulation parameters

Parameter	Value	Unit	Parameter	Value	Unit
$\boldsymbol{\varepsilon_{por}}$	0.23		$\boldsymbol{\rho_w}$	1000	kg/m^3
$\boldsymbol{\gamma}$	0.45	N/m	$\boldsymbol{\rho_n}$	1.225	kg/m^3
$\boldsymbol{\psi}$	33	deg	**Domain**		
$\boldsymbol{r_c}$	22	μm	$\boldsymbol{x}$	25	mm
$\boldsymbol{\tau}$	1		$\boldsymbol{y}$	4	mm
$\boldsymbol{p_{c0}}$	3.43*10^6	Pa	$\boldsymbol{z}$	0.185	mm
$\boldsymbol{k_o}$	1.113	m^2	$\boldsymbol{n_x}$	31	
$\boldsymbol{\beta_c}$	0.362	N/m	$\boldsymbol{n_y}$	16	
$\boldsymbol{\mu_w}$	1.00E-03	$N-s/m^2$	$\boldsymbol{n_z}$	3	
$\boldsymbol{\mu_n}$	0.45	$N-s/m^2$	$\boldsymbol{\Delta t}$	2.50E-04	s

Both experiments were performed by applying certain volumes of water to the sample pad of the LFTS and measuring the time required for the entire length of the membrane to be wetted. A total of 7 different sample volumes were applied ranging from 80 μL to 200 μL at 20 μL intervals. Each volume was tested 3 times in order to reduce statistical hysteresis for a total of 21 data points. Only the nitrocellulose membrane was modeled, due to the porous properties of the sample and conjugate pads compared to those of the membrane. The

permeability of these pads is estimated to be 5 orders of magnitude greater than that of the membrane. Because the pore velocity is proportional to permeability, the transport across them is instantaneous relative to transport across the membrane. Therefore it is assumed that the pads can be treated as an ideal reservoir and sink with uniform saturations. The boundary conditions are updated as a function of time based upon the flux in or out of the control volume. 2D simulations of the LFTS's were run for each of the 7 volumes as well the wetting flow times are compared in Figure 23.

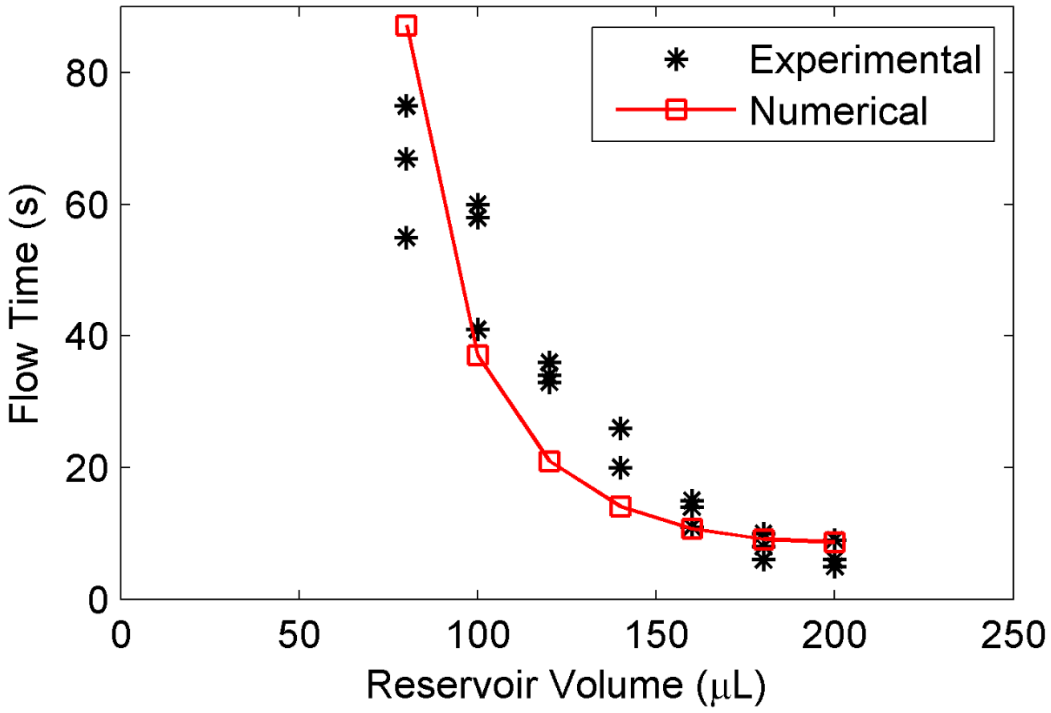

Figure 23 – Porous media model validation against LFTS experiments

The first observation that should be noted is the wide variation in experimental flow times, especially at low reservoir volumes. The Millipore official specification suggests that the variance in flow velocity is ±25%. With this in mind, the model predictions seem to be within the acceptable variance range at each volume tested. Qualitatively, the general trend of both the experimental and

simulated data appears to be exponential. Another qualitative observation that can be made is the shape of the flow front. A comparison is shown in Figure 24.

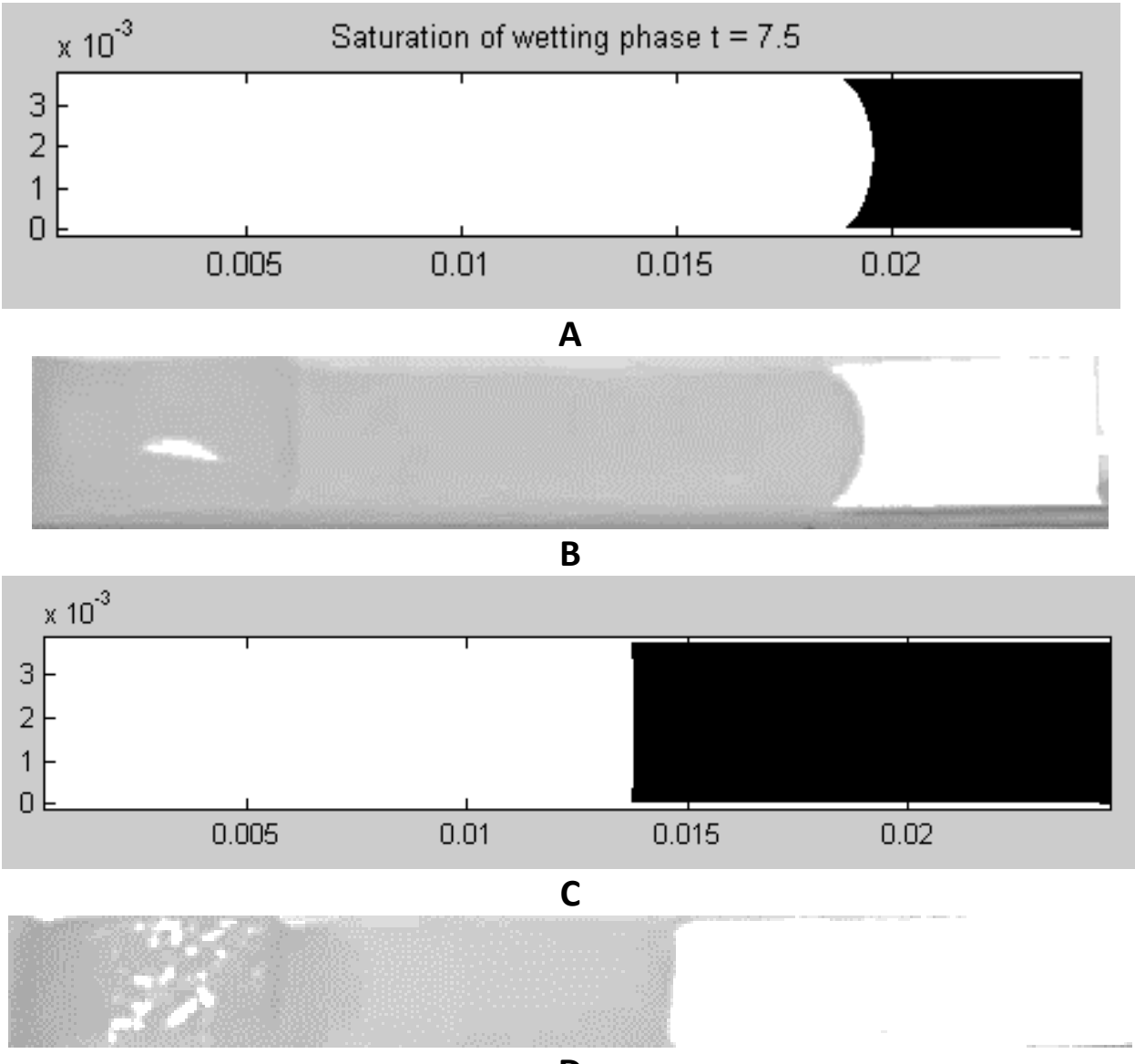

Figure 24 – LFTS flow front comparisons, A: Numerical, 200 μL reservoir, B: Experimental, 200 μL reservoir, C: Numerical, 80 μL reservoir, D: Experimental 80 μL reservoir

The flow front in both experiments (typically) and simulations has a parabolic profile that maintains a constant shape as the front moves towards the adsorption pad (Figure 24 A and B). By observation, it seemed that the parabola increased in magnitude with the reservoir volume. For low volumes, the flow front is nearly flat in both cases (Figure 24 C and D). Due to a close representation to real flow behavior, the porous media flow model is considered to be valid and relatively accurate. Additional experiments with less variability would be more desirable, however.

4.3 Summary

The total mass transport model consists of the combination of the migration within the liquid phase and the flow of the total liquid via capillary action. At each time step, the migration of sodium and sulfur within the melt are calculated in terms of molar concentrations by solving Equations (43) (44). The properties of the total liquid are updated as functions of the new concentrations. Next, the porous media flow model calculates the flux (pore velocity) and solves for the wetting phase saturation and volume fraction of liquid ($\varepsilon_{liq} = \varepsilon_{por} S_w$). The flux of individual species due to capillary motion is proportional to the normalized concentrations (C) of melt in the corresponding adjacent control volume (Equations (69) and (70)). Figure 26 in Chapter 5 illustrates flux into control volumes and the nomenclature used to represent each direction.

$$c_+(t + \Delta t) = c_+(t) + \frac{\Delta t \rho_{Na}}{M_{Na}} \left[\sum \left(\varepsilon_{liq} u_w C_+ \right)_{in} - \sum \left(\varepsilon_{liq} u_w C_+ \right)_{out} \right] \quad (69)$$

$$c_-(t+\Delta t) = c_-(t) + \frac{\Delta t \rho_S}{M_S}\left[\sum\left(\varepsilon_{liq} u_w C_-\right)_{in} - \sum\left(\varepsilon_{liq} u_w C_-\right)_{out}\right] \quad (70)$$

Where $C_+ = c_+/(c_+ + c_-)$ and $C_- = 1 - C_+$. Now the concentrations and saturations of all phases and species have been calculated for the current time step. Mass conservation can be checked by checking that the total number of moles of each species present in the system (n) equals the initial amount (n^0) (Equation (71)).

$$n_+^0 = n_+ = \sum \forall c_+$$
$$n_-^0 = n_- = \sum \forall c_- \quad (71)$$

Chapter 5: Heat Transport Modelling

5.1 Introduction

Heat transfer modelling within NaS batteries is important as temperature appears directly in the electrochemical equations and the properties and phases of the electrode materials are sensitive to temperature fluctuations. This is apparent when considering the phase diagram of sodium polysulfide (Figure 2). All of this would be still be negligible, if not for the level of heat produced during normal battery operation [29]. Because of this heating, temperature gradients form within the NaS battery. These temperature gradients can have significant effects on certain properties or even cause a pressure differential across the electrolyte due to heating of the inert gas in either electrode. This, together with increased corrosion rate and thermal stress fatigue at higher temperatures, are reasons why heat transfer within NaS cells should be considered when optimizing performance.

5.2 Theory

The general heat transport equation for a control volume is expressed as Equation (72).

$$\rho c_P \frac{\partial T}{\partial t} + \frac{1}{\forall}\left[\sum\left(\dot{m}c_p T\right)_{in} - \sum\left(\dot{m}c_p T\right)_{out}\right] = \vec{\nabla}\cdot\lambda\nabla T + \dot{q}_{total} \tag{72}$$

Where the heat generation source term ($\dot{q}_{total}$) contains any relevant heat sources. For the NaS battery this term contains the Ohmic heating ($\dot{q}_{Ohmic}$) due to ionic and electronic current flow as well as the entropy generation from the electrochemical reactions. These are written as follows:

$$\dot{q}_{total} = \dot{q}_{Ohm} + \dot{q}_{react} = J_i \Delta\phi_i + J_e \Delta\phi_e + i_F [T \frac{dE_{OCV}}{dT}] \quad (73)$$

The Ohmic heating portion can be calculated directly from the charge transport solution. The entropy generation term (dE_{OCV}/dT) on the other hand is not readily available. This term is derived from the fundamental thermodynamic relation for Gibb's free energy:

$$\Delta G = \Delta H - T\Delta S = \Delta G^0 + T\kappa \ln\left(\frac{[RED]}{[OX]}\right) = -nFE_{OCV}$$

Divide through by zF and the equation becomes:

$$\frac{\Delta H - T\Delta S}{zF} = E^0 + Tk \ln\left(\frac{[RED]}{[OX]}\right)$$

We can relate terms on the left hand side to terms on the right hand side due to the similarity of the terms. Effectively, the value $k\ln\left(\frac{[RED]}{[OX]}\right)$ is the change of Nernst potential with respect to temperature ($\frac{dE_{OCV}}{dT}$) yielding the following relations (Equations (74) and (75)).

$$\Delta H = -zF\left(E - T\frac{dE_{OCV}}{dT}\right) \quad (74)$$

$$\Delta S = zF\frac{dE_{OCV}}{dT} \quad (75)$$

Knödler [36] and Gupta et al [25] performed experiments in which he measured the values of ΔG, ΔH and ΔS for various concentrations and temperatures of NaS melt, and then used the values to calculate $\frac{dE_{OCV}}{dT}$. These values have been plotted by Min and Lee [56] with respect to depth of discharge

(Figure 25). A look up table based on the data produced by Knoedler will be used to estimate the entropy generation term in the equation.

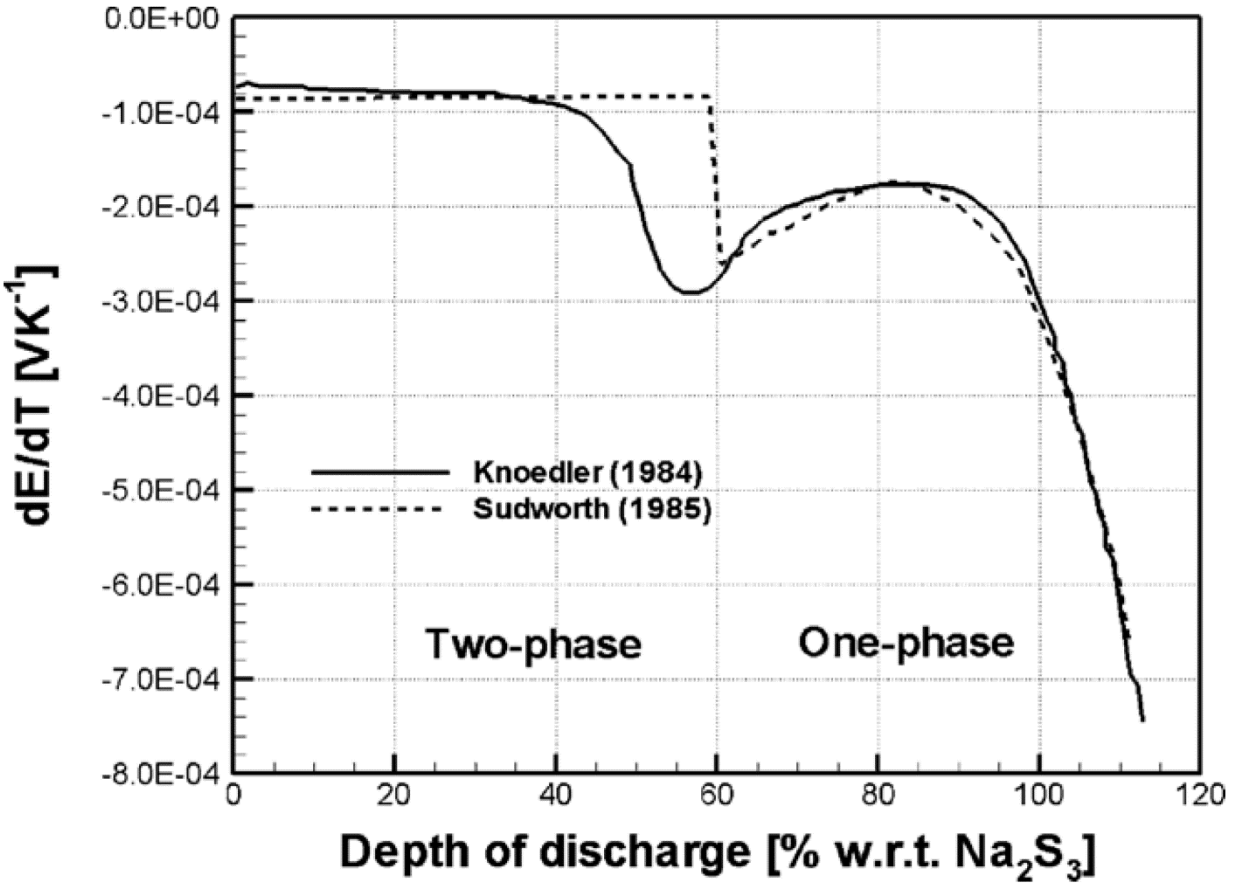

Figure 25 – Plot of dE_{OCV}/dT with respect to depth of discharge produced by Min [56] using data from Sudworth [1] and Knoedler [36]

Next the enthalpy change due to mass flow will be derived. The mass flow rates of the materials in and out of a specific control volume in the NaS cell includes ionic flux, molecular diffusion and capillary motion. The mass flow rate due to ionic flux and molecular diffusion through each interface is obtained by discretizing Equations (43) and (44) via the finite volume and multiplying by the corresponding molecular weights. If more detail is needed, please reference the discretization method described by Pakalapati [13]. A total of 6 flow rates are

produced corresponding the 6 interfaces (Figure 26) surrounding a control volume in the positive and negative direction of each coordinate (east, west, north, south, top and bottom).

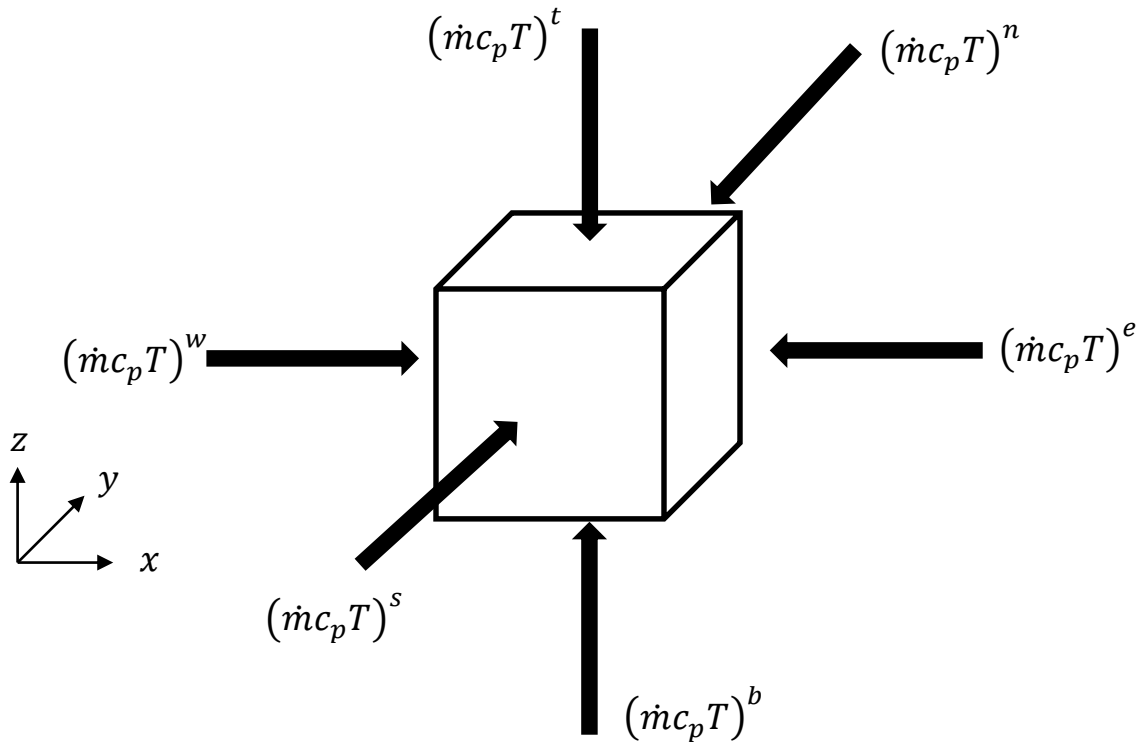

Figure 26 – Illustration of control volume fluxes

The pore velocity calculated by the porous media model is then converted to a mass flow rate by multiplying by the porosity, density and interface area. For brevity the mass flow rate through the east face ($x_P + \frac{\Delta x^e}{2}$) of a general control volume in the cathode is given as an example (Equation (76)).

$$\begin{aligned}\left(\dot{m}c_pT\right)^e = \frac{A^e}{\Delta x^e}\Bigg\{ & M_{Na}\left[\frac{t_+}{F}\sigma_i^e\left(\phi_i^E-\phi_i^P\right)\right. \\ & \left.+D\left(\varepsilon_{liq}^E c_+^E-\varepsilon_{liq}^P c_+^P\right)\right] \\ & -M_S\left[\frac{1-t_+}{2F}\sigma_i^e\left(\phi_i^E-\phi_i^P\right)\right. \\ & \left.+D\left(\varepsilon_{liq}^E c_-^E-\varepsilon_{liq}^P c_-^P\right)\right]\Bigg\}+\varepsilon_{liq}^e u_w^e \rho_w^e A^e\end{aligned} \tag{76}$$

In the anode, because only sodium is present the equation would reduce to:

$$\dot{m}^e = \frac{A^e}{\Delta x^e}\, M_{Na}\frac{1}{F}\left[\sigma_i^e\left(\phi_i^E-\phi_i^P\right)\right]+\varepsilon_{liq}^e u_w^e \rho_w^e A^e \tag{77}$$

And finally, because it is a solid, no convection occurs in the electrolyte.

Chapter 6: Numerical Implementation and Property Models

6.1 Mesh application and boundary conditions

A 3D mesh of control volumes representing the battery geometry is generated in cylindrical coordinates. The battery is represented by concentric cylinders representative of the region enclosed in the dashed box in Figure 27.

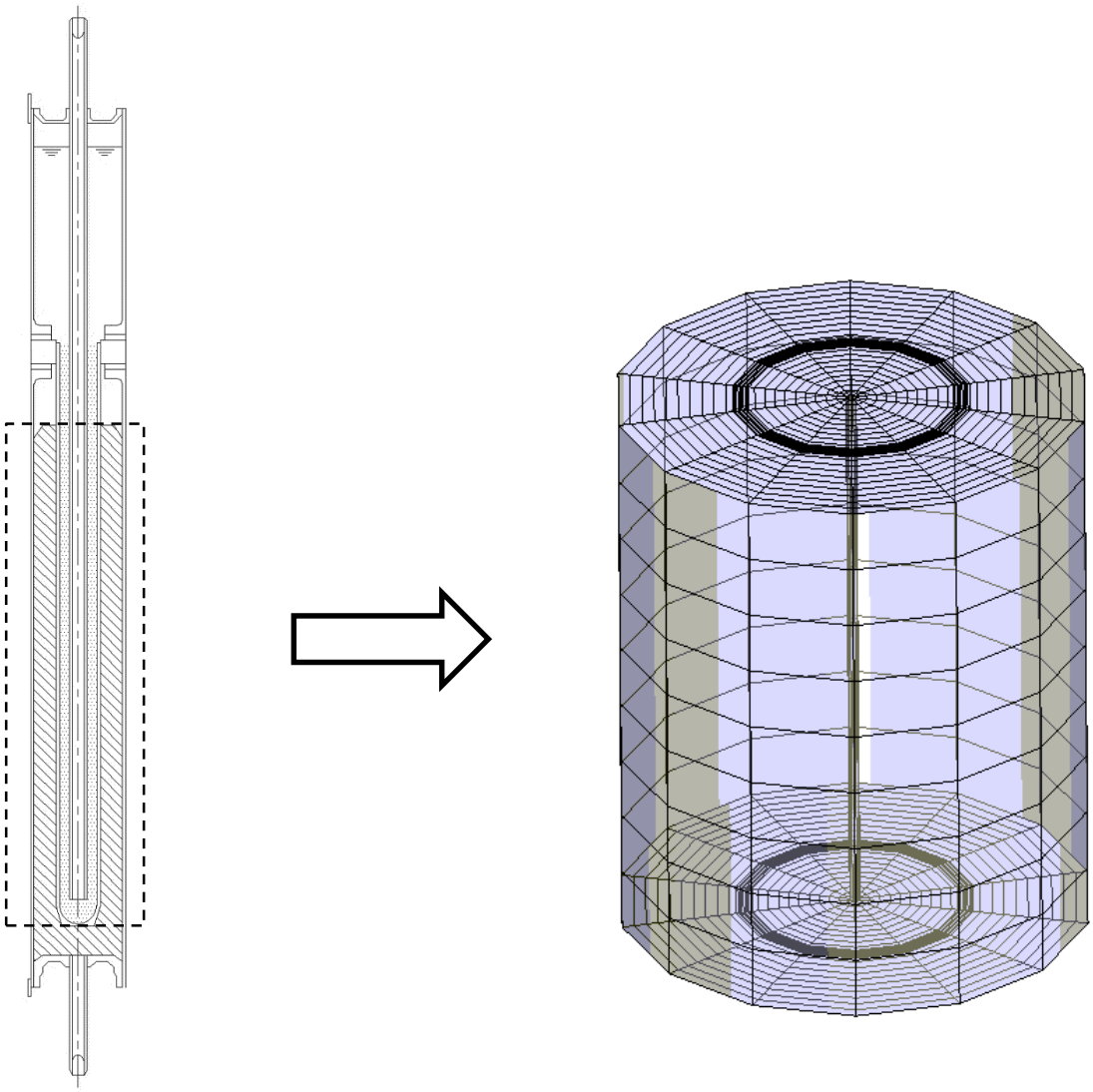

Figure 27 – NaS battery mesh illustration

Solving within this region only is more computationally efficient as no relevant electrochemistry or heat generation takes place above this region. The area below is accounted for by applying an effective length of the electrolyte to be 180 mm instead of the 171 mm actual length of electrolyte (counting only the surface area where cathode material is present). This makes the electrolyte surface area and electrode volumes nearly equivalent to the real cell. For the electrochemical model, 3 separate meshes are created to represent the anode, cathode and electrolyte. The total battery mesh (used as the electrolyte mesh) contains a superposition of volume elements from the anode and cathode meshes as well as the solid electrolyte. Ionic current is solved for in the electrolyte mesh while anode and cathode meshes act as a back ground for the electrical current to travel through. These individual continua exist simultaneously and interact via the charge transport equations. The equations are discretized and applied to the set of meshes as described by Pakalapati [13], the original developer of the code structure. Please refer to his work for a detailed description of the methods used. The system of equations and boundary conditions are summarized in Figure 28 through Figure 31.

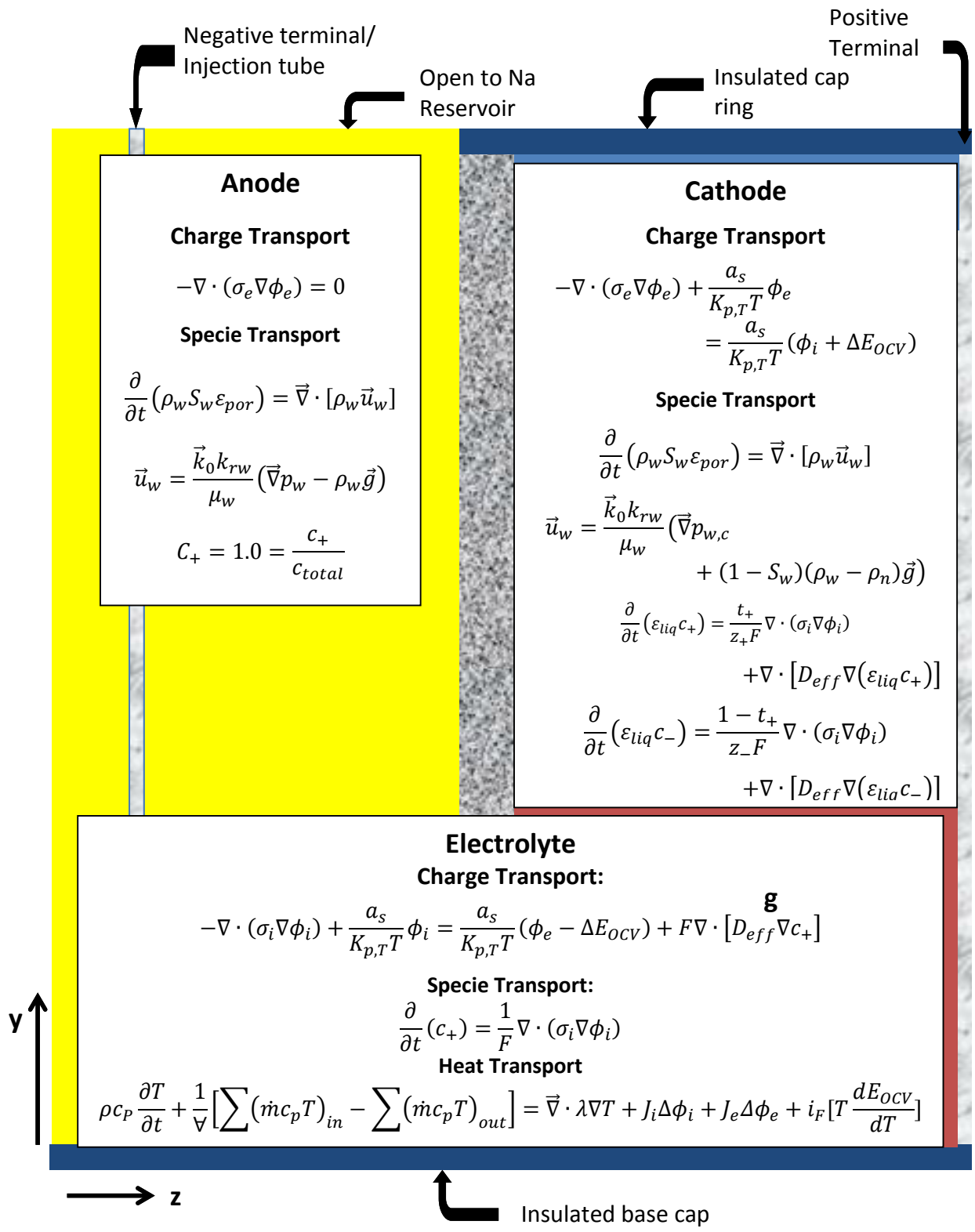

Figure 28 – Summary of model equations

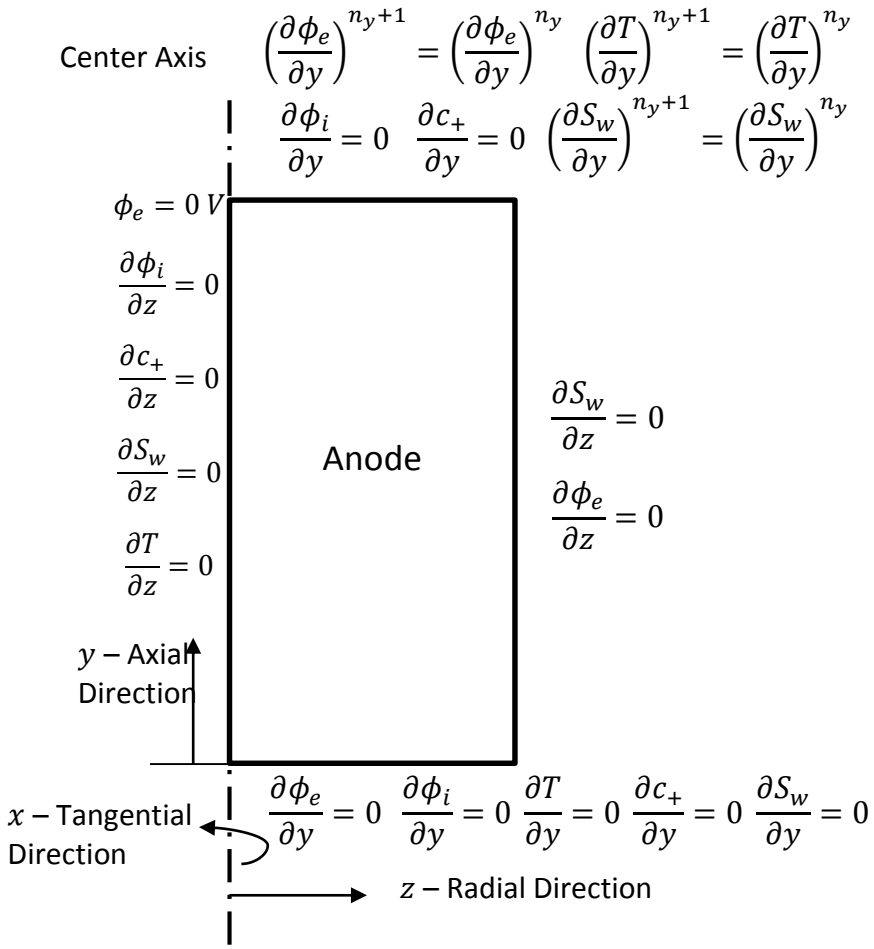

Figure 29 – Anode boundary conditions

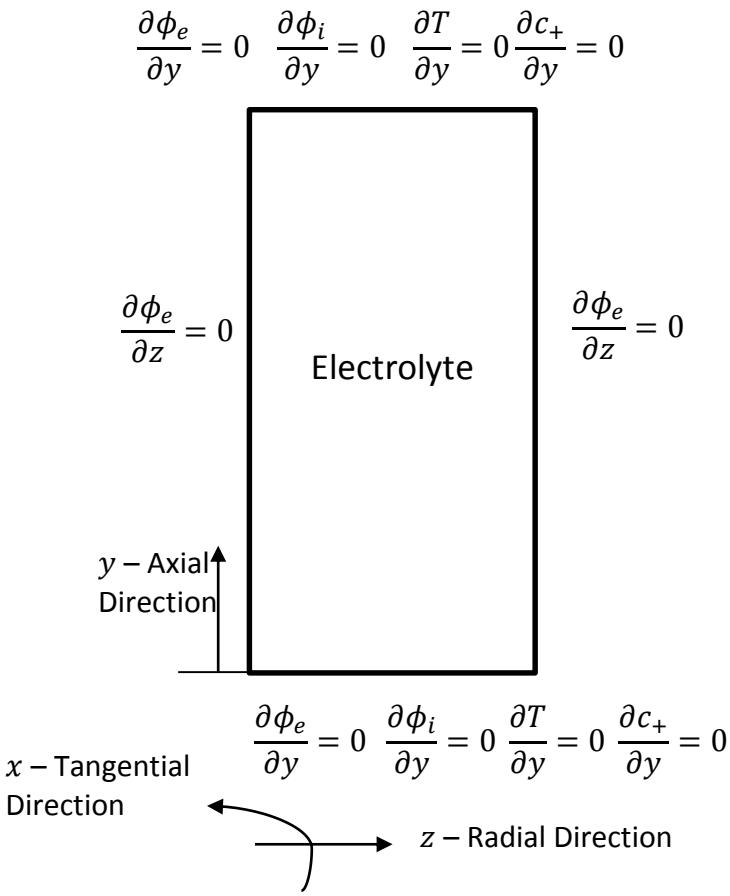

Figure 30 – Electrolyte boundary conditions

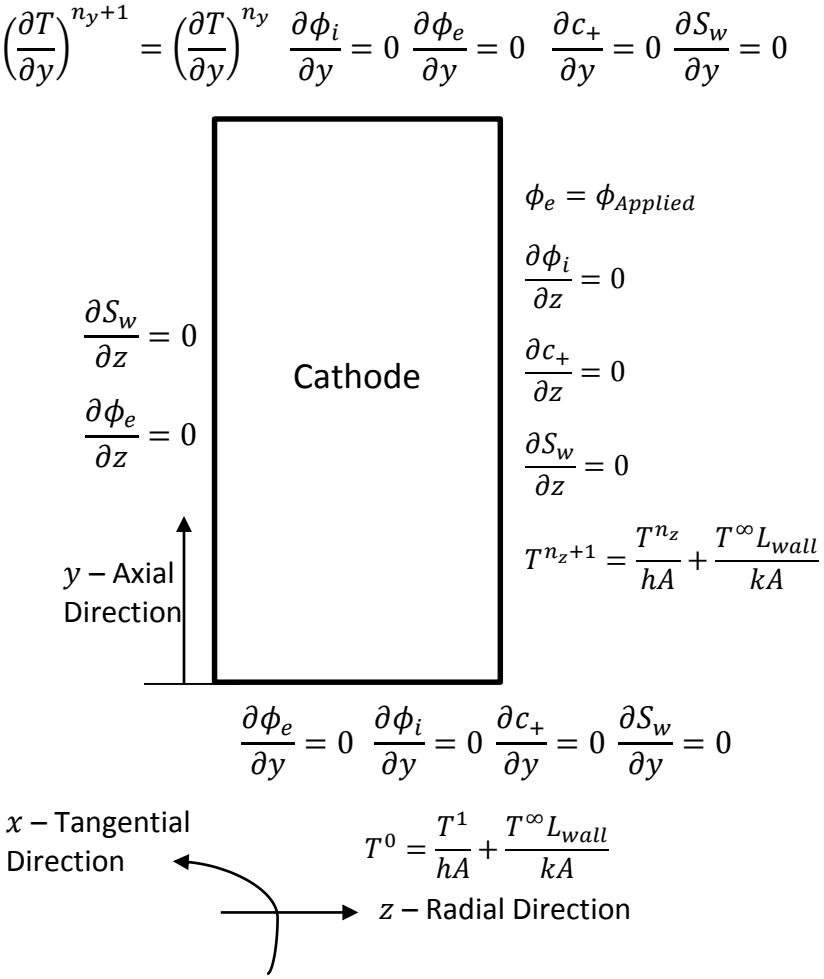

Figure 31 – Cathode boundary conditions

Periodic boundary conditions are used in the tangential direction. The central axis of the battery, which is located in the anode, is assumed to have symmetry in the radial direction, apart from the electrical potential which is set to the reference value of 0 V. At the bottom of the battery ($y = 0$), all fluxes are set to zero apart from the heat flux from the cathode, as this is the only component whose boundary is exposed to the ambient environment. In the electrodes, fluxes of liquid via capillary motion and of the electronic current are set to zero at the electrolyte surface. At the top of the domain ($y = 0.18\ m$), the anode is open to the sodium reservoir. Therefore electronic current and heat are assumed to have a constant gradient at this point. The wetting phase saturation is assumed to be equivalent to the volume of sodium remaining in the reservoir divided by the total volume of the reservoir. During discharge, once the reservoir is depleted, the flux of liquid is set to zero. No flux occurs out of the top of the electrolyte and only temperature is released from the top of the cathode. The region above the cathode mesh is filled with argon gas, which is used to calculate the properties at that boundary. At the outer radius of the cell, which is also the outer radius of the cathode, mass transport fluxes are set to zero. A wall function based on the ambient environment and properties of the cell casing is used to calculate the heat transport across this boundary. Finally, the potential is set to the cell potential, which is dependent on the desired boundary condition.

For constant voltage or voltage as a function of time, it is simply a prescribed condition. For a constant power demand or for an applied current, an initial guess for the voltage is used based on the total cell resistance. The initial value of the current I_{avg} is that of the applied current I.

$$\phi_{Applied} = I_{avg}\xi_{cell} + E_{OCV}$$

I_{avg} is then increased if the current or power output is to low or vice versa. This is done iteratively at each time step using a weighted harmonic average.

$$I_{avg} = \frac{n_1 + n_2}{n_1\left(\frac{1}{I_{avg}^{old}}\right) + n_2\left(I_{avg}^{old} * \frac{I_{applied}}{I_{actual}}\right)}$$

The applied potential is then updated by Equation for the next time step. A similar approach was applied by Pakalapati in a reduced order fuel cell model [13]. This converges to the correct applied voltage for the desired load at a rate which depends on the values of n_1 and n_2 with respect to each other. By increasing n_1, stability is increased as there is less likelihood for overshooting the correct current while increasing n_2 can speed up convergence.

6.2 Property models

Many of the properties needed to solve the transport equations are dependent on temperature or concentration. These properties are calculated for each phase at each control volume in the mesh using empirical equations. Volume averaged properties are then calculated using the volume fractions of each phase within each control volume. For a general property φ this equation for the effective value (volume average) would be:

$$\varphi^{eff} = \sum_j \varepsilon_j \varphi_j^o$$

Where j represents each phase and species. For example, within the cathode the total equation would be:

$$\varphi^{eff} = \varepsilon_S \varphi_S^o + \varepsilon_{Na} \varphi_{Na}^o + \varepsilon_{NaS} \varphi_{NaS}^o + \varepsilon_{sol} \varphi_{sol}^o + \varepsilon_{gas} \varphi_{gas}^o$$

Where $\varepsilon_S + \varepsilon_{Na} + \varepsilon_{NaS} = \varepsilon_{liq}$. Table 7 through Table 14 list in detail the values and empirical equations used for the properties of each individual phase and species. A majority of the data used in this study comes from Sudwort [1]. Table 7 lists the electrical conductivities. The beta-alumina electrolyte, sulfur and sodium polysulfide have no electrical conductivity. Sodium conductivity is sensitive to temperature variation and is therefore calculated using an equation fitted empirical data. Conductivities of the carbon and stainless steel electrode materials have relatively constant values.

Table 7 – *Electrical Conductivity (σ_e^o)* values and empirical equations [1]

Phase/Species	Equation/Value $(1/\Omega - m)$
Sodium Polysulfide	$\sigma_{e,NaS}^o = 0.0$
Sulfur	$\sigma_{e,S}^o = 0.0$
Sodium	$\sigma_{e,Na}^o = 10^8 * \left(6.37 + 2.44 * 10^{-2} * T_{^\circ C} + 2.67 * 10^{-5} * T_{^\circ C}^2 + 1.07 * 10^{-7} * T_{^\circ C}^3 - 2.67 * 10^{-10} * T_{^\circ C}^4\right)^{-1}$
Beta-Alumina	$\sigma_{e,\beta-Al}^o = 0.0$
Carbon (cathode mesh)	$\sigma_{e,sol}^o = 50.0$
Stainless Steel (anode mesh and wall)	$\sigma_{e,sol}^o = 8.33 * 10^4$
Inert gas (argon)	$\sigma_{e,gas}^o = 0.0$

The only components considered to have non-zero ionic conductivities are the sodium polysulfide and the beta-alumina (Table 8). It is noted that both sulfur conductivities are zero such that the presence of a current collector is crucial for current flow. Sodium polysulfide is calculated with an empirical equation considering both concentration (weight fraction sulfur W_S) and temperature. The beta-alumina conductivity varies depending on fabrication, so the value used by Kawamoto and Wada is used, as empirical data exists for that particular cell.

Table 8 – *Ionic Conductivity (σ_i)* values and empirical equations [1]

Phase/Species	Equation/Value $(1/\Omega - m)$
Sodium Polysulfide	$\sigma^o_{i,NaS} = 41925.9 * W_S^3 - 91093.7 * W_S^2$ $+65582.5 * W_S - 15594.4 + 0.5 * (T - 613)$ Limited by: $20.0 \leq \sigma^o_{i,NaS} \leq 101.0$
Sulfur	$\sigma^o_{i,S} = 0.0$
Sodium	$\sigma^o_{i,Na} = 0.0$
Beta-Alumina	$\sigma^o_{i,\beta-Al} = 50.0$
Carbon (cathode mesh)	$\sigma^o_{i,sol} = 0.0$
Stainless Steel (anode mesh and wall)	$\sigma^o_{i,sol} = 0.0$
Inert gas (argon)	$\sigma^o_{i,gas} = 0.0$

The material densities of all three liquid electrode materials are temperature dependent (Table 9) while the solid materials are assumed constant. Density of the inert gas is calculated using the ideal gas law. Meanwhile the heat

capacities of the materials are all assumed to be constant apart from that of the sodium, which is fitted to data in terms of temperature in Celsius (Table 10).

Table 9 – *Material Density (ρ)* values and empirical equations [1]

Phase/Species	Equation/Value (g/m^3)
Sodium Polysulfide	$\rho_{NaS}^{o} = 2.3112 * 10^6 - 660.0 * T$
Sulfur	$\rho_{S}^{o} = 2.0445 * 10^6 - 610.0 * T$
Sodium	$\rho_{Na}^{o} = 1.0189 * 10^6 - 245.0 * T$
Beta-Alumina	$\rho_{\beta-Al}^{o} = 3.76 * 10^6$
Carbon (cathode mesh)	$\rho_{sol}^{o} = 1.0 * 10^5$
Stainless Steel (anode mesh and wall)	$\rho_{sol}^{o} = 7.9 * 10^6$
Inert gas (argon)	$\rho_{gas}^{o} = PM_{Ar}/RT$

Table 10 – *Heat Capacity (c_p)* values and empirical equations [1]

Phase/Species	Equation/Value ($J/g-K$)
Sodium Polysulfide	$c_{p,NaS}^{o} = 1.31$
Sulfur	$c_{p,S}^{o} = 1.11$
Sodium	$c_{p,Na}^{o} = 1.4378 - 5.8063 * 10^{-4} * T_{^\circ C} + 4.624 * 10^{-7} * T_{^\circ C}^2$
Beta-Alumina	$c_{p,\beta-Al}^{o} = 1.2$
Carbon (cathode mesh)	$c_{p,sol}^{o} = 1.6$
Stainless Steel (anode mesh and wall)	$c_{p,sol}^{o} = 0.55$
Inert gas (argon)	$c_{p,gas}^{o} = 0.52$

As shown in Table 11, the thermal conductivities of the materials range across a number of magnitudes. In particular, stainless steel used as the cell casing and anode wick has a conductivity 5000 times that of the cathode current collector (carbon) leading one to believe that the cathode will not dissipate heat well with respect to the anode.

Table 11 – *Thermal Conductivity (λ)* values and empirical equations [1]

Phase/Species	Equation/Value ($W/m-K$)
Sodium Polysulfide	$\lambda^o_{NaS} = 0.27$
Sulfur	$\lambda^o_S = 0.0195 + 3.0 * 10^{-4} * T$
Sodium	$\lambda^o_{Na} = 105.177 - 0.049 * T$
Beta-Alumina	$\lambda^o_{\beta-Al} = 3.0$
Carbon (cathode mesh)	$\lambda^o_{sol} = 0.1$
Stainless Steel (anode mesh and wall)	$\lambda^o_{sol} = 500.0$
Inert gas (argon)	$\lambda^o_{gas} = 0.016$

For the majority of porous media properties, the values of individual phases are constant (Table 12). However, liquid sulfur is notorious for large variations in viscosity within the operating temperature range of NaS batteries so it must be accounted for. Data is not available above $317^{\circ}C$ so the resulting equation extrapolates out of its prescribed range in this study. Another important note is the discrepancy between wetting properties between the anode and cathode. The average pore radius is 100 times higher in the anode, which means permeability is 10,000 times higher. Combined with the much lower viscosity of

sodium, it is expected that the anode liquid will behave relatively ideal compared to the cathode material (homogenous phase distribution). Also note that the wetting angle of NaS is greater than 90º so at high depths of discharge, the polysulfide melt actually becomes the non-wetting fluid.

Table 12 – Relevant porous media model parameters [1] [57]

Parameter	Equation/Value	Units
Cathode Porosity	$\varepsilon_{por} = 0.9$	
Anode Porosity	$\varepsilon_{por} = 0.9$	
Cathode pore radius	$r_c = 4.0 * 10^{-8}$	m
Anode pore radius	$r_c = 4.0 * 10^{-6}$	m
Surface tension Sulfur	$\gamma_S^o = 0.0614$	N/m
Surface tension Sodium	$\gamma_{Na}^o = 0.18$	N/m
Surface tension NaS	$\gamma_{NaS}^o = 0.12$	N/m
Wetting angle Sulfur	$\psi_S^o = 50^\circ$	
Wetting angle Sodium	$\psi_{Na}^o = 89^\circ$	
Wetting angle NaS	$\psi_{NaS}^o = 100^\circ$	
Viscosity Sulfur	$\mu_S^o = 931.25 - 3.148 * T + 0.00266 * T^2$	$\frac{N-s}{m^2}$
Viscosity Sodium	$\mu_{Na}^o = 3.0 * 10^{-4}$	$\frac{N-s}{m^2}$
Viscosity NaS	$\mu_{NaS}^o = 0.025$	$\frac{N-s}{m^2}$
Tortuosity (Throughout)	$\tau = 1.5$	
Permeability (isotropic)	$k_o = r_c^2 \varepsilon_{por}/\tau$	m^2
Capillary Pressure	$p_{c,o} = 2\gamma^{eff} \cos(\psi^{eff}) / r_c$	Pa

The polarization resistance (which is inversely proportional to the exchange current density) is not well defined in the literature. For the cathode, Kawamoto and Wada [8] [9] [10] [33] use the listed value and produced results very similar to experiments. The corresponding parameter in the anode is not known and has been calibrated such that the voltage curve of a constant current cell cycle is matched closely. The result is an anodic polarization resistance much lower than the cathodic counterpart. In other words, the kinetics are much faster at the anode/electrolyte interface than at the cathode/electrolyte interface. This is plausible as it is expected that the cathode will determine most of the electrochemistry based on the literature review. The diffusion coefficient is calculated in two parts. First the binary diffusion coefficient between sodium and sulfur is calculated using an empirical function produced by Thompson [58]. This is combined with the analytical equation for ionic diffusion which follows the theory presented by Newman [39]. The transference number is calculated using a semi-theoretical equation. The constants in the equation are related to the formal potential of the cell reaction. The convection heat transfer coefficient is calculated using a formula presented by Bejan [59] for natural convection around a vertically oriented cylinder.

Table 13 – Diffusion and Miscellaneous Electrochemical Properties

Parameter	Value/Equation	Units
Polarization Resistance in Cathode [10]	$K_P = 1.0 * 10^{-4}$	$\Omega - m^2$
Temperature Dependent K_P in Cathode	$K_{P,T} = 1.658 * 10^{-7}$	$\frac{\Omega - m^2}{K}$
Polarization Resistance in Anode (Calibrated)	$K_P = 3.3 * 10^{-6}$	$\Omega - m^2$
Temperature Dependent K_P in Anode (Calibrated)	$K_{P,T} = 5.4 * 10^{-9}$	$\frac{\Omega - m^2}{K}$
Area Density [10]	$a_S^{eff} = \varepsilon_{liq} a_S^o$ $a_S^o = 100$	$\frac{cm^2}{cm^3}$
Transference Number [40]	$t_+ = \frac{\frac{3.078 * 10^{-3} T + 4.7215 * 10^{-2}}{7.35 * 10^{-4} T - 1.56} - \frac{2}{X}}{1 - \frac{2}{X}}$	
Effective Diffusion [10] [39]	$D_{eff} = \frac{1}{3} D_o \frac{\left(2 + \frac{1}{X}\right) t_+ - \frac{1}{X}}{t_+ (1 - t_+)}$	m^2/s
Diffusion Coefficient [58]	$D_o = 3.89 * 10^{-4} e^{-\frac{1907.4}{T}}$	m^2/s
Convection Heat Transfer Coefficient at wall [59]	$h_{conv} = 5.79$	$\frac{W}{m^2 K}$

Table 14 outlines the domain, mesh and time step used for the majority of this study. Notice that the total number of nodes in the anode, cathode and solid electrolyte in the radial direction are greater than the number of nodes in the total mesh (25 compared to 21). This is due to the use of “ghost cells” just outside

the boundaries of each domain. These ghost cells are used to apply boundary conditions across an interface, specifically the Neumann boundary conditions of a constant (or zero) derivative. Another important distinction is between the time steps used to solve the implicit and explicit equations. The charge and heat transfer equations are solved implicitly while the mass transport models are solved explicitly. When marching forward in time, the mass transport models are advanced by $\Delta t_{imp}/\Delta t_{exp}$ steps each time the electrochemistry and heat transfer move forward once. Even at this increased number of time steps, observations of the model show that the charge transport equations account for the majority of computational costs.

Table 14 – Domain and mesh size

	Grid Size	Dimension
Radial direction (z):		
Total	$n_z = 21$	$15\ mm$
Anode	$n_{z,a} = 8$	$6.375\ mm$
Solid electrolyte	$n_{z,elec} = 5$	$1.125\ mm$
Cathode	$n_{z,c} = 12$	$7.5\ mm$
Axial direction (y)	$n_y = 22$	$180\ mm$
Tangential direction (x)	$n_x = 10$	2π
Time step (implicit)	$\Delta t_{imp} = 0.1\ s$	
Time step (explicit)	$\Delta t_{exp} = 1.0 * 10^{-3}\ s$	

Chapter 7: Results and Discussion

The charge, mass and heat transport models are compared to the experimental and numerical results produced by Kawamoto and Wada [8] [9] [10] [29] [33]. These include cell voltage curves for multiple applied currents, cell temperature measurements and the distribution of the current density in the vertical direction. All of these measurements and simulations were performed on the battery shown in Figure 6 using the parameters and equations described in the previous chapters.

7.1 Electrochemistry Model

The calculated cell voltage is compared to measured cell voltage data as a function of depth of discharge (Figure 32). In both cases the numerical data agrees with the experimental data. Figure 33 demonstrates the effect that porous media has on the voltage curve. As shown, high potential occurs at the beginning of the first charging cycle. It seems that with the cathode melt condensed at the bottom in a fully saturated region, ionic migration is limited. It is assumed to be due to the fact that the liquids are incompressible and there is a lack of free pore space for ions to be transported through. Also note that the total capacitance increases slightly from one cycle to the next (on the order of 1.5% from the 1^{st} to 10^{th} cycles). Additionally, the cell resistance is plotted as a function of depth of discharge and divided into individual components in order to illustrate the overall contribution of each in Figure 34. It is observed that the contribution of the anode is nearly insignificant compared to that of the electrolyte and cathode. Also, the electrolyte and ohmic resistance of the cathode are nearly constant (with the cathode ohmic resistance increasing slightly as depth of discharge decreases). The

most interesting component is the remaining loss that includes polarization and concentration losses. There are two primary factors which contribute to this loss, the effective surface area (a_{eff}) between the electrodes and electrolyte and the relative total concentrations of sulfur and sodium in the cathode. Polarization resistance increases as the effective surface area is depleted (see Equation (34)), which is most extreme at high depths of discharge when sodium is depleted to low levels in the anode (Figure 38). At low depths of discharge, the loss depends on the direction of current (charging or discharging). During charge, concentration losses increase as sodium concentration in the cathode is depleted. However, during discharge this loss is dependent on available sulfur instead which is why there is an immediate drop of $10\ m\Omega$ cell resistance when the current direction is switched.

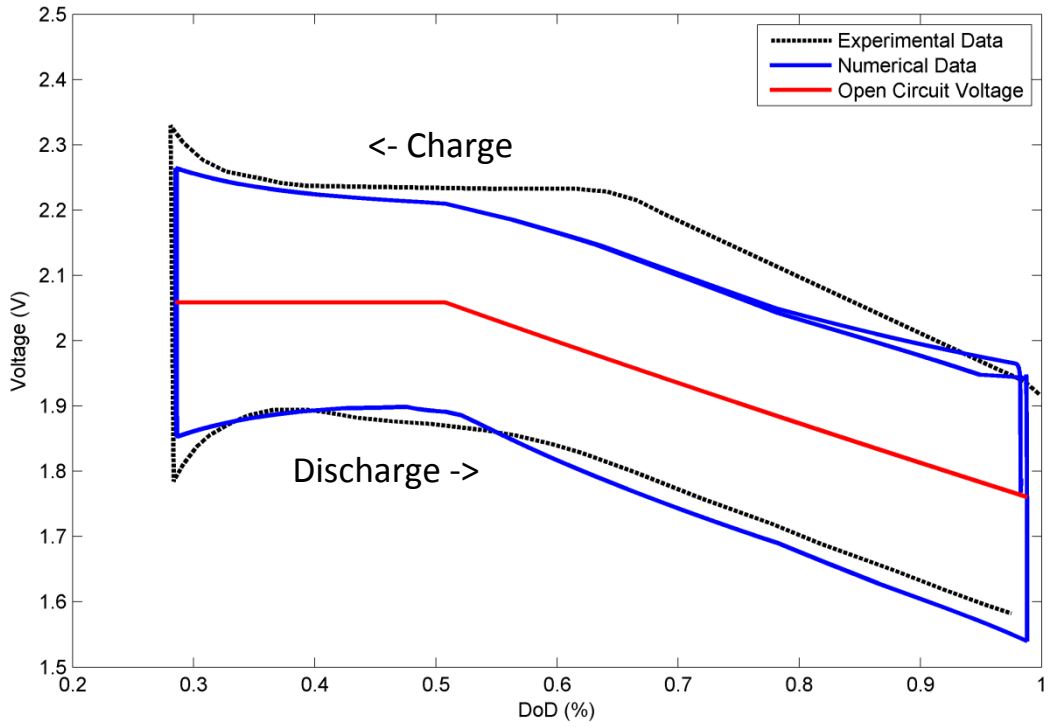

Figure 32 – Electrochemistry validation – 9 Amp total current charge and discharge curve with respect to DoD.

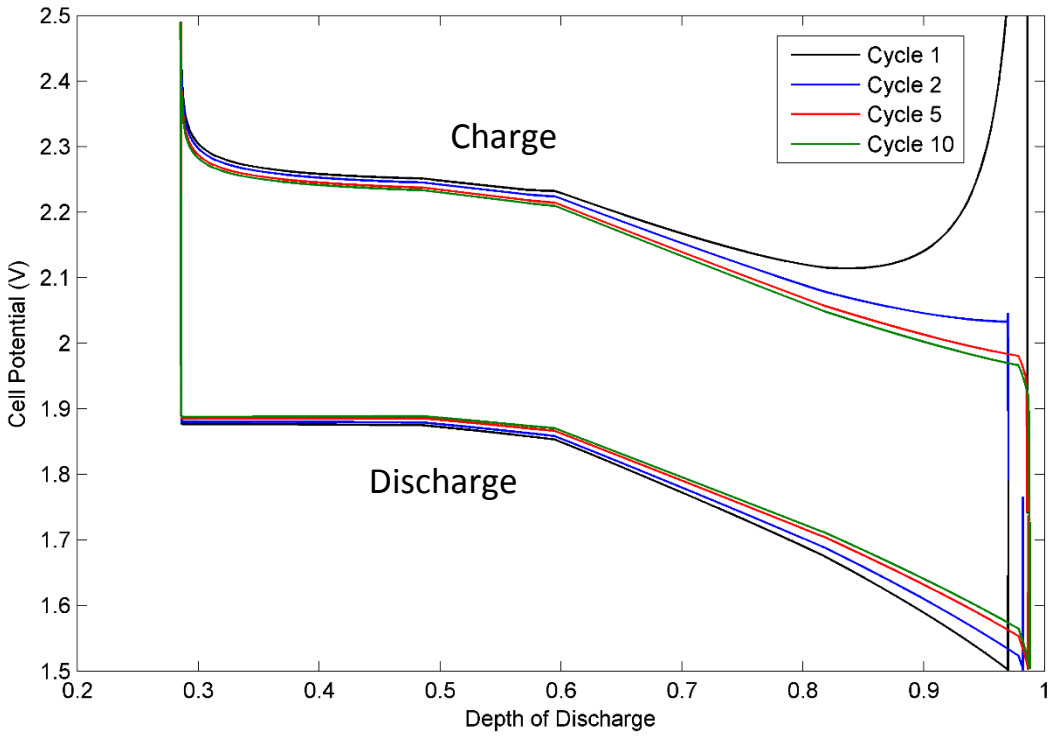

Figure 33 – Demonstrations of cycling hysteresis due to porous media effects

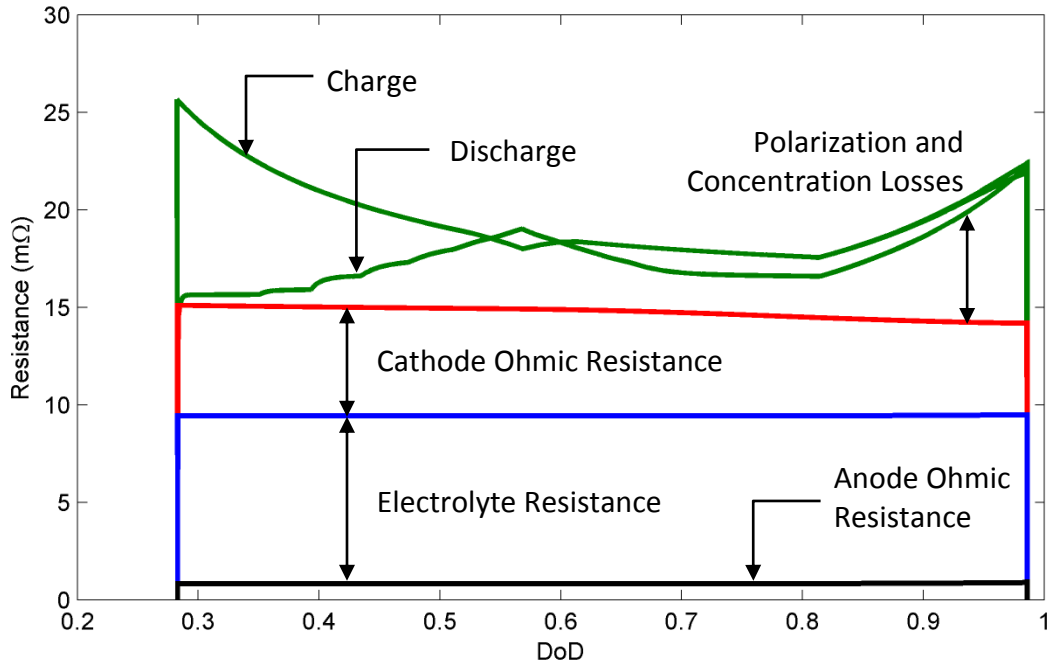

Figure 34 - Cell resistance and individual losses during charge/discharge at 9 amps

7.2 Heat Transfer Model

Averaged temperature data is compared to empirical and numerical data produced by Kawamoto and Kusakabe [29].The average applied current density is set to mA/cm^2 (10.01 A total for this cell). Figure 35 shows the results from the model developed in this study compared to data from reference [29]. In both cases the wall temperature is relatively constant at the wall. The battery is cooled overall during charge due to the backwards reaction being endothermic. Heating occurs during discharge, with the present model predicting a peak temperature to occur near the beginning while Kawamoto's model predicts a peak midway through.

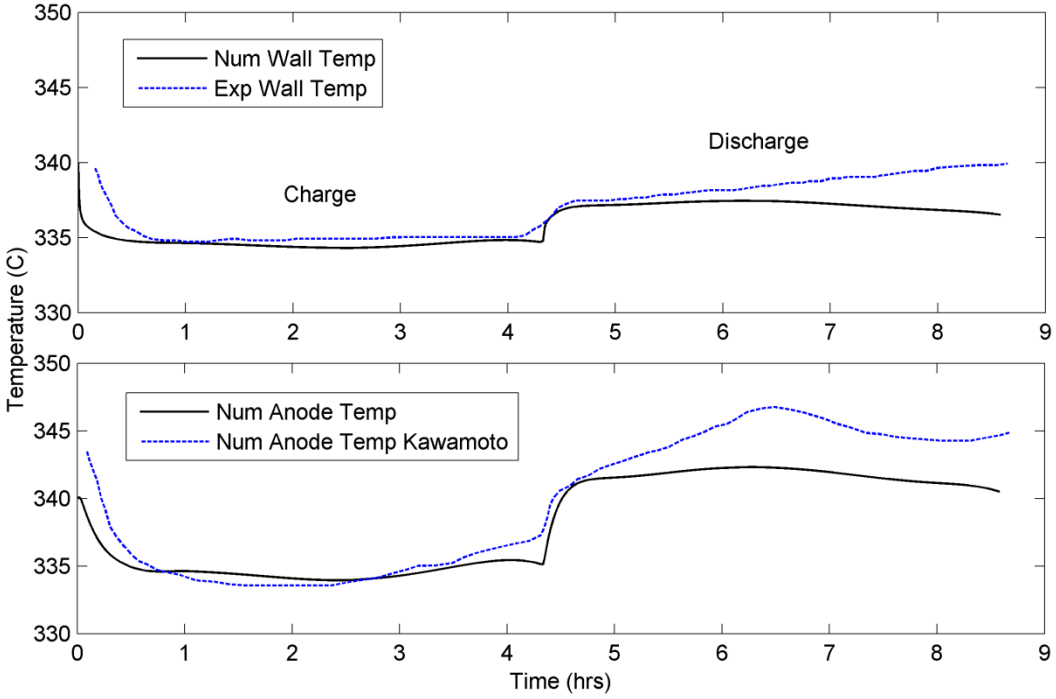

Figure 35 – Numerical temperature data compared to experimental and numerical results by Kawamoto [29]

The effect that the porous media has on the temperature gradient is also studied. An example is shown in Figure 36. Capillary rise has a significant effect on the temperature distribution, especially considering the low thermal conductivity of the cathode materials (Table 11). When gravity is assumed dominant (capillary pressure neglected) the highest temperatures occurs in the region above the cathode liquid with temperature overall distributed vertically. This may be ideal in practice as the similar temperatures in the anode and cathode would prevent gas pressure from building up in one electrode, causing an amplified pressure gradient to occur across the electrolyte. If this pressure exceeds the yield strength of the electrolyte, the electrolyte may rupture. Direct contact between electrodes would result in near instantaneous reactions, rapid heating and possible

explosion. When capillary action is considered, this same region where liquid would now be present is actually cooler overall than any other part of the cell. The primary temperature gradient is swapped from vertically to radially, which could result in failure as mentioned previously. To study this in more detail, the total pressure difference across the electrolyte is calculated within the model and compared to the max pressure that the electrolyte can withstand. The conservative estimate for the fracture strength (yield strength) of beta alumina according to Sudworth [1] is $\sigma_F = 230\ MPa$. For a circular vessel, the limiting pressure is calculated as:

$$P_{limit} = \frac{2 * (r_o - r_i) * \sigma_F}{r_o} = \frac{0.001125\ m * 230\ MPa}{0.015\ m} \approx 69 MPa$$

For the case with a high current density of $390 \frac{mA}{cm^2}$, it is found that the maximum pressure difference occurs at the end of discharge. This is as expected as this is when the ratios of liquid volume between electrodes is the highest (most of the sodium has migrated to cathode) and when the highest temperatures occur. Assuming the worst case scenario, in which the cell is constructed at room temperature and atmospheric pressure such that it contains a large amount of inert gas (Argon), the maximum pressure difference calculated is 0.43 MPa. It is therefore determined that for the cell being studied, failure due to electrolyte fracture is improbable assuming no major defects exist.

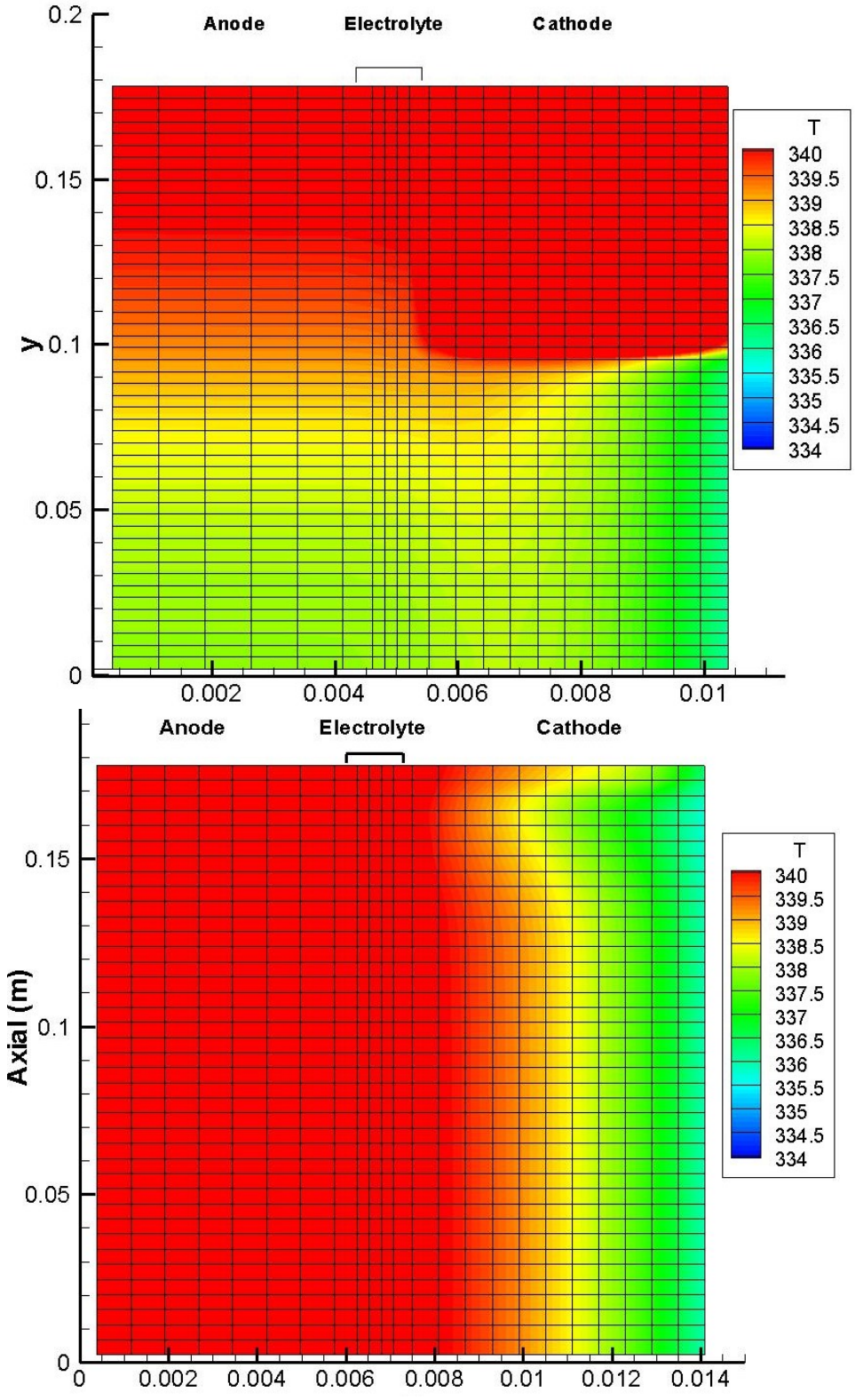

A. Zero capillary pressure

B. Porous media model considered

Figure 36 – Temperature gradients during discharge: A. without capillary pressure and B. with capillary pressure

7.3 Porous media

The effects of the porous media model on vertical current density distribution are compared to experimental measurements in the axial (vertical) direction. This data was produced by Kawamoto and Wada [8]. As shown, both the numerical and empirical values of current density decrease as moving vertically. The gradient appears to be sharper in the numerical case. However, the data may not be sufficient for revealing any sharp gradients.

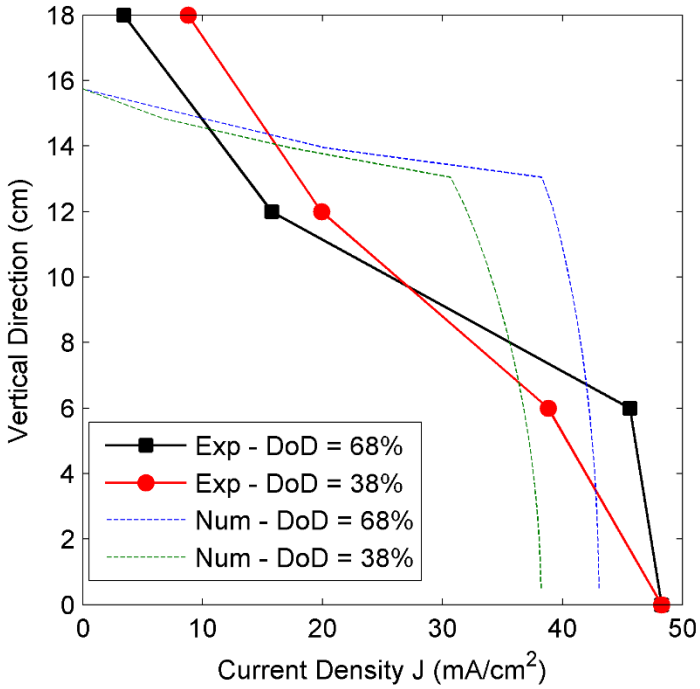

Figure 37 – Porous media validation – Current density gradients in vertical direction compared to empirical data from [8]

The model produces gradients of liquid volume fractions in the cell with results shown in (Figure 38).

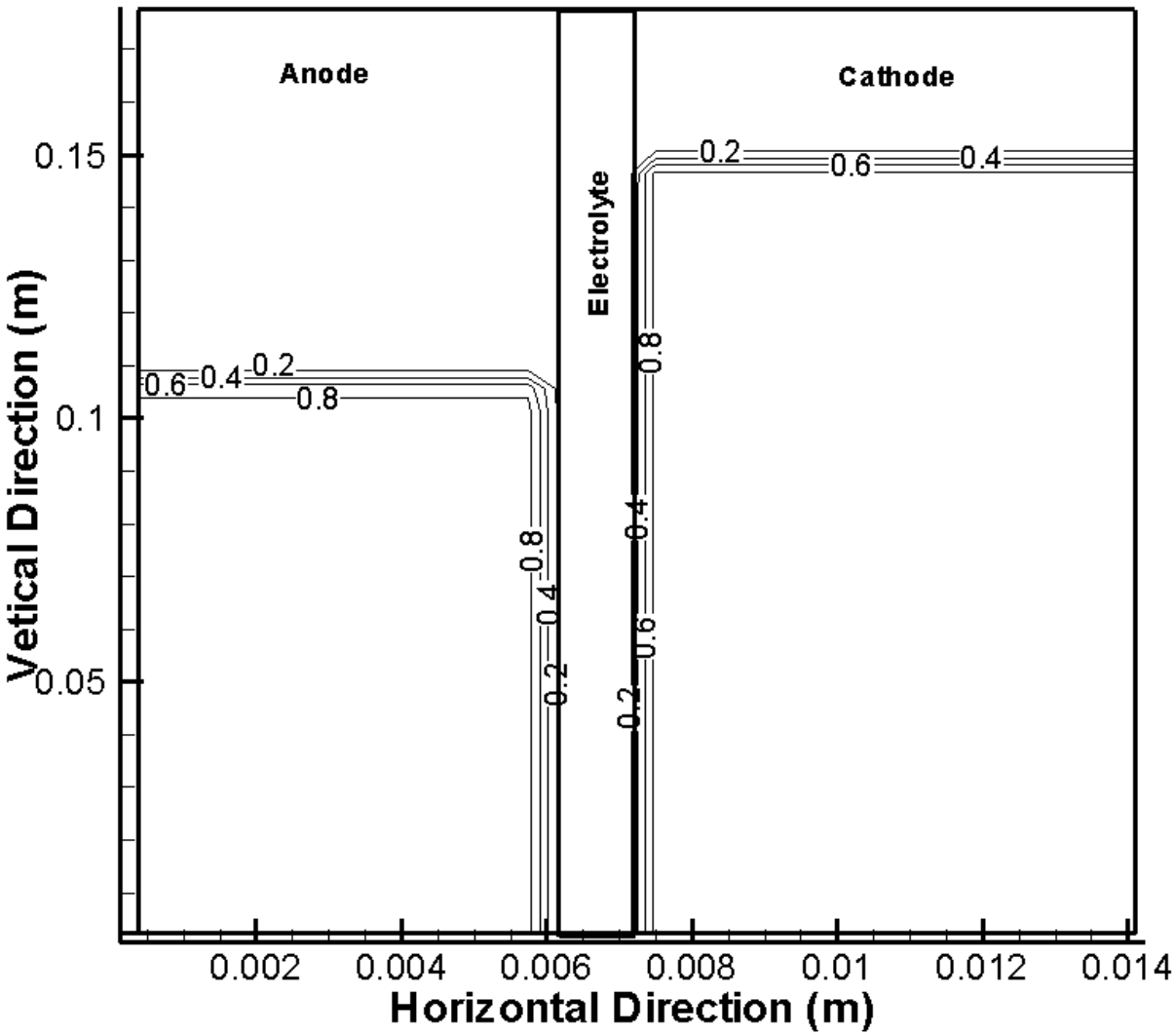

Figure 38 A. Before charge (1st cycle)

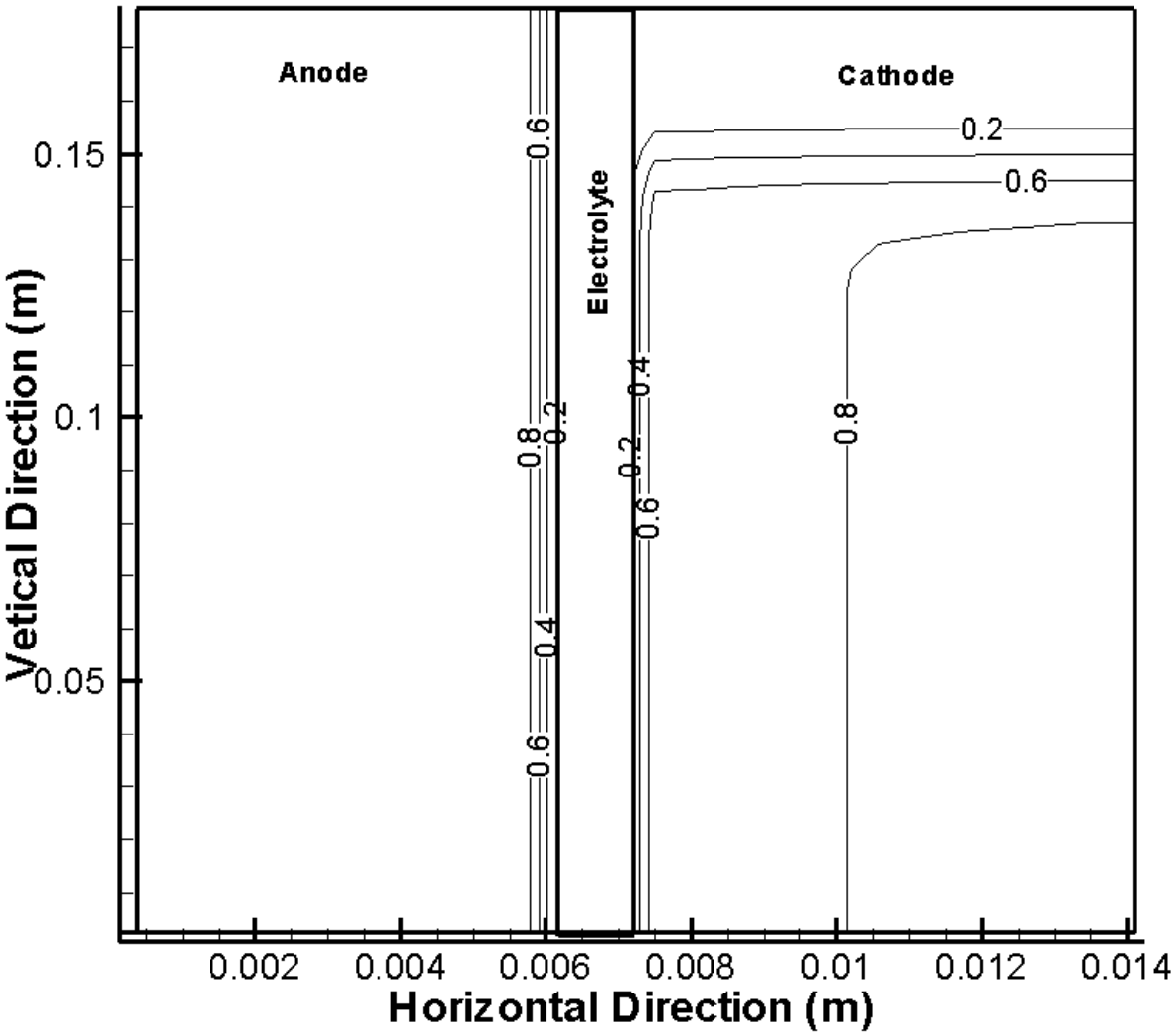

Figure 38 B. 2 hours into charge (1st cycle)

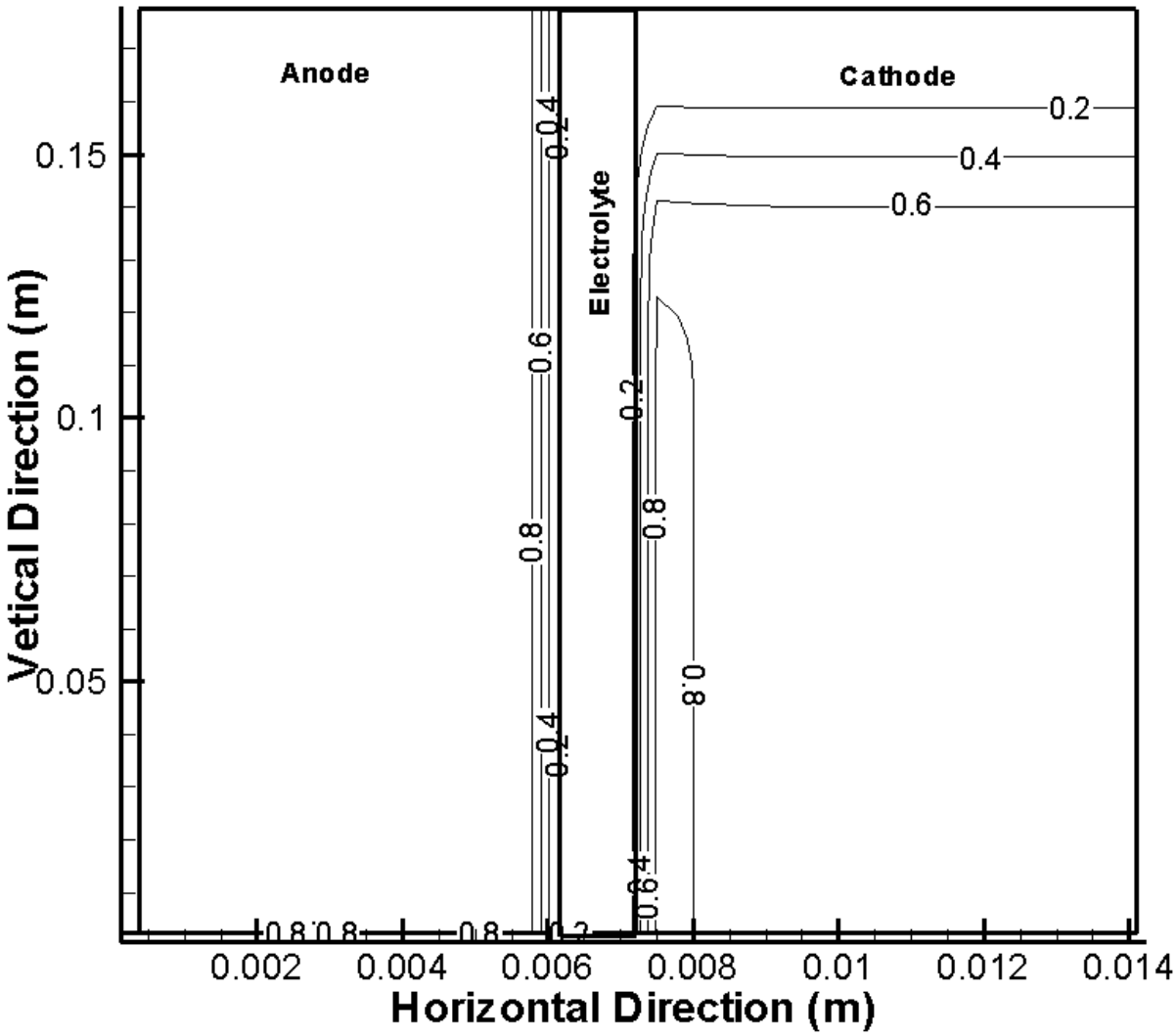

Figure 38 C. 2 hours into discharge (1st cycle)

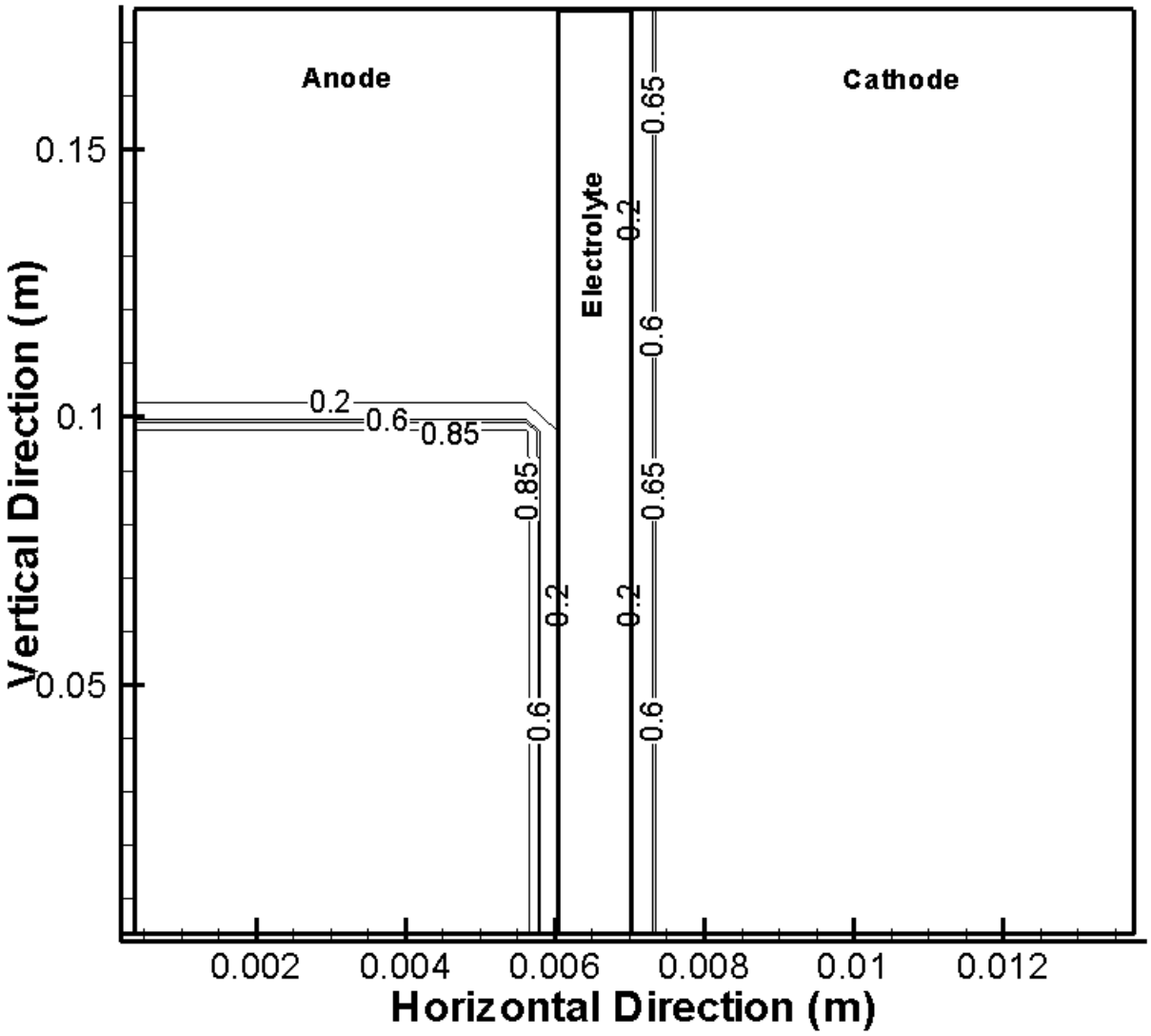

Figure 38 D. Before charge (5th cycle)

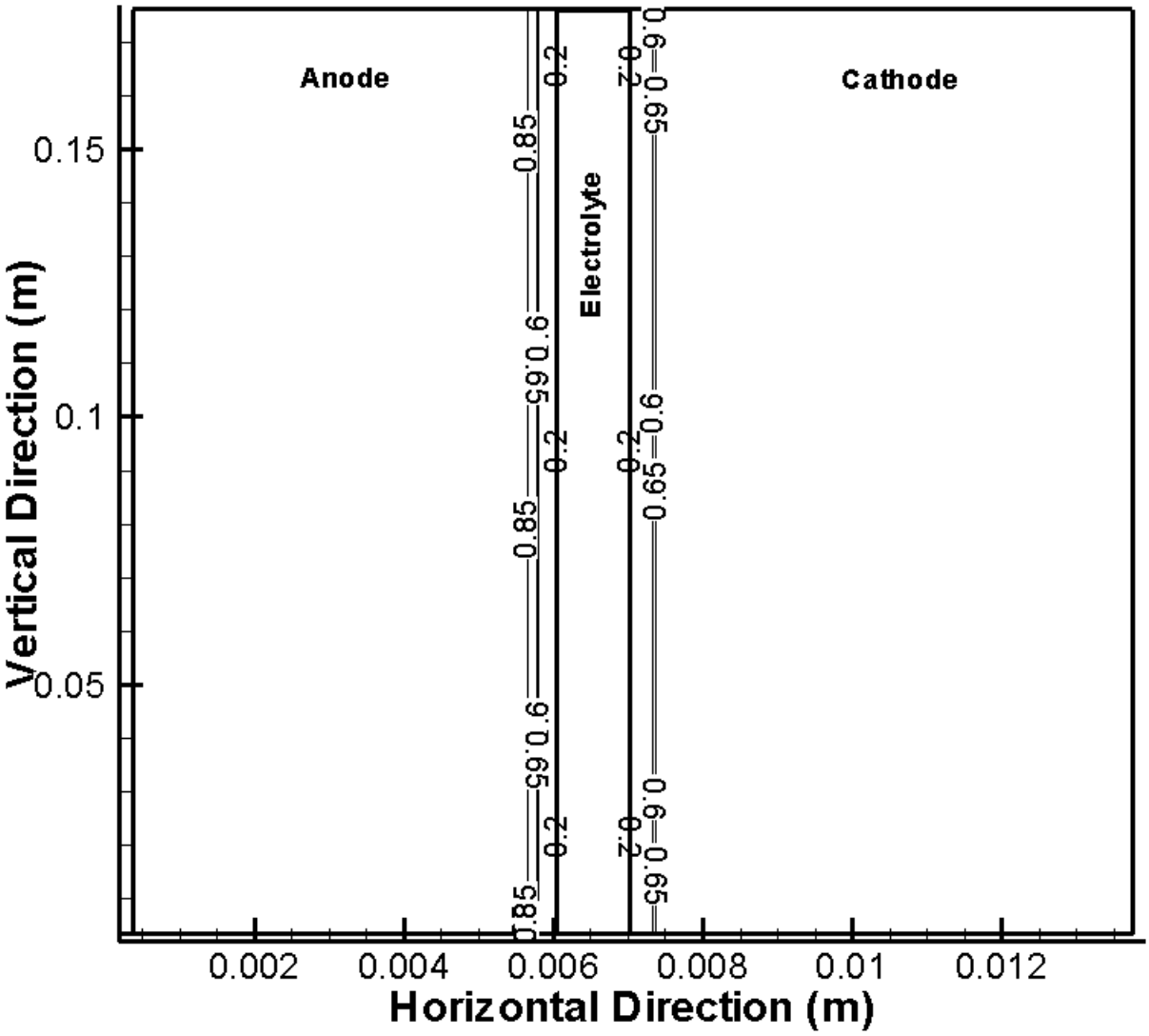

Figure 38 E. 2 hours into charge (5th cycle)

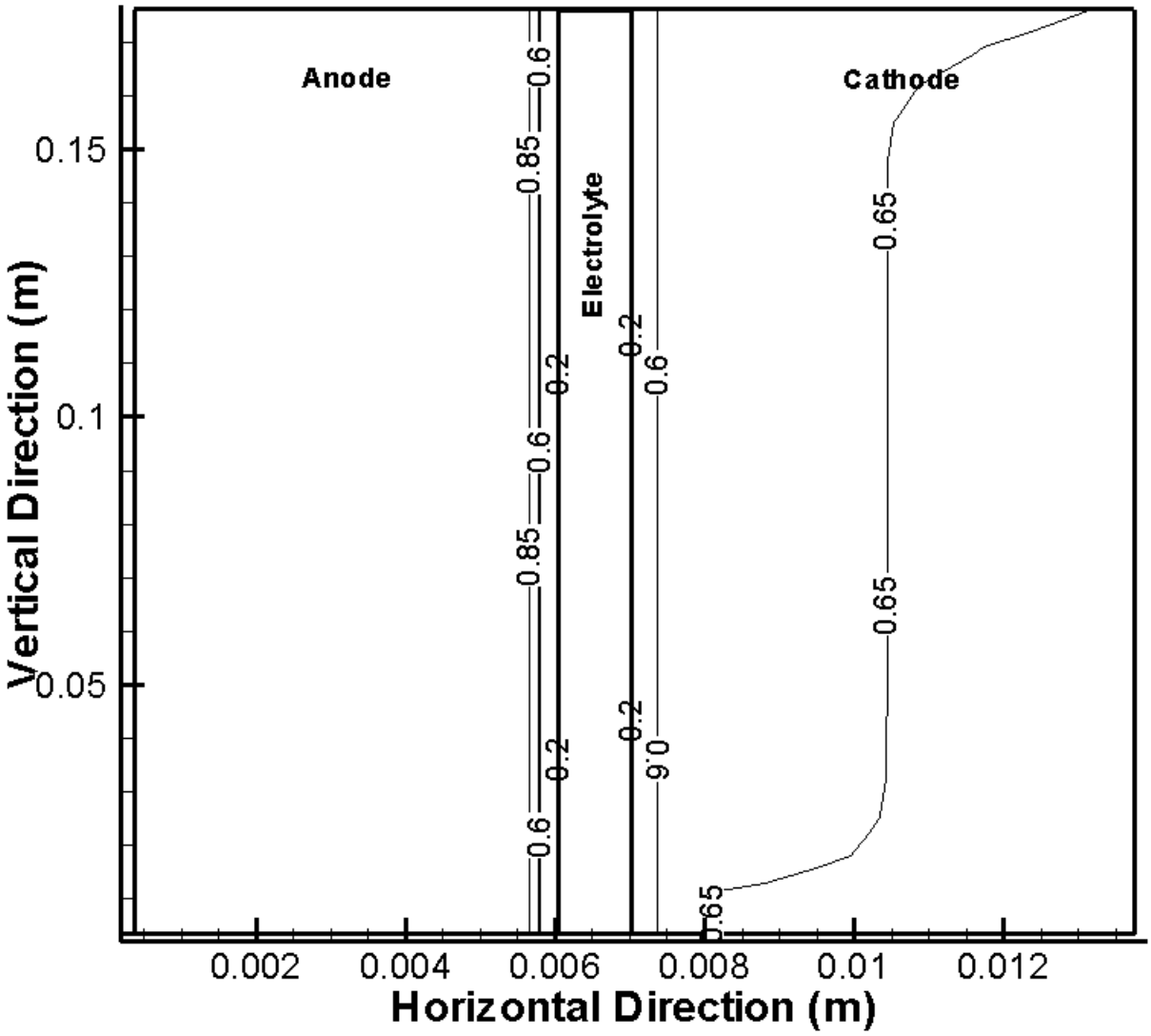

Figure 38 F. 2 hours into discharge (5th cycle)

Figure 38 – Demonstration of liquid saturation gradients during battery cycling with an applied current density of $130\ mA/cm^2$

Notice that no gradient develops within the anode but rather a sharp interface between liquid and gas. This is due to the force of gravity and buoyancy being dominant over capillary pressure. In the cathode, liquid is depleted near the electrolyte surface during charge and accumulated during discharge (Figure 38 A through C). This is caused by the sodium species being carried out of and into the

cathode respectively at the electrolyte surface. However, after multiple cycles, the capillary pressure (which is approximately 10 times higher than pressure gradient produced by gravity for the given properties) dominates and results in the liquid being almost uniform in the vertical direction (Figure 38 D through F). Additionally, during charge there is a “dewetting” (decrease in wetting phase saturation) at the electrolyte surface which would suggest a decrease in effective surface area and an increase in polarization loss and electrolyte resistance (as is shown in Figure 34).

It seems illogical that liquid would travel vertically and displace gas, however it has been shown to occur using a simple experiment:

A 2.6 cm square, 1.5 cm deep polystyrene container (10 mL volume) is tightly packed with carbon felt (similar to that used in the sulfur electrode) and an 18 gauge needle is inserted near the bottom of one side (Figure 39). The openings are then sealed with high pressure marine grade sealant in order to prevent leakage. 8 mL of canola oil (80% of container volume) is then injected via a syringe at a rate of approximately 0.15 mL/s and then allowed to reach a steady state. The final results are shown in Figure 39 and Figure 40. It is observed that the oil has spread at a similar rate both vertically (against gravity) and horizontally. Air bubbles and fingering of the oil/air interface are shown. Additionally, air is present at the container walls as oil preferentially wets the carbon, dewetting the polystyrene which creates a vacuum that is filled by air.

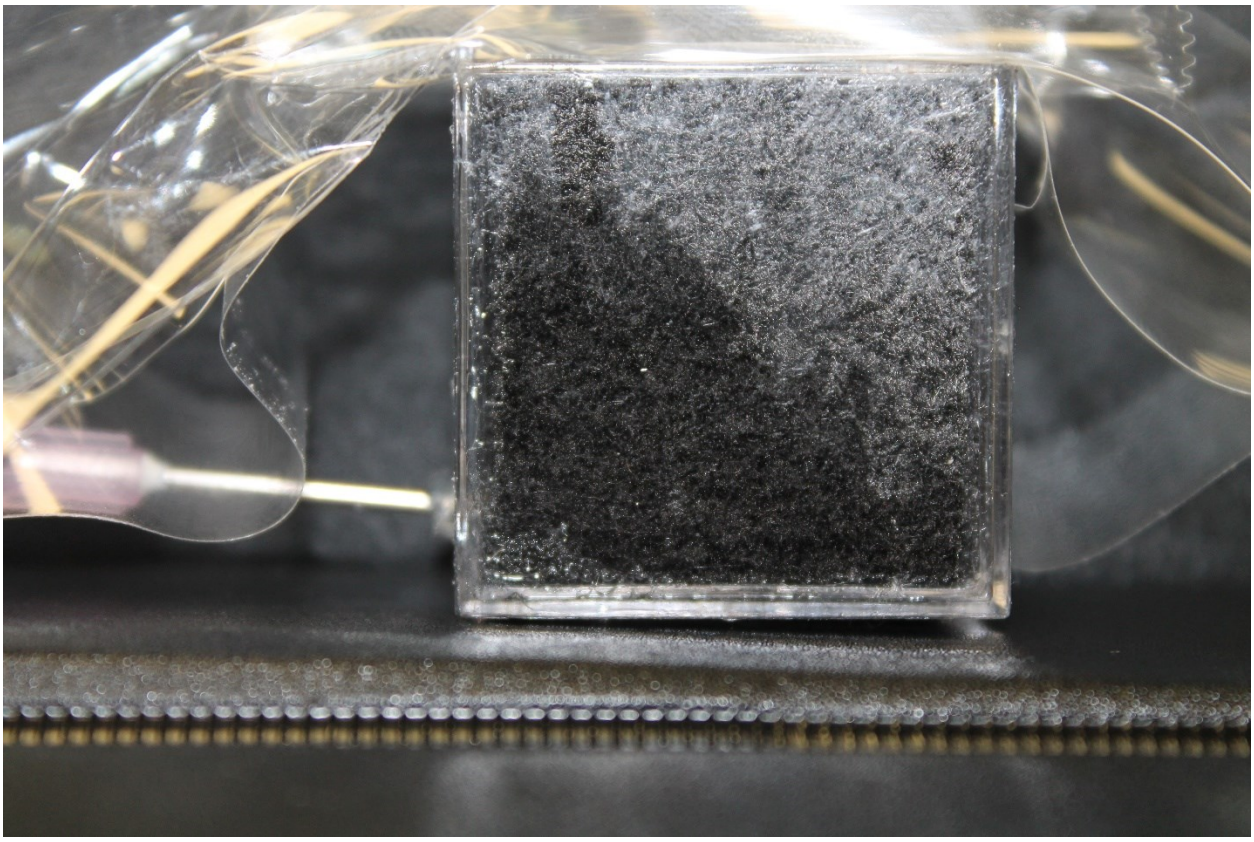

Figure 39 - Porous media experimental setup

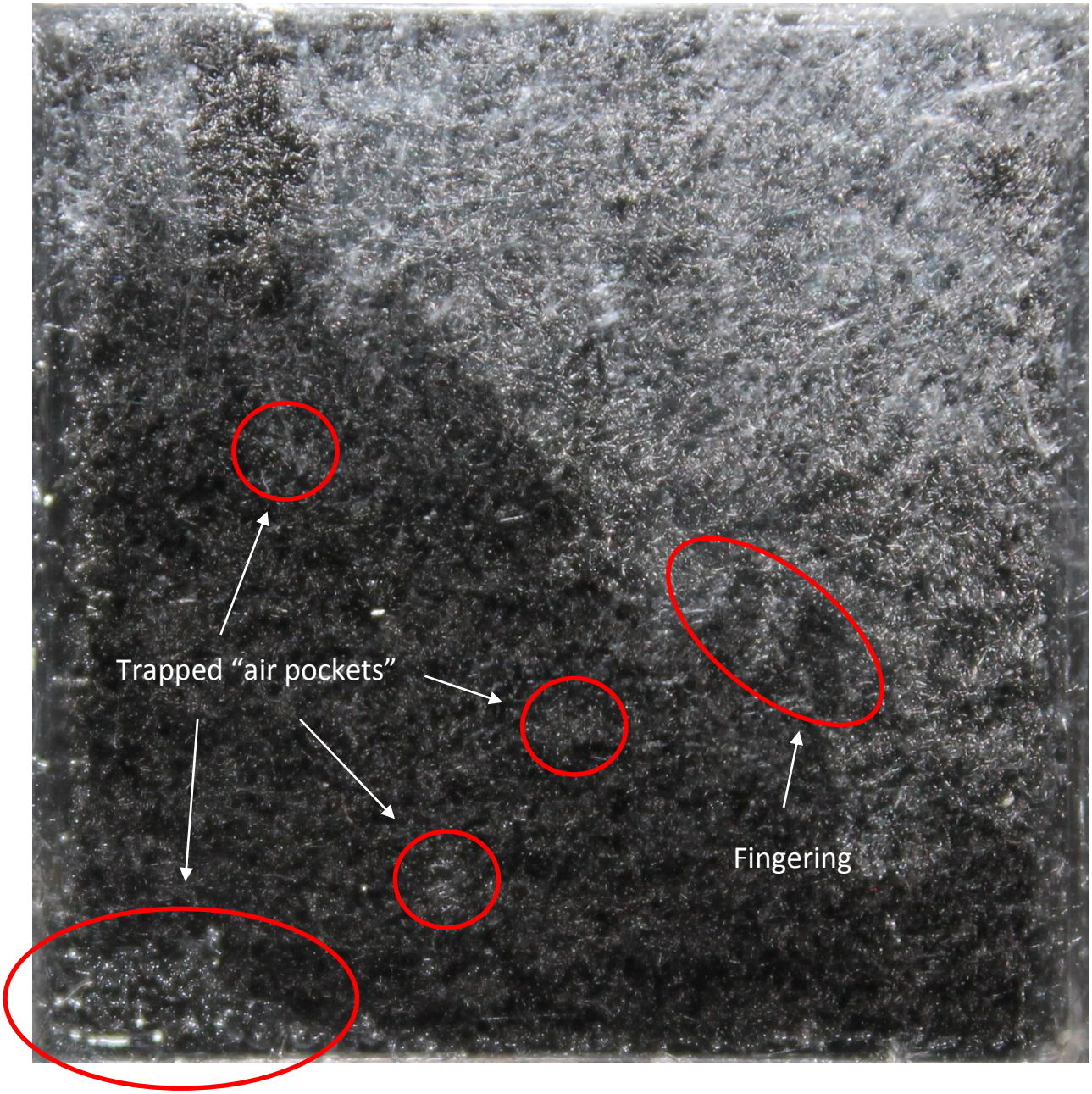

Figure 40 - Detailed picture of oil distribution in porous media experiment

Additionally, the relationship between capillary pressure and buoyancy is studied numerically. A 7.5 cm square piece of graphite felt saturated with oil which has a pocket of air 2.5 cm square pocket of air centered at the bottom initially. Three different cases are considered:

1. Capillary pressure and buoyancy pressure are similar

2. Capillary pressure is 10 times larger than the buoyancy pressure
3. Buoyancy pressure is 10 times larger than the capillary pressure

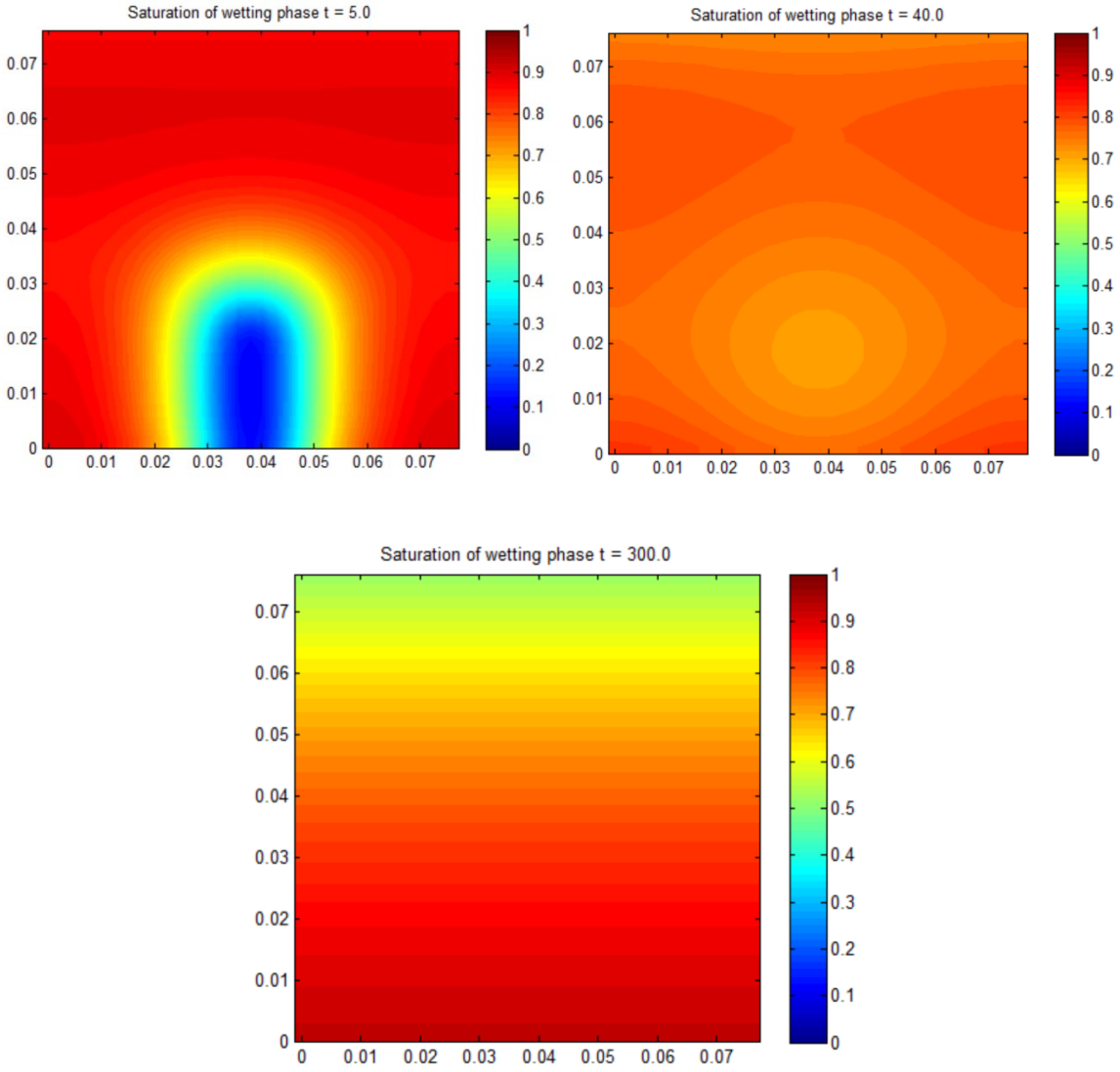

Figure 41 - Porous media model capillary/buoyancy demonstration – Case 1

$$P_{capillary} \approx P_{buoyancy}$$

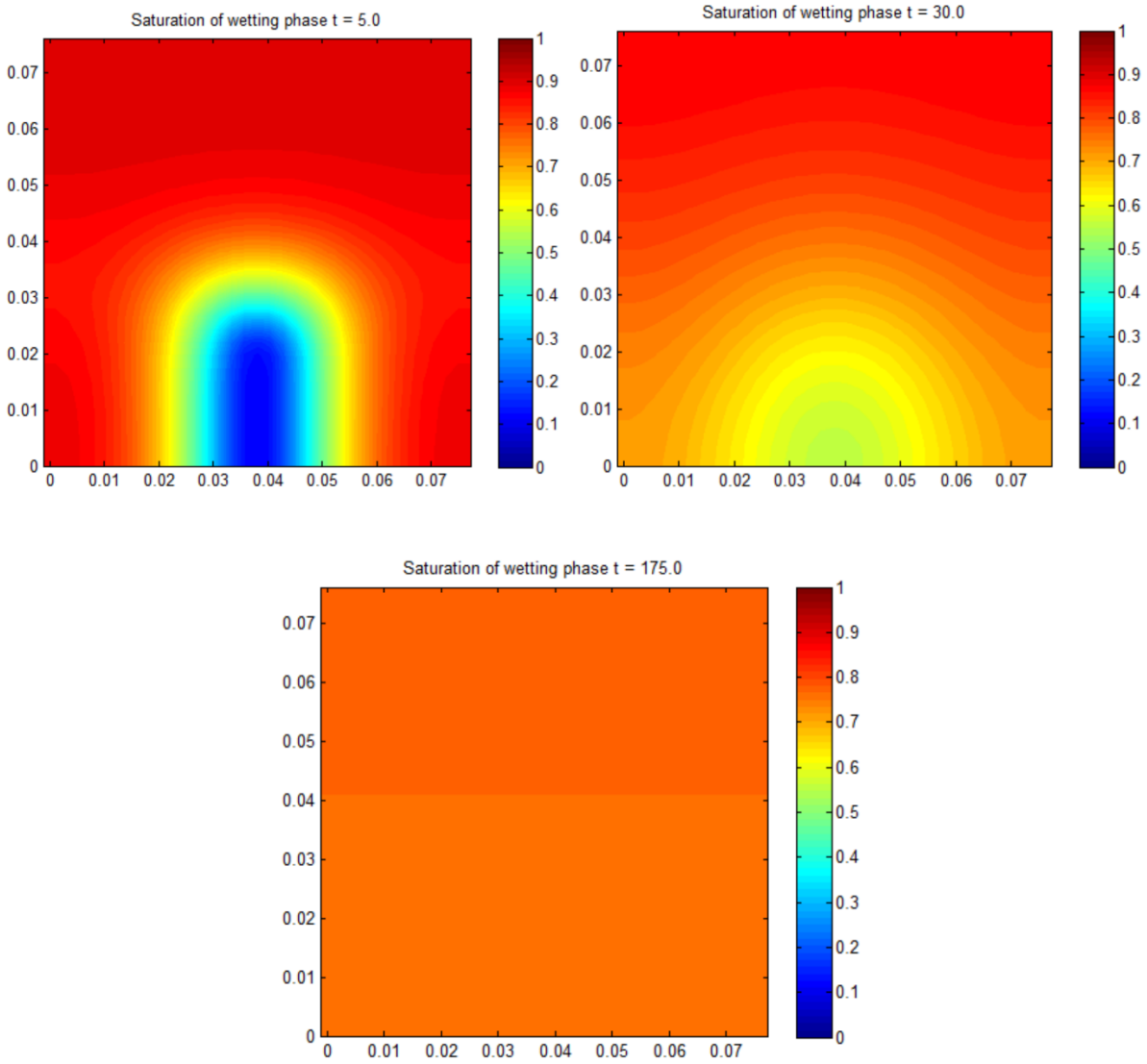

Figure 42 - Porous media model capillary/buoyancy demonstration – Case 2

$$P_{capillary} \approx 10 * P_{buoyancy}$$

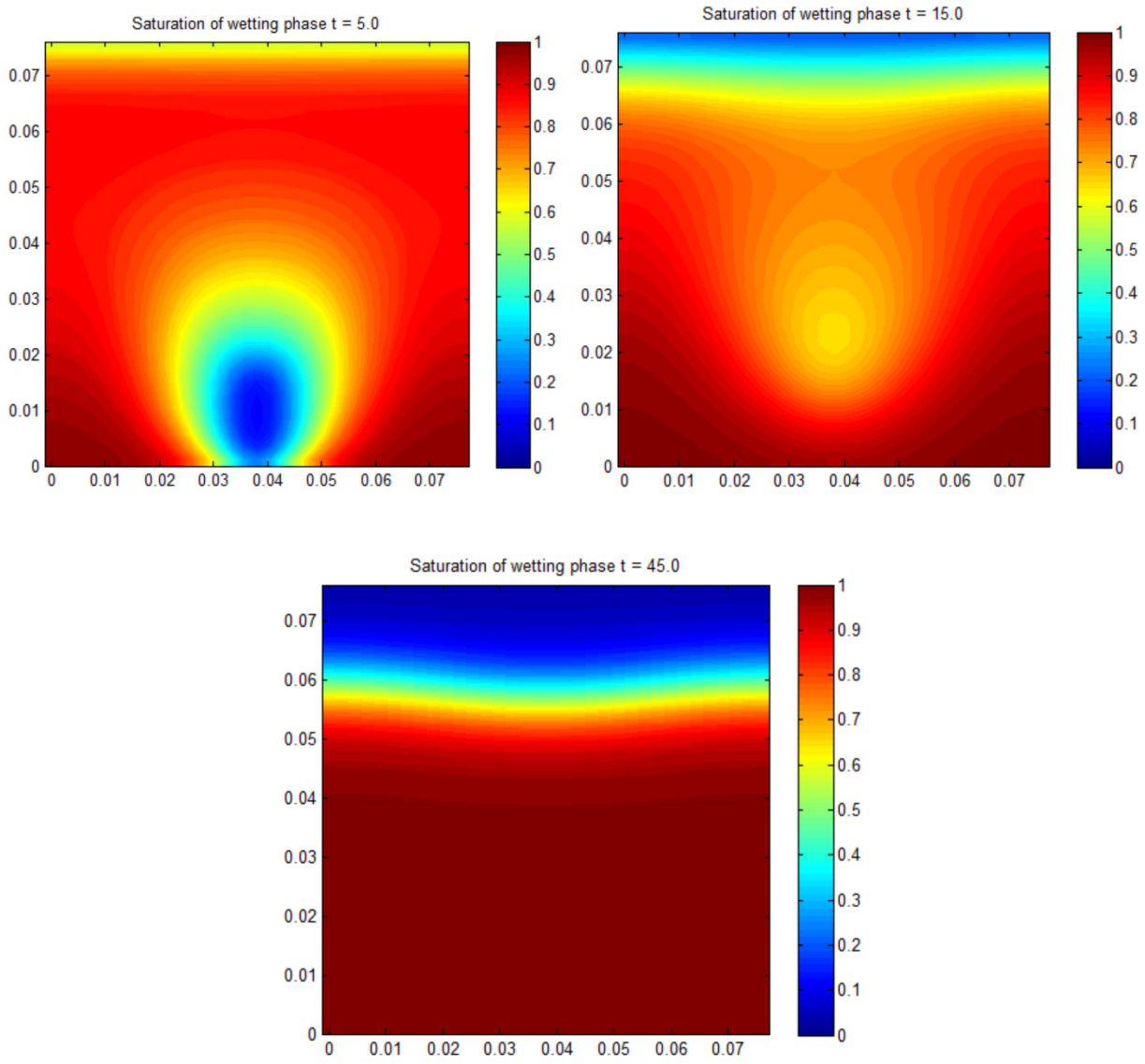

Figure 43 - Porous media model capillary/buoyancy demonstration – Case 3
$\boldsymbol{P_{capillary} \approx 0.1 * P_{buoyancy}}$

When the capillary pressure and buoyancy pressure are equivalent (Case 1, Figure 41), the gas (low saturation region) diffuses quickly as capillary action acts on the high concentration gradient (from $t = 5\,s$ to $t = 40\,s$). Once the concentration gradients are decreased, the buoyancy force takes over as the gas moves upward and displaces the liquid, creating a steady vertical gradient acting against the capillary pressure. When the capillary pressure is an order of

magnitude greater (Case 2, Figure 42) the location of the air “bubble” seems to remain stationary as the air spreads evenly throughout the media via capillary motion. The steady state obtained is similar to that which is predicted to occur in the cathode (nearly homogeneous distribution). Finally, when gravity dominates (Case 3, Figure 43) the air moves upward before it can be diffused by capillary action and a sharp interface is formed between the gas and liquid phases, as is predicted in the anode.

These numerical results seem to be physically plausible and maintain mass conservation throughout the simulations (pressure field is realistic). It is therefore determined that the model properly handles gravitational effects with full validation requiring further experimentation.

7.4 Alternative Cathode designs and parametric studies

As the majority of significant physics occur in the cathode (capillary pressure, temperature, concentration and potential gradients), it is desirable to manufacture the current collector (carbon mesh) in a way that will help reduce these gradients from occurring. One way to accomplish this is by using a mesh with varying electrical conductivity. As mentioned in the literature review, multiple scientists have used a low conductance layer near the electrolyte surface ($r = 7.5\ mm$ in our case) in order to decrease the potential gradients in this region. However, Kawamoto and Wada [8] predict that while the overpotential is significantly decreased by the dual mat electrode, an area of high overpotential still occurs (Figure 8). In this study an attempt to remedy this will be made by using a cathode mesh which has a sloping conductivity gradient, with maximum values on the order of those used in the dual mat cells. Five different conductivity

distributions in the radial direction are considered in this study, including homogeneous, dual mat and newly proposed alternate configurations illustrated in Figure 44. The conductivities in these alternative cathodes increase or decrease exponentially near the electrolyte and cell container. Contour plots of the over potential distributions taken at the same time for the same applied currents are shown for each case in Figure 45 through Figure 47.

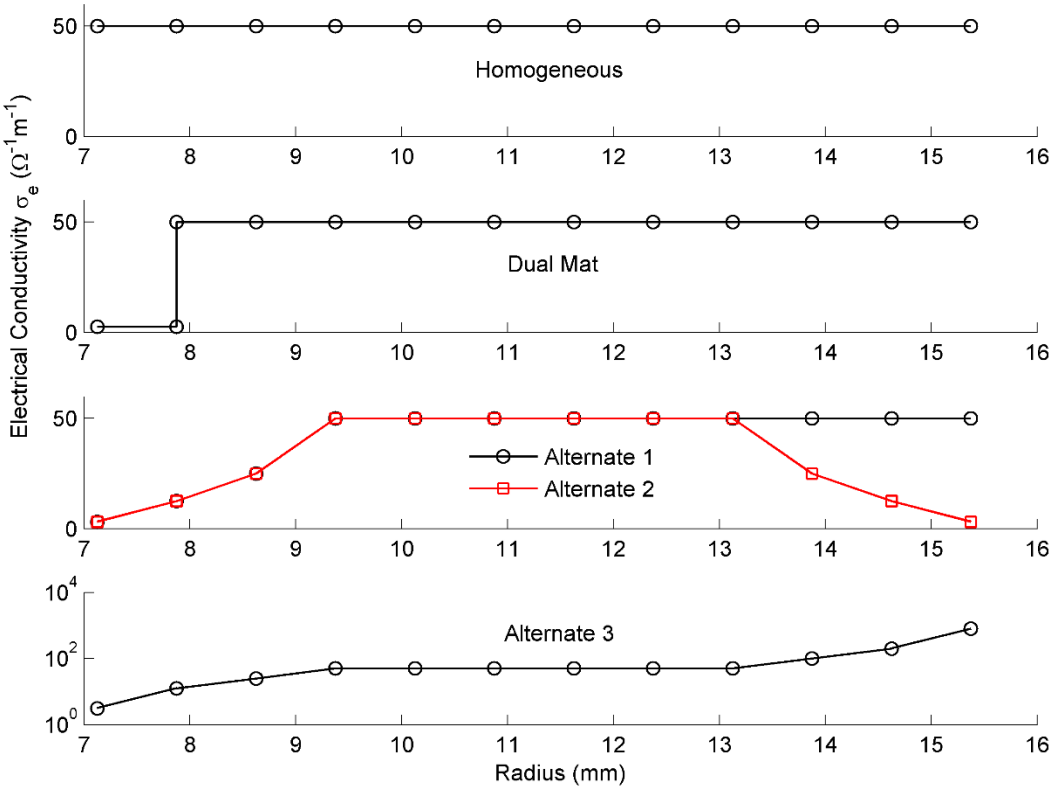

Figure 44 – Alternative cathode mesh conductivity distributions

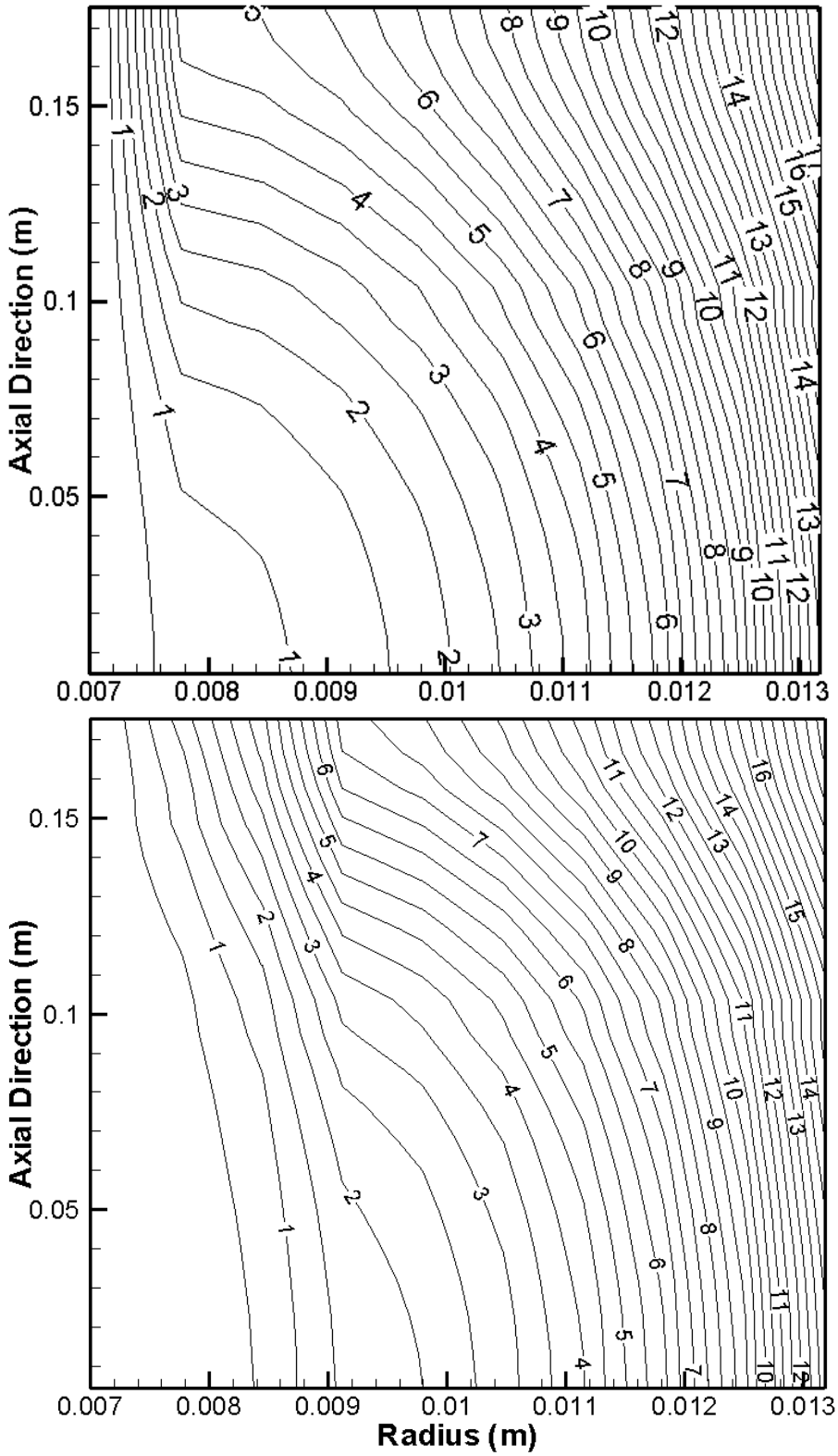

A. Homogeneous

B. Dual mat

Figure 45 – Overpotential (in mV) distributions within the cathode at 750 s into charge with 6 amp current for: A. Homogenous cathode and B. Dual mat

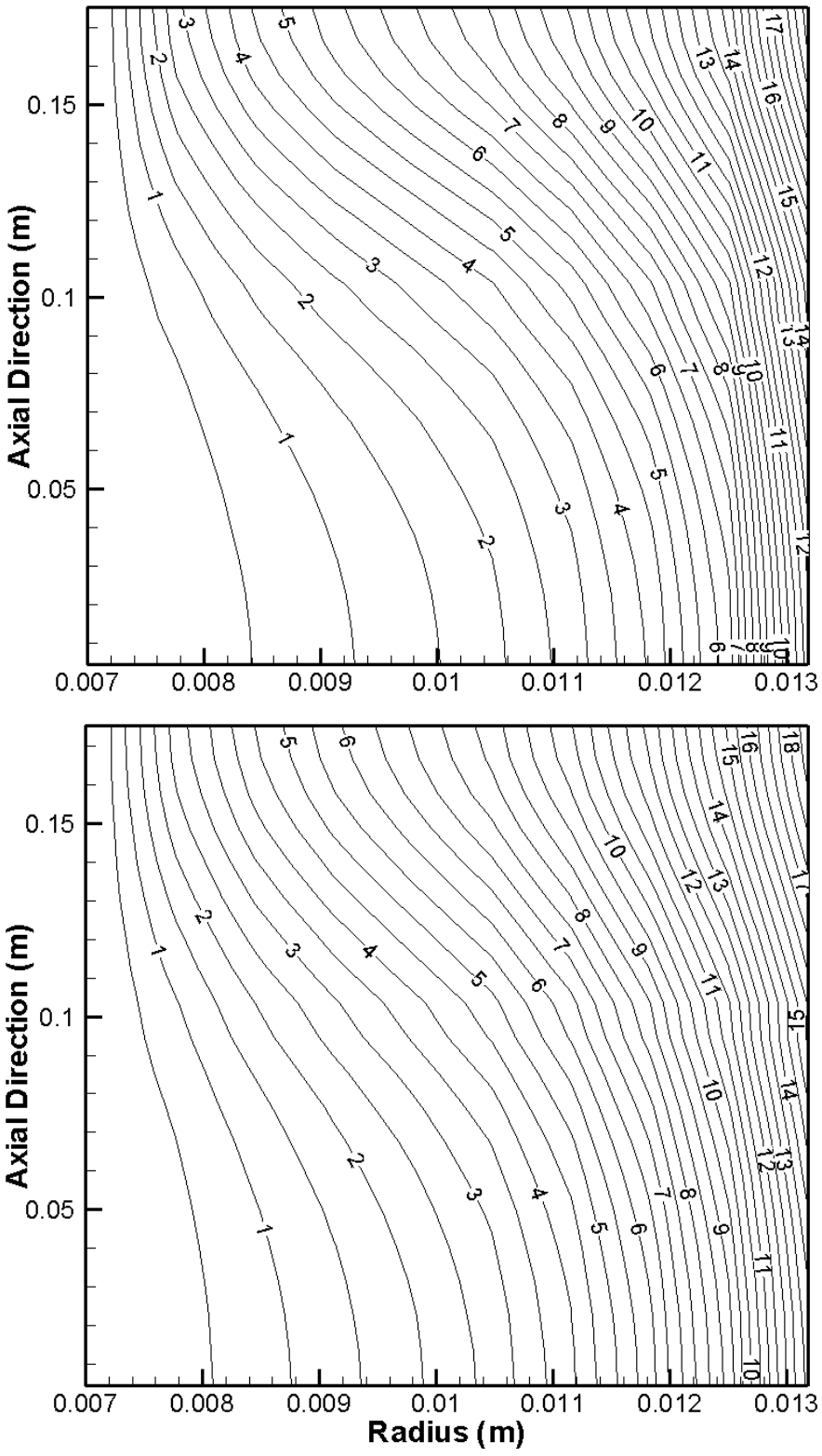

A. Alternative 1

B. Alternative 2

Figure 46 – Overpotential (in mV) distributions within the cathode at 750 s into charge with 6 amp current for: A. Alternative 1 and B. Alternative 2

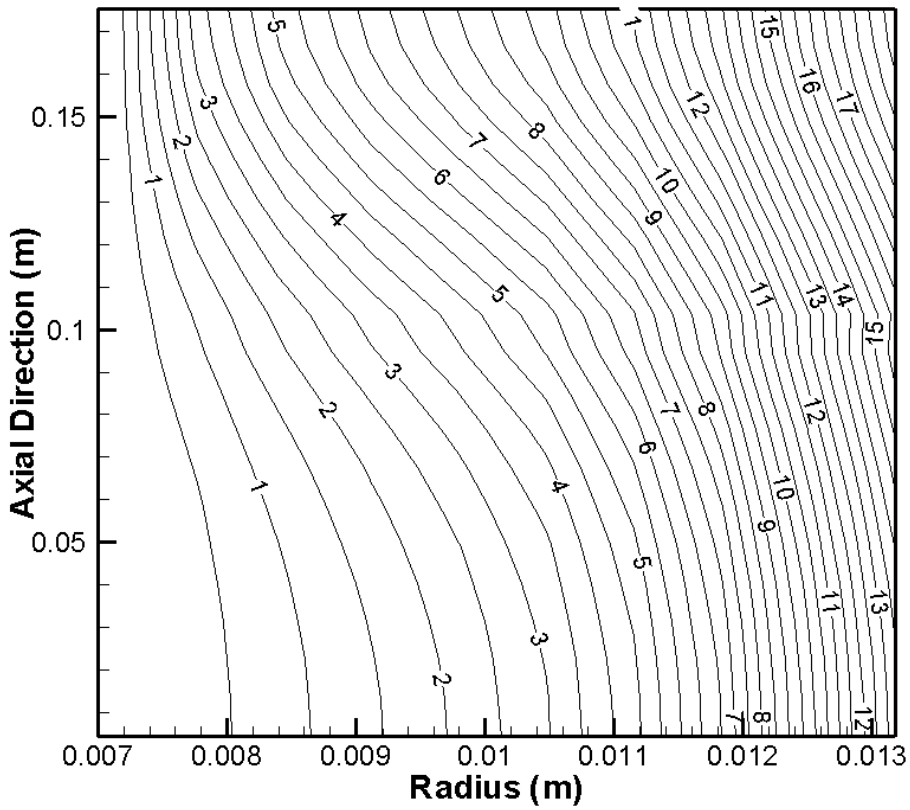

B. Alternative 3

Figure 47 – Overpotential (in mV) distributions within the cathode at 750 s into charge with 6 amp current for Alternative 3

As shown in the homogenous case (Figure 45 A), a potential gradient exists near the electrolyte surface, specifically in the upper portion of the cell. This can be detrimental as sodium will quickly be depleted in a region where low amounts of material are available potentially causing solid precipitation of Na_2S_2 during charge. Unlike previous modes, the present model also predicts a high potential gradient to occur near the wall. The dual mat electrode (Figure 45 B) does decrease the gradient near the electrolyte, but in doing so creates a similar distribution roughly 1 mm away. The first alternative electrode applies an exponential gradient of electrical conductivity at the electrolyte surface in an attempt to avoid this. As shown in Figure 46 A, the resulting potential gradient is

distributed more evenly. However, the overpotential near the wall has not decreased. The second and third alternative cathodes apply an exponentially decreasing and increasing conductivity near the wall respectively in order to reduce this. In Figure 46 B it appears that the gradient is decreased slightly but not a significant amount, as the ionic potential is low in this region compared to the electronic potential. Decreasing the electrical conductivity should theoretically increase the overpotential, but the actual result seems to be a negligible change. Finally, the third alternative electrode design is applied with overpotential distribution shown in Figure 47. As shown, the gradient of the overpotential is more uniform than in the previous cases. However, the magnitude of the overpotentials in this region are relatively constant for all of the applied configurations.

In order to compare the performance of these cell configurations relative to one another, the voltage curves are plotted as a function of depth of discharge (Figure 48) and the effective capacity of each cell is compared (Table 15). The applied current is 9 amps for each case. The initial conditions assume that the cells have completed 5 cycles previously in order to reduce computational time. It is obvious from the table and figure that the dual mat electrode has the worst performance among the cathodes studied. The capacity of this cell is over 40% lower than the original. Alternative cathodes 1 and 2 show significant capacity deficiencies as well. The third design on the other hand gains 5% capacity compared to the original. It is noted that other than the original cathode, only alternative cathode 3 completes an entire cycle before failing, but is predicted to fail shortly into the next cycle. The reason behind these failures are analyzed next.

Table 15 - Capacity comparisons for alternative cathode configurations

	Capacity (Ah)	Capacitance Difference	Percentage Gained/Lost
Orginial	35.77	0.00	0.00%
Dual Mat	20.17	-15.60	**-43.61%**
Alt Cathode 1	33.68	-2.09	**-5.84%**
Alt Cathode 2	26.87	-8.90	**-24.88%**
Alt Cathode 3	37.62	1.85	**+5.17%**

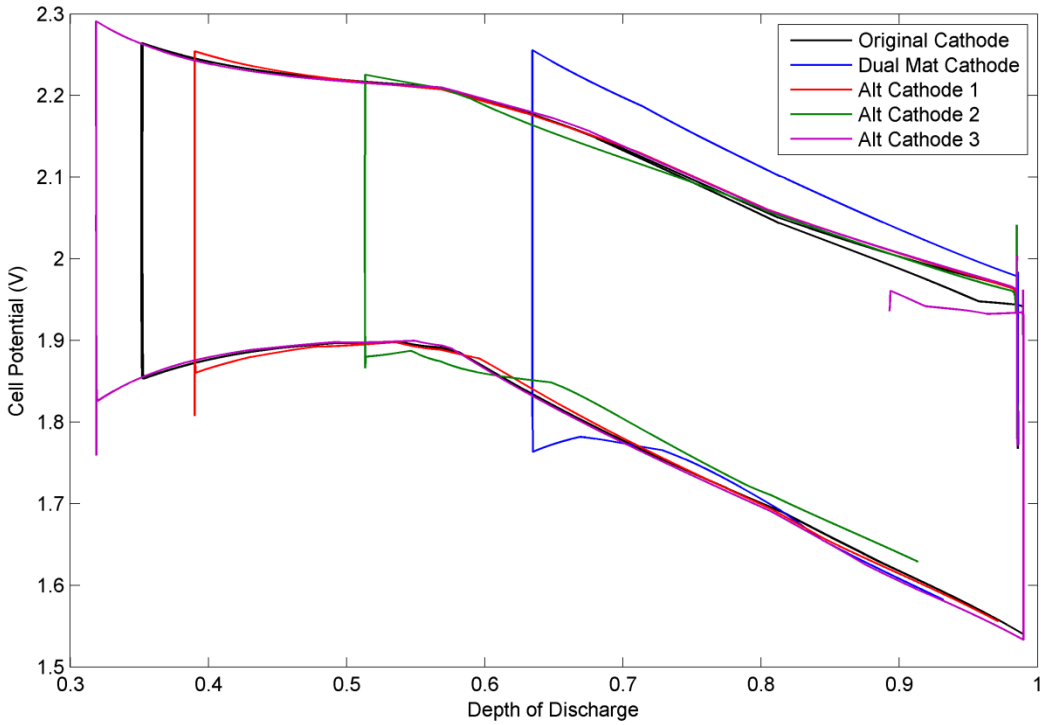

Figure 48 - Voltage curves for alternative cathode configurations

Solid precipitation of Na_2S_2 is a significant problem in sodium sulfur cells. This is why it is an objective to predict when, where and if such precipitation might occur. For the cathodes studied thus far, distributions of X in the radial direction during the course of charge (Figure 49) and discharge (Figure 50) are plotted and compared.

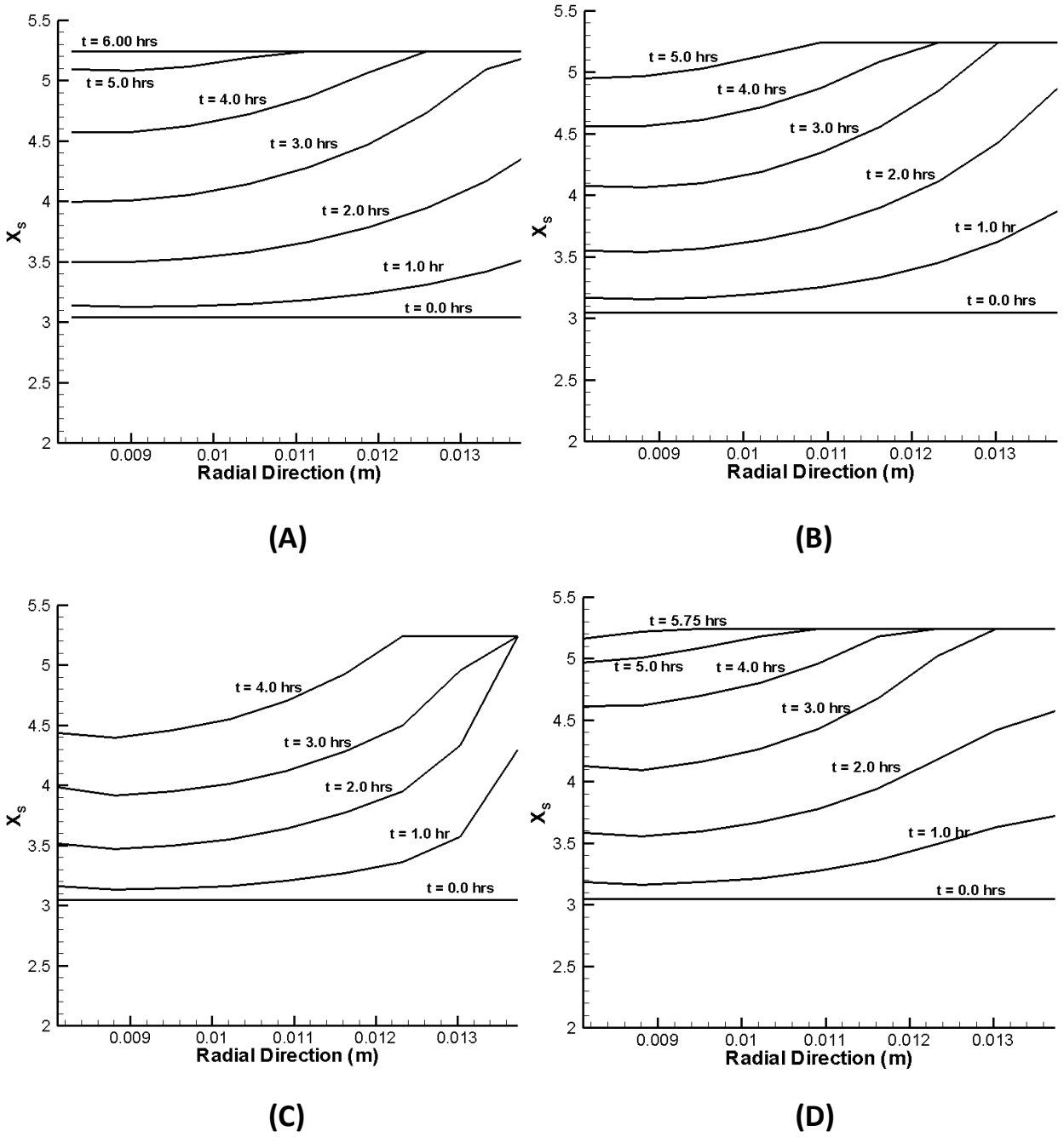

Figure 49 - X_s Distributions during charge in each cathode (A) Original (B) Alternative 1 (C) Alternative 2 (D) Alternative 3

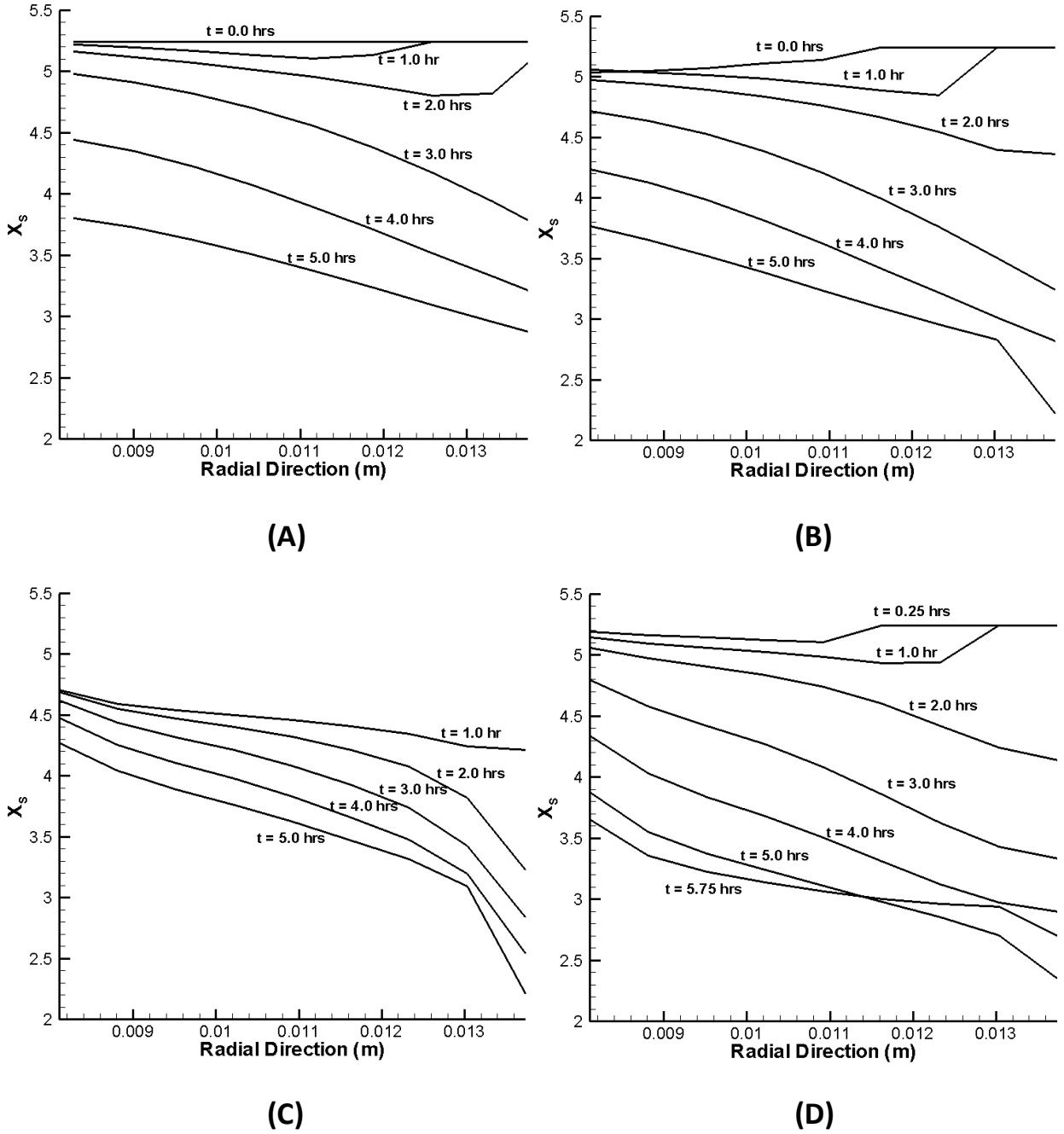

Figure 50 - X_s Distributions during discharge in each cathode (A) Original (B) Alternative 1 (C) Alternative 2 (D) Alternative 3

During charge, all of the cathodes seem to perform similarly. Alternative cathode 2 does seem to maintain high levels of sodium (low X) near the

electrolyte better than the other cathodes, but it is already known that the overall performance of this cathode is worse. Counterintuitive to what previous authors have stated, X increases fastest near the outside wall of the cathode (sodium is being depleted fastest here rather than at electrolyte surface) in each case. This is induced by the electro migration term in the mass transport equation (Equation (29)) which is proportional to the potential gradient. As demonstrated previously, the highest potential gradient occurs near the outside wall, resulting in accelerated mass transport. When the current is reversed and the battery is discharged, X is decreased quickly in the same region. Previous authors have suggested that sodium penetration into the cathode is problematic which is why the cathode is generally designed to be thin. However, these results suggest that the combination of capillary motion, electro migration and diffusion allow for deep penetration of sodium. This could be attributed to the inclusion of capillary motion, which has not been considered before. In fact, so much sodium is drawn towards the wall that X actually falls below 3 for all of the newly designed cathodes, which means that solid precipitation occurs here causing the battery to fail (as predicted by the simulations). It is determined that cathodes with manufactured conductivity gradients are not necessarily beneficial must be designed carefully in order to prevent cell degradation and failure due to solid precipitation, especially when decreasing the conductivity (alternative cathode 2 (Figure 50C) in particular). While increasing the conductivity at the wall in alternative cathode 3 did decrease the potential gradient, it also accelerated the motion of sodium and eventually caused failure.

Chapter 8: Conclusions and Recommendations

In this study, a detailed multiphysics mathematical model was developed to simulate physiochemical processes occurring within NaS batteries. Charge, heat and mass transport equations (specifically capillary motion in porous media) have been developed and are coupled and solved numerically in order to fully resolve the relationships between them. The models have each been validated to some extent using empirical data. It is demonstrated in this study that the porous media model, which was neglected in most previous models, is crucial to understanding the details of NaS battery operation, predicting failure and optimizing their design.

In the process of this study, new cathode designs were developed and simulated. It is shown that proper conductivity distributions in the cathode solid mesh have the potential to improve battery performance and reduce the negative effects of vertical and radial concentration gradients induced by capillary motion and gravity. However, upon further inspection the original cathode with homogeneous conductivity performs best as both increasing and decreasing the conductivity in a region increases the risk of solid precipitation.

In order to fully validate the model, it is recommended that a couple of experiments should be performed. First, the exchange current density between the sodium and solid electrolyte should be explored. It is proposed that an electrochemical experiment using a sodium microelectrode (drop of liquid sodium) could be placed onto an electrolyte with a reservoir of sodium on the opposite side. The use of a sodium microelectrode would allow for the faradaic

current to be measured relatively simply with little interference from the charging current at such small scales.

Second, further experiments which measure the vertical distribution of current density in the NaS cell would allow for further validation of the porous media model when couple with electrochemistry. Also, “freezing” a NaS battery at specific depths of discharge and then cutting the cell open would allow for quantification of the phase distributions to be made, including identification of Na_2S_2 and Na_2S. Combined with the current density measurements, this could confirm the validity of the porous media flow model and the properties used.

Another useful experiment would be an impedance study on the cell which could be used to verify the magnitude of the losses. In particular, the polarization losses that are produced by the predicted “dewetting” phenomena could be measured and compared.

Finally, it is concluded that while porous media effects can be both beneficial and detrimental to NaS battery operation, careful modelling in the design process can be used to predict and alleviate the negative consequences.

References

[1] J. Sudworth and A. Tiley, Sodium Sulphur Battery, Springer Science & Business Media, 1985.

[2] J. P. Deane, B. P. Gallachoir and E. J. McKeogh, "Techno-economic review of existing and new pumped hydro energy storage plant," *Renewable and Sustainable Energy Reviews,* vol. 14, pp. 1293-1302, 2010.

[3] D. Mcconnell, "Opportunities for Pumped Hydro Energy Storage in Australia," Melbourne Energy Institue, Australia, 2014.

[4] B. Dunn, H. Kamath and J.-M. Tarascon, "Electrical Energy Storage for the Grid: A Battery of Choices," *Science,* vol. 334, no. 6058, pp. 928-935, 2011.

[5] H. Lund and G. Salgi, "The role of compressed air energy storage (CAES) in future sustainable," *Energy Conversion and Management,* vol. 50, pp. 1172-1179, 2009.

[6] W. Fan, "A Lumped Computational Model for Sodium Sulfur Battery Analysis - Master's Thesis," 2014.

[7] H. Sezer, M. Aygun, J. Mason, E. Baran and I. Celik, "A Computational Model for Sodium Sulfur Battery Analysis," vol. 69, no. 1, pp. 91-100, 2015.

[8] H. Kawamoto and M. Wada, "Two-Dimensional Distribution of Electrochemical Reaction Rate in Porous Sulfur Electrodes of Sodium-Sulfur Cells," *Journal of The Electrochemical Society,* vol. 134, no. 2, pp. 280-285,

1987.

[9] H. Kawamoto, "Two-Dimensional Distribution of Sodium Polysulfide Composition in Sulfur Electrodes of Sodium-Sulfur Cells," *Journal of The Electrochemical Society,* vol. 136, no. 7, pp. 1851-1860, 1989.

[10] H. Kawamoto, "Dynamic simulation of the charge-discharge characteristics of the sodium-sulphur cell," *Journal of applied electrochemistry,* vol. 21, no. 5, pp. 409-414, 1991.

[11] General Electric Co., "EPRI Report EM-2579," 1982.

[12] General Electric Co., "EPRI Report EM-3453," 1984.

[13] S. R. Pakalapati, "A new reduced order model for solid oxide fuel cells," 2006.

[14] I. Celik and S. R. Pakalapati, "A Modular Approach to SOFC Modeling," 2003.

[15] S. R. Pakalapati, "Numerical Study of Current Distribution Inside the Cathode and Electrolyte on a Solid Oxide Fuel Cell - Masters Thesis," 2003.

[16] J. T. Kummer and N. Weber, "Battery having a molten alkali metal anode and a molten sulfur cathode". U. S. Patent 3,413,150, 26 November 1968.

[17] T. Oshima and M. Kajita, "Development of Sodium-Sulfur Batteries," vol. 1, no. 3, pp. 269-276, 2004.

[18] B. Yang et. al., "On the use of energy storage technologies for regulation services in electric power systems with significant penetration of wind

energy".

[19] W. Zhaoyin, "Study on Energy Storage Technology of Sodium Sulfur Battery and it's Application in Power System," 2006.

[20] B. Tamyurek, D. K. Nichols and O. Demirci, "The NaS battery: a multifunction energy storage system," 2003.

[21] A. R. Sparacino et. al., "Survey of battery energy storage systems and modeling techniques," 2012.

[22] A. Herczog, "Sodium Ion Conducting Glasses for the Sodium-Sulfur Battery," vol. 132, no. 7, pp. 1539-1545, 1985.

[23] R. S. Gordon, "Fabrication and characterization of NASICON electrolytes," vol. 3, pp. 243-248, 1981.

[24] A. E. Sarasua et. al., "Modelling of NAS energy storage system for power system applications," Transmission and Distribution Conference and Exposition: Latin America (T&D-LA), 2010.

[25] N. K. Gupta and R. P. Tischer, "Thermodynamic and Physical Properties of Molten Sodium Polysulfides from Open-Circuit Voltage Measurements," vol. 119, no. 8, pp. 1033-1037, 1972.

[26] M. S. Whittingham, "Electrical Energy Storage and Intercalation Chemistry," vol. 192, no. 4244, pp. 1126-1127, 1976.

[27] K. B. Hueso, M. Armand and T. Rojo, "High temperature sodium batteries:

status, challenges and future trends," vol. 6, no. 3, pp. 734-749, 2013.

[28] H. Zhang and X. Liu, "NASICON-Type Electrolytes for Low Temperature Sodium Battery Applications," 2011.

[29] H. K. a. Y. Kusakabe, "Performance and Thermal Behavior of Sodium-Sulfur Cell under High Current Density Operations," *Journal of the Electrochemical Society,* vol. 136, no. 5, pp. 1355-1361, 1989.

[30] J. M. Kee and H. L. Chang, "Numerical study on the thermal management system of a molten sodium-sulfur battery module," *Journal of Power Sources,* vol. 210, pp. 101-109, 2012.

[31] M. W. Breiter and B. Dunn, "Potential distribution model for rechargeable sulphur electrodes in sodium-sulphur cells," vol. 9, no. 3, pp. 291-299, 1979.

[32] J. G. Gibson, "The distribution of potential and electrochemical reaction rate in molten polysulphide electrodes," *Journal of applied electrochemistry,* vol. 4, pp. 125-134, 1974.

[33] M. Wada, "Numerical simulation of the dual mat sulfur electrode of a sodium sulfur cell," *Journal of The Electrochemical Society,* vol. 134, no. 3, pp. 631-638, 1987.

[34] Y.-K. Kao and P. C. Wayner, "The Transient Response of the Sulfur/Polysulfide Electrode Based on a Varying Concentration Model," *Journal of The Electrochemical Society,* vol. 124, no. 2, pp. 230-236, 1977.

[35] B. Cleaver and A. Davies, "Properties of fused polysulphides—III. EMF measurements on the sodium-sulphur cell, and sulphur activities and constitution in fused sodium polysulphides," *Electrochimica Acta,* vol. 18, no. 10, pp. 733-739, 1973.

[36] R. Knodler, "Thermal properties of sodium-sulphur cells," *Journal of applied electrochemistry,* vol. 14, no. 1, pp. 39-46, 1984.

[37] Z. G. Li and e. al., "Numerical Simulation of the Heat and Mass Transfer in a Sodium Sulfur Cell," vol. 347, pp. 3956-3962, 2012.

[38] J. Newman and K. E. Thomas-Alyea, Electrochemical systems, John Wiley \& Sons, 2012.

[39] E. Rosen and R. Tegman, "Solid, Liquid and Gas-Phase Equilibria in System Sodium Monosulfide Sodium-Polysulfide Sulfur," *Chemica Scripta,* vol. 2, no. 5, p. 221, 1972.

[40] T. Risch and J. Newman, *Transference Number Calculations for Sodium Polysulfides,* vol. 135, 1988, pp. 1715-1718.

[41] A. Szymkiewicz, "Mathematical Models of Flow in Porous Media," in *Modelling Water Flow in Unsaturated Porous Media*, Springer, 2013, pp. 9-47.

[42] R. H. Brooks and A. T. Corey, *Properties of porous media affecting fluid flow,* vol. 92, 1966.

[43] M. Kutílek and D. R. Nielsen, *Soil hydrology: texbook for students of soil science, agriculture, forestry, geoecology, hydrology, geomorphology and other related disciplines,* Catena Verlag, 1994.

[44] L. Ning and W. J. Likos, *Unsaturated Soil Mechanics,* Wiley, 2004.

[45] D. Or and J. M. Wraith, *Soil water content and water potential relationships,* vol. 1, 2002.

[46] G. F. Pinder and W. G. Gray, *Essentials of Multiphase Flow in Porous Media,* Wiley, 2008.

[47] H. Hoteit and A. Firoozabadi, "Numerical modeling of two-phase flow in heterogeneous permeable media with different capillarity pressures," *Advances in Water Resources,* vol. 31, no. 1, pp. 56-73, 2008.

[48] L. Lassabatere, R. Angulo-Jaramillo, J. M. Soria Ugalde, R. Cuenca, I. Braud and R. Haverkamp, *Beerkan estimation of soil transfer parameters through infiltration experiments—BEST,* vol. 70, 2006.

[49] M. Leverett, "Capillary behavior in porous solids," *Trans AIME Petroleum Engineering Division,* vol. 142, pp. 152-169, 1941.

[50] R. Brooks and A. Corey, "Hydraulic properties of porous media," *Hydrol Pap,* vol. 3, 1964.

[51] S. E. Buckley and M. Leverett, *Mechanism of fluid displacement in sands,* vol. 146, 1942.

[52] C. J. Van Duijn and M. J. De Neef, *Similarity solution for capillary redistribution of two phases in a porous medium with a single discontinuity,* vol. 21, 1998.

[53] X. Gao and N. Wu, *Personal Corresponance,* Morgantown, WV: West Virginia University, 2015.

[54] EMD Millipore Corp., *Rapid Lateral Flow Test Strips,* Billerica, MA, 2013.

[55] S. A. Zhdanov, V. M. Starov, V. D. Sobolev and M. G. Velarde, "Spreading of aqueous SDS solutions over nitrocellulose membranes," *Journal of Colloid and Interface Science,* vol. 264, pp. 481-489, 2003.

[56] J. K. Min and C.-H. Lee, "Numerical study on the thermal management system of a molten sodium-sulfur battery module," *Journal of Power Sources,* vol. 210, pp. 101-109, 2012.

[57] G. J. Janz, C. B. Allen, N. P. Bansal, R. M. Murphy and R. P. T. Tomkins, *Physical Properties Data Compilations Relevant to Energy Storage,* Troy, New York: Cogswell Laboratory, 1979.

[58] S. D. Thompson and J. Newman, "Differential Diffusion Coefficients of Sodium Polysulfide Melts," *Journal of the Electrochemical Society,* vol. 136, no. 11, pp. 3362-3369, November 1989.

[59] A. Bejan, Convection Heat Transfer, John Wiley & Sons, 2013.

[60] A. Bito, "Overview of the Sodium-Sulfur Battery for the IEEF Stationary

Battery Committee," in *IEEE PES Annual meeting*, 2005.

[61] L. W. Chung, M. Siam, A. B. Ismail and Z. F. Hussien, "Modeling and Simulation of Na-S Battery for Battery Energy Storage System and Custom Power Devices," in *National Power & Energy Conference (PeCon)*, Kuala Lumpur, 2004.

[62] A. R. Sparacino, G. F. Reed, R. J. Kerestes, B. M. Grainger and Z. T. Smith, "Survey of Battery Energy Storage Systems and Modeling Techniques," in *IEEE*, 2012.